Open Journal of Geology, 2026, 16(9), 606-666
https://www.scirp.org/journal/ojg
ISSN Online: 2161-7589
ISSN Print: 2161-7570

Lithostructural Mapping and Petrology of Banded Iron Formations (BIF) Associated with Metamorphic Rocks of the Bogoin Complex, West-Central Central African Republic, Northern Margin of the Congo Craton: Implications for Its Origin and Tectonic Environment

Rodrigue Martial Topien[1]*, Jules Tcheumenak Kouémo[2], Cyrille Prosper Ndepete[3], José Kpéou[3], Gaetan Moloto-A-Kenguemba[3], Maurice Kwékam[4]

[1]Department of Mining Engineering and Geology, Higher Institute of Technology, Bangui, Central African Republic
[2]Department of Earth Sciences, Faculty of Science, University of Douala, Douala, Cameroon
[3]Department of Geology, University of Bangui, Bangui, Central African Republic
[4]Department of Earth Sciences, Faculty of Sciences, University of Dschang, Dschang, Cameroon
Email: *topienrodriguemartial@gmail.com, Rodrigue-martial.topien@univ-bangui.org

How to cite this paper: Topien, R.M., Tcheumenak Kouémo, J., Ndepete, C.P., Kpéou, J., Moloto-A-Kenguemba, G. and Kwékam, M. (2026) Lithostructural Mapping and Petrology of Banded Iron Formations (BIF) Associated with Metamorphic Rocks of the Bogoin Complex, West-Central Central African Republic, Northern Margin of the Congo Craton: Implications for Its Origin and Tectonic Environment. *Open Journal of Geology*, **16**, 606-666.
https://doi.org/10.4236/ojg.2026.169031

Received: June 1, 2026
Accepted: September 21, 2026
Published: September 24, 2026

Abstract

Detailed remote sensing, petrographic, and geochemical data were processed in the Bogoin to produce a lithostructural map, determine the petrogenesis history and the tectonic and geodynamic reconstruction. Landsat images and field and petrographic observations highlight two main lithologies: the banded iron formations (BIFs) intercalated with metamorphosed host rocks consisting of orthogneisses and mafic rocks. Geochemical data indicate that the mafic host rocks (amphibolites) associated with the Bogoin BIFs originated from metamorphosed tholeiitic to calc-alkaline MORB-like protoliths emplaced in a submarine volcanic-arc environment. The BIFs themselves, in contrast, are interpreted as chemical (chemogenic) sediments precipitated from a mixture of seawater and low-temperature hydrothermal solutions, subsequently affected by contamination and metasomatism during Paleoproterozoic (Eburnean-Trans-Amazonian) subduction and collision. The geotectonic evolution of the host rocks associated with the Bogoin iron deposit is related to this Paleoproterozoic subduction and collision along an extending continental margin, during which the dominant iron-bearing rock assemblages record a sequential geodynamic change from extension to compression. Structural data evidenced intense polyphase deformations defined by D1, D2 and D3 accompanied by a series of brittle-ductile deformation, similar to other Congo craton greenstone belts. The similarity between data from the Bogoin area in the Yangana complex and data from the Nyong complex in Cameroon suggests that they belong to the same blocks. The results of several studies conducted in recent years on the Nyong complex and the São Francisco craton suggest that they originated from the same quasi-rigid, dismembered and reworked blocks that may also be similar to the Yangana complex in the southern part of the Central African Republic.

Keywords

Remote Sensing, Banded Iron Formations, Bogoin Complex, Northern Margin of the Congo Craton, Central African Republic

1. Introduction

The examination of mafic-ultramafic rocks holds significant importance across various aspects within Precambrian greenstone belts [1] [2]. These rocks reflect distinct tectonic environments and offer valuable insights into plate tectonic processes and the evolution of the lithospheric mantle (*e.g.*, [3]-[6]). The composition of Earth's mantle has undergone considerable alteration due to the formation of the continental crust, which has created a stable, buoyant reservoir capable of seizing mantle material and generating rich, diverse metallogenic belts (*e.g.*, [7] [8]). The evolution of the Earth's crust is crucial in determining the location and development of various sources of valuable mineralization, particularly for iron, nickel, and gold. These minerals are often found in deposits of thick iron formations (IFs), as well as in mafic and ultramafic rocks and within fertile crust regions. Over time, the erosion of the old crust occurs due to two primary processes: the gradual accumulation of new crust or the tectonic recycling of the existing old crust (*e.g.*, [9]-[11]). Mafic and ultramafic rocks are particularly significant since they host numerous metal deposits, including gold, nickel, chromium, cobalt, copper, iron, and platinum group elements (PGE), as well as volcanogenic massive sulphide (VMS) and diamond deposits around the globe (*e.g.*, [5] [11]-[16]).

Thallapalli *et al.* [2] reported that mafic and ultramafic rocks are distinguished by their holomelonocratic nature. Common examples of these rock types include peridotites, pyroxenites, and hornblendites within the layered complex, as well as komatiites and basalts in greenstone sequences [8] [11] [12] [17]. In all litho-tectonic associations, the composition of the mantle from which they originate is documented. These rocks are linked to extensional tectonic processes that have occurred in the crust since the Palaeo-Archean [18].

The Bogoin complex represents the northern margin of the Congo craton in the Central African Republic (CAR), where several iron deposits are hosted by metamorphic iron formations (IFs) (*e.g.*, [19] [20]). Except for work by Biandja [19] and Poidevin [20], no detailed lithology of the Bogoin Complex BIF sequences has been documented in the literature.

Although very little work has been done on the Bogoin greenstone, studies of the iron formations associated with mafic and felsic rocks have been carried out in order to understand the genesis and geological context of iron mineralisation in the area. Previous research has largely neglected the structural evolution recorded by the banded iron formations (BIFs) of the Bogoin complex. In contrast to the extensive structural studies conducted on well-characterized BIFs in Brazil (such as those by [21]-[23]), Australia (for example, [24] [25]) and Cameroon [26] [27], the post-depositional deformation of BIFs and the corresponding tectonic structures within the Bogoin Complex remain inadequately documented.

It is generally considered that the Bogoin complex was located in an environment of subduction of the oceanic lithosphere during the Paleoproterozoic [19] [20] [28]. This paper presents a detailed litho-structural map, petrographic and geochemical data on BIFs associated with mafic and felsic rocks. The main objectives are 1) to present new geological data on the mafic host rocks in view of the geotectonic and geodynamic setting of the Bogoin complex and 2) to discuss the origins of these rocks BIFs.

2. Geologic Settings

The Pan-African North Equatorial Fold Belt (PANEFB), or Central African Fold Belt (CAFB) [29], is a major Neoproterozoic orogeny linked to the Trans-Saharan Belt of western Africa and the Brasiliano Orogen of NE Brazil. The CAFB is located between the Congo Craton and the Sahara Metacraton. It was remobilised during the Pan-African orogeny between 700 and 500 Ma [30]. In the Central African Republic (CAR), this belt is commonly subdivided into two main domains ([28] [31]-[42]). 1) The northern domain, or Yadé, or Adamawa-Yadé, in which our study area is located (**Figure 1**). It continues in Cameroon and Chad, where it is known as the Adamawa domain, hence the name "Adamawa-Yadé domain" ([37] [38] [40] [41] [43]-[47]) or "Yadé-Adamawa", often used; 2) the south domain of the CAR, or the Yangana or Yaoundé-Yangana, where our study area is located, extends from the Congo Craton craton to the Yadé-Adamaoua domain and continues into Cameroon, where it is known as the South-Cameroon domain [32] [48], and extends from the Congo craton to the Yadé-Adamaoua domain and extends into Cameroon, where it is known as the South Cameroon domain [32] [48].

This domain is subdivided into two units (south and intermediate units): 1) The Southern unit represent a northern part of Congo Craton and consists of metasediments of Archean and Paleoproterozoic age [48]; metabasites of Archean age (2900 Ma, [34]); Komatiites, itabirites, greywacke, rhyodacitic tuffs, amphibolites, orthogneisses and granitoids [33]. 2) Intermediate unit consists of gneisses, metasedimentary, metabasites rocks and migmatites of Archean and Paleoproterozoic age. These rocks are separated from the Neoproterozoic gneisses by a ductile shear zone [35]. This domain comprises several lithological units, represented by mafic, ultramafic, and felsic rocks [28] [37] [48] [51] [52]. It corresponds to a basement of Archean to Paleoproterozoic age dismembered during the Pan-African orogeny [32] [35] [45] [53] [54].

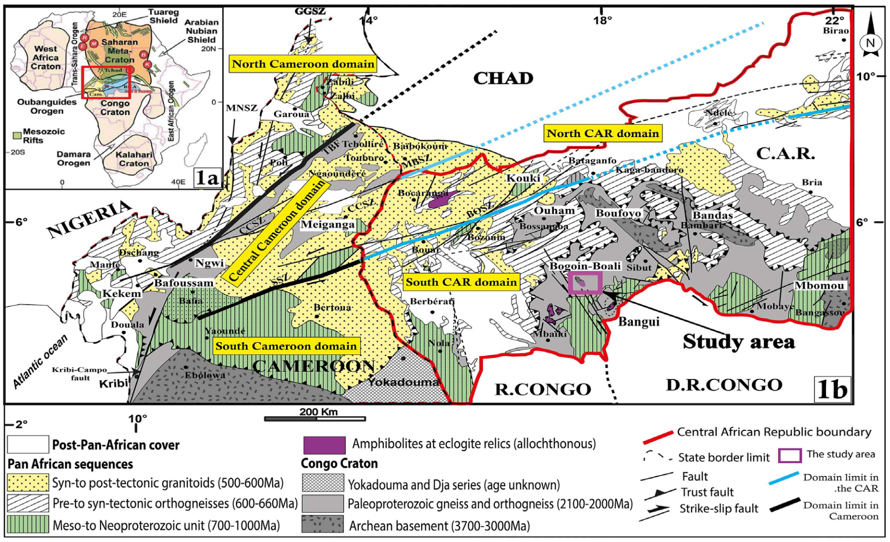

Figure 1. (a) African Precambrian orogenic belts, metacratons, and cratons ([49], modified from [50]); (b) Geological map of the CAFB in Central Africa [41], showing the main lithotectonic units and domains of the Central-African Orogenic Belt (BOSZ, Bozoum-Ndélé shear zone; CAR, Central African Republic; CCSZ, Central Cameroon shear zone; D. R. Congo, Democratic Republic of Congo; MBSZ, M'Béré shear zone; MNSZ, Mayo Nolti shear zone; R. Congo, Congo Republic; SSZ, Sanaga shear zone; SZ, shear zone; TBF, Tcholliré Banyo Fault).

The greenstone belts of Bandas (central and central-eastern Central African Republic) and Bogoin (central-western Central African Republic) are 250 and 150 km long, respectively.

The dominant metavolcanic rocks in the belts are komatiitic and tholeiitic basalts [28] [33] [48]. Komatiites and tholeiites depleted in light rare-earth elements likely originate from a common source in the upper mantle. The ultramafic and mafic terms can be related to the same magmatic lineage ranging from true komatiites (MgO > 27%) to tholeiites (10% > MgO > 3%) via komatiitic basalts (22% > MgO > 12%). The Bogoin greenstone rocks are located approximately 100 km northwest of Bangui, in central-western Central African Republic (**Figure 1**). The supracrustal units are preserved in complex, narrow, sinuous structures that are about 80 km long [55]. The north-eastern part, the Bogoin greenstone sensu stricto, was first mapped by Mestraud and Bessoles (1982) and has been the subject of recent geological studies [19] [20] [28] [48].

These supracrustal units are unconformably overlain by low-grade basal

Yangana-type schists intruded by a 2.08 Ga granite (U-Pb zircon age; [31]) and by upper quartzites, also of Palaeoproterozoic age. Several types of granitoids cut the greenstone units: 1) large trondhjemite-tonalite plutons older than the Yangana schists; 2) granodiorites and porphyritic granites older than the schists but intrusive in the tonalites; 3) the fluorite-rich alkaline granite of Mbolene. The Bogoin greenstone is younger than the Archean domain of central CAR and northeastern Congo [34] [48] and older than the 2.15 Ga post-tectonic Mbolene granite.

Geochronological data make it possible to characterise three (3) major chronological assemblages in this domain [48]: the first, of Lower Archean age (3.7 - 3.4 Ga), corresponds to the Mbomou complex (south-eastern CAR); the second groups together the green rocks of central CAR, namely at Boufoyo and Bandas (3.0 Ga; Boufoyo is assumed to be younger than Bandas); the last set is basal Proterozoic (2.4 - 2.2 Ga) and corresponds to Bogoin (or Bogoin-Boali) greenstones (**Figure 2**). To sum up, the spatial arrangement of the mafic and ultramafic assemblages in this domain is from oldest to youngest, moving from east to west (**Figure 1**).

The amphibolites of the upper Bogoin assemblages form part of the supercrustal series of the Bogoin greenstone belt (west-central Central African Republic). They are underlain by Al-depleted komatiites, back-arc tholeiites and arc-related greywackes. Pb-Pb and Sm-Nd isotopic data give an imprecise isochron age of around 2.3 Ga, which is thought to represent the depositional time of the greenstones [20] [34]. The genesis of the amphibolites in the upper Bogoin assemblages is explained by mixing depleted and enriched components. Sm/Nd isotopic data and major element content suggest the involvement of a trondhjemite-type melt rather than sediments as the enriched component. The depleted component may be produced by residues of a peridotitic residue after extraction of tholeiites similar to the tholeiites of the lower unit [20]. The presence of back-arc tholeiites, arc-related greywackes, and boninite-type amphibolites from the upper BogoIIin units strongly supports a compressional-edge plate boundary for the Bogoin greenstone belt [20]. According to Giorgi [56], the Bogoin-Boali greenstone belt (**Figure 1**) corresponds to the southern part of a cratonic mole recognised in the Central African mobile zone in the west of the country. It is characterised by the succession of several differentiated volcanic episodes [20] [56]. The tholeiitic terms of the various mafic formations of the Bogoin belt, together with the modern tholeiites, indicate a duality of origin with metabasalts of intraplate affinity and a majority of abyssal affinity.

The Bogoin trench is a zone of weakness (initial graben) involved in successive orogenies north of the Congo craton in the Central African mobile zone [33]. The Bogoin greenstone presents a relatively complex succession [20]: 1) the base unit I can be considered as a fragment of oceanic crust; 2) the associated sediments of unit II correspond to the destruction products of an active continental margin volcanic arc; 3) unit III, characterised by the association of boninites and komatiites, may correspond to fore-arc basin products; 4) the ferruginous quartzite that overlies it (unit IV) may have been deposited in a shallow marine basin.

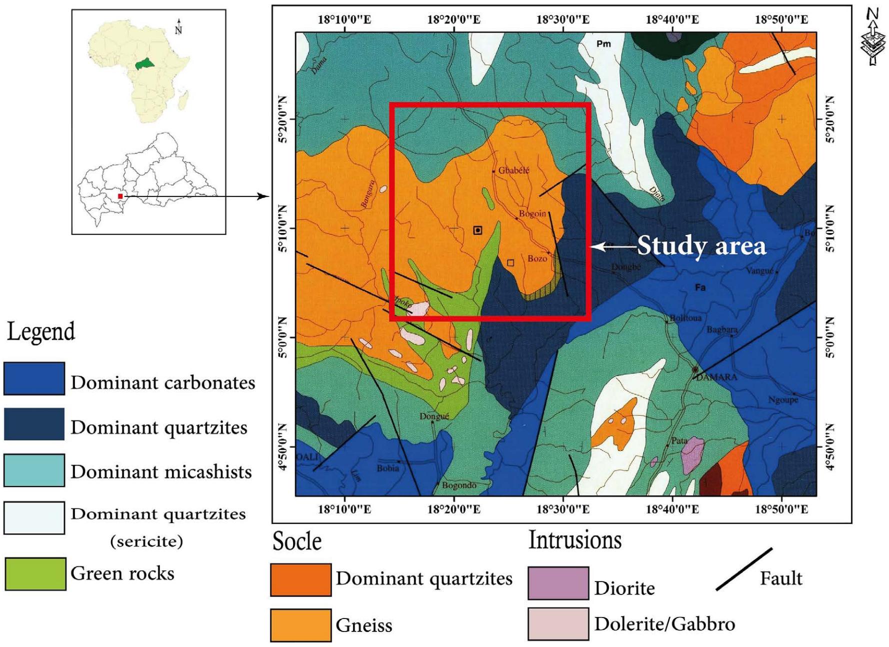

Figure 2. Bogoin geological map after Rolin [57] (1:1.500000) cut to the scale of the study area (central western CAR).

The iron deposits were discovered in the surrounding greenstone belts (**Figure 2**). The iron deposits of the Bogoin complex consist of metasedimentary and metavolcanic rocks as well as intrusive rocks [19] [20]. Although the Bogoin banded iron formation (BIF) contains significant iron deposits, little information has been published on its origin and geodynamic context.

3. Material and Methods

3.1. Data

To conduct our research, we began with a literature review (bibliographic study) before shifting our focus to fieldwork, where we applied various prospecting techniques. The location of outcrops was determined using the global positioning system (GPS) and a base topographic map. The strikes and dips of rock foliations were meticulously measured using clinometers and recorded. Photographs of outcrops and their significant geological features were taken and archived. Representative rock samples were collected from outcrops and road cuts, employing geological hammers. The strikes and dips of outcrops, as well as structural features measured, were recorded.

3.2. Methods

In this paper, we focused on metamorphosed rocks associated with the Bogoin BIFs. 10 samples were selected for petrographic and 9 for geochemical investigations, all of which were fresh rock samples. We observed the thin sections using transmitted and reflected light microscopy at the Laboratory of the Geology Department, University of Ibadan, Oyo State, Nigeria. Other samples were analyzed for major and trace element concentrations at Nancy Laboratory, Rock and Mineral Analysis Service SARM, Nancy, France. Sample locations, lithology, and selection criteria: Outcrop and sample locations were recorded in the field with a handheld GPS receiver (WGS 84 datum) and are listed in **Table 1** together with their dominant lithology. The lithologies recognized in the field include migmatites, granite gneiss (orthogneiss), amphibolites, chlorite schists, itabirites (BIF), basic volcanites (dolerites), and quartzites, together with calcareous units and the location of artisanal gold-mining sites recorded for reference. These outcrops occur along the contacts between the itabirites and their orthogneissic and amphibolitic host rocks and the surrounding basement gneisses and migmatites, which allowed the field relationships between the mapped units to be established. Samples retained for petrographic and geochemical analysis (Sections 4.1.1 and 4.1.3) were selected from these outcrops based on 1) freshness, *i.e.*, the absence of visible weathering, oxidation staining, or vein material; and 2) representativeness of the main mapped lithological units and of their contacts.

Table 1. Coordinates (WGS 84) and dominant lithology of outcrops recorded in the Bogoin study area.

Longitude (X˚)_WGS84	Latitude (Y˚)_WGS84	Lithology
18.429	5.325	Migmatites
18.395	5.282	Migmatites
18.358	5.278	Migmatites
18.333	5.236	Migmatites
18.306	5.22	Migmatites
18.269	5.26	Migmatites
18.404	5.245	Amphibolites
18.391	5.196	Amphibolites
18.37	5.186	Chlorite schistes
18.334	5.182	Chlorite schistes
18.328	5.136	Chlorite schistes
18.273	5.156	Chlorite schistes
18.329	5.137	Chlorite schistes
18.27	5.089	Chlorite schistes
18.314	5.036	Chlorite schistes
18.339	5.075	Itabirites
18.379	5.109	Itabirites
18.378	5.129	Itabirites
18.385	5.138	Itabirites

Continued

18.366	5.064	Basic volcanites
18.375	5.08	Basic volcanites
18.392	5.106	Quartzites
18.401	5.087	Quartzites
18.422	5.118	Granite gneiss
18.436	5.159	Granite gneiss
18.417	5.201	Granite gneiss
18.485	5.029	Calcareous
18.499	5.044	Calcareous
18.517	5.052	Calcareous
18.52	5.074	Calcareous
18.379	5.168	Gold-mining sites
18.345	5.16	Gold-mining sites
18.396	5.164	Dolerites
18.39	5.154	Dolerites

In this study, we utilized three types of materials: a geological map of the Central African Republic at a scale of 1:1.500000 [57] (**Figure 2**), a geomorphological map of the western region of the Central African Republic at a scale of 1:1.000000 [58], and satellite imagery including Landsat 8 OLI and SRTM DEM data.

The Landsat 8/LDCM (Landsat Data Continuity Mission) satellite image of scene 180-51 was acquired from https://earthexplorer.usgs.gov/ with 0% clouds on January 10, 2023 (**Figure 2**). The characteristics of the Landsat 8 image are detailed in **Table 2** (**Figure 3**). The image corresponds to Zone 34 North of the Universal Transverse Mercator (UTM) projection system and follows the WGS 84 geodetic reference system. Various researchers have employed SRTM data [41] [59] and Landsat 7 ETM+ [60] for automatic lineament extraction and geological mapping due to their advantageous characteristics. In this study, we used these datasets to extract lineaments using PCI Geomatica 2017 software. Additionally, ArcGIS 10.5 was employed for statistical analysis of the lineaments and to convert the data into a suitable format (Autocad) for use in Works 17 software, specifically designed for generating directional rosette diagrams.

Three field campaigns were conducted in the Bogoin area from March 8-12 2023, April 13-16 2023, and May 10-15 2025.

3.2.1. Preprocessing of the Data

The schematic diagram (**Figure 4**) shows the steps of the pre-processing and image processing of Landsat 8 OLI and DEM data. The pre-processing steps in this study involved radiometric calibration and atmospheric correction using the FLAASH (Fast Line-of-sight Atmospheric Analysis of Spectral Hypercube) module. The goal was to eliminate radiometric noise in OLI bands, making them more reliable and allowing for accurate comparison with existing topographic and geological maps.

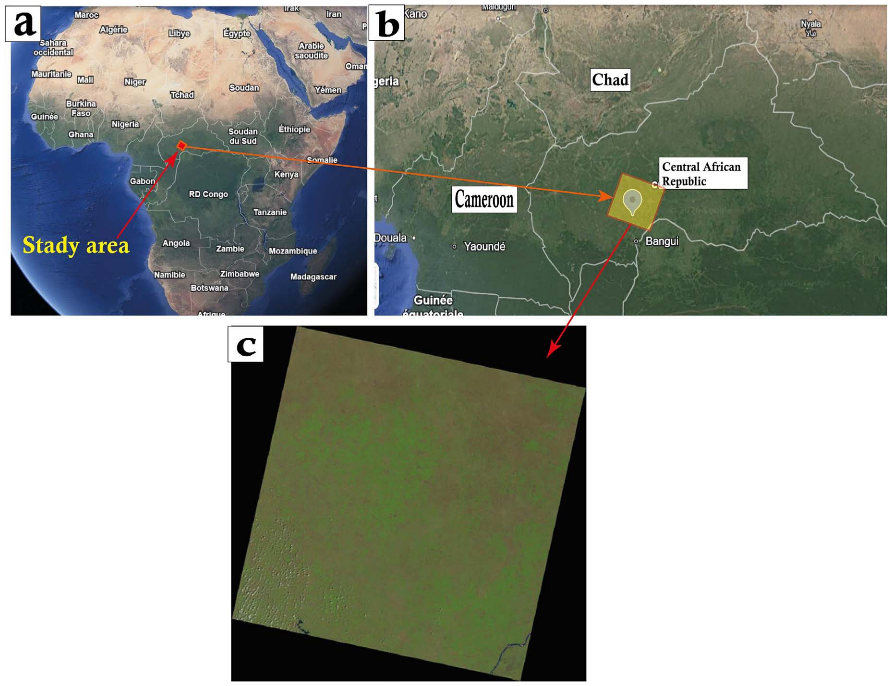

Figure 3. Location of the study area: (a) map of Africa showing the position of Bogoin in central western CAR; (b) and (c) location and extraction of Landsat-8/LDCM scene 180-51. Landsat 8 OLI imagery, USGS Earth Explorer (https://earthexplorer.usgs.gov/), path/row 180-51.

Table 2. Sensor characters of Landsat 8.

Sensor	Bands	Spectral bands	Wavelength (µm)	Spatial resolution (m)
Operational Land Imager (OLI)	1	Coastal	0.433 - 0.453	30
	2	Bleu (visible)	0.450 - 0.515	30
	3	Vert (visible)	0.525 - 0.600	30
	4	Rouge (visible)	0.630 - 0.680	30
	5	PIR	0.845 - 0.885	30
	6	IR moyen	1.560 - 1.660	30
	7	IR moyen	2.100 - 2.300	30
	8	Panchromatique	0.500 - 0.680	15
	9	Cirrus	1.360 - 1.390	30
Thermal Infrared Sensor (TIRS)	10	IR Thermique/lointain	10.6 - 11.2	100
	11	IR Thermique/lointain	11.5 - 12.5	100

For images with significant noise, an inverse Maximum Noise Fraction (MNF) transformation was applied. MNF as defined by Boardman [61] helps determine the eigen dimension of an image, separate noise from useful data, and reduce computational complexity for further processing. This transformation resulted in surface reflectance bands with minimal noise (Figure 5).

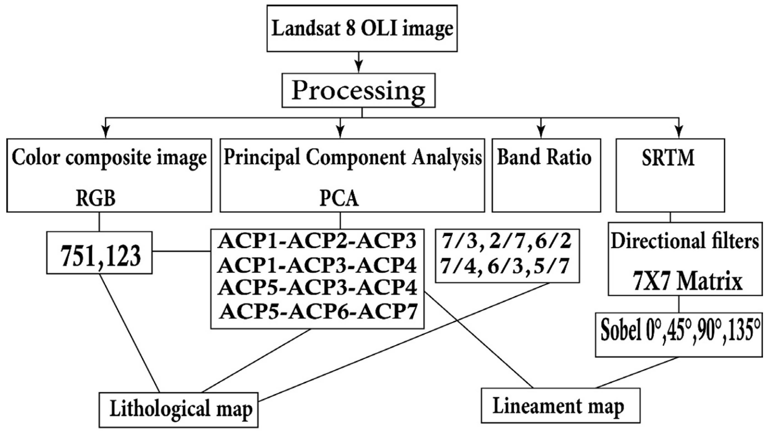

Figure 4. The schematic diagram shows the pre-processing and image processing of the Landsat 8 data for the mapping of geology and lineament structures of the Bogoin region.

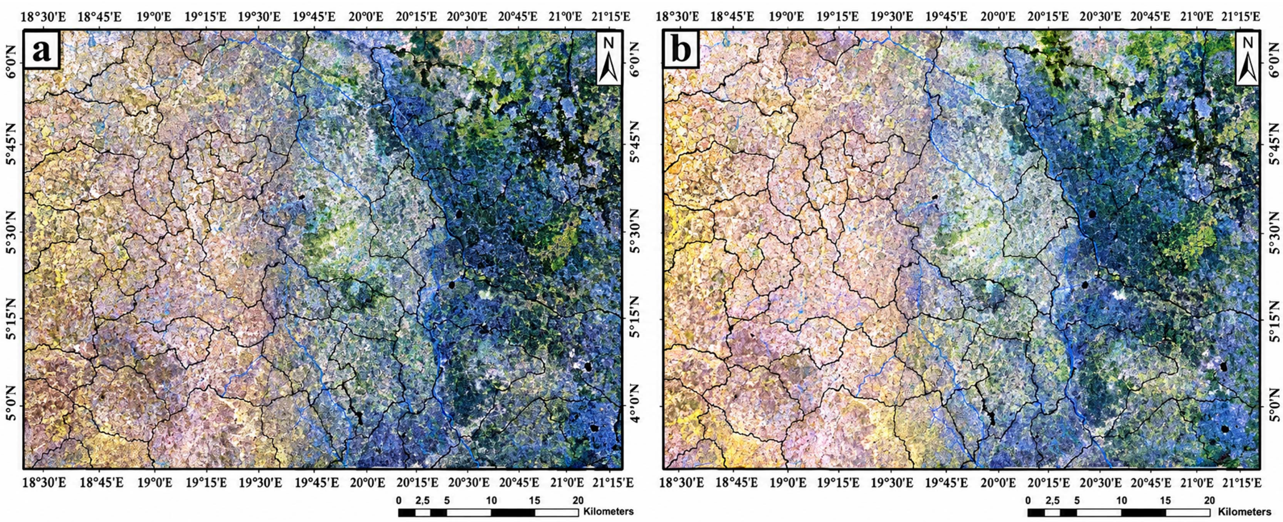

Figure 5. Comparison of (a) raw OLI bands with a lot of noise to (b) combination of b1, b2 and b3 bands pre-processed using FLAASH (Fast Line-of-sight Atmospheric Analysis of Spectal Hypercubes). This gives a clear surface reflectance with less noise and improved interpretability.

3.2.2. False Color Composite

Color compositing is used to generate both true-color and false-color RGB images (Figure 6). In this study, it was applied to highlight lithological units and geological structures. To achieve the most informative color composition, the Optimum Index Factor (OIF) method was utilized. This statistical value, computed using ILWIS software, helps identify the best combination of three spectral bands in the scene. Based on this method, the bands with the highest information content (*i.e.*, the highest sum of standard deviation) were identified as bands 7, 5, and 1 (Table 3). In the final composite, band 7 was assigned to red, band 5 to green, and band

1 to blue. The resulting image was further refined through calibration and spatial enhancement using the panchromatic band, which has the lowest color resolution. This false-color composition, derived from different sections of the electromagnetic spectrum (band 7: mid-infrared 2; band 5: near-infrared; band 1: aerosol), produced high-quality images that effectively distinguished various lithological types (**Figure 6(a)**). Additionally, this composition demonstrated a strong ability to differentiate lithological features compared to the 7/5/2 color composition (**Figure 6(b)**). The signals in the images revealed four key areas based on their color variation: green, light pink, yellow, purple, and grey. Field data confirmed the lithologies corresponding to these colors:

Green: limestone (dominantly carbonate-rich). Purple with red spots: migmatites, diatexite and metatexite. Pinkish: Orthogneisses. Light blue: Chlorito-schist.

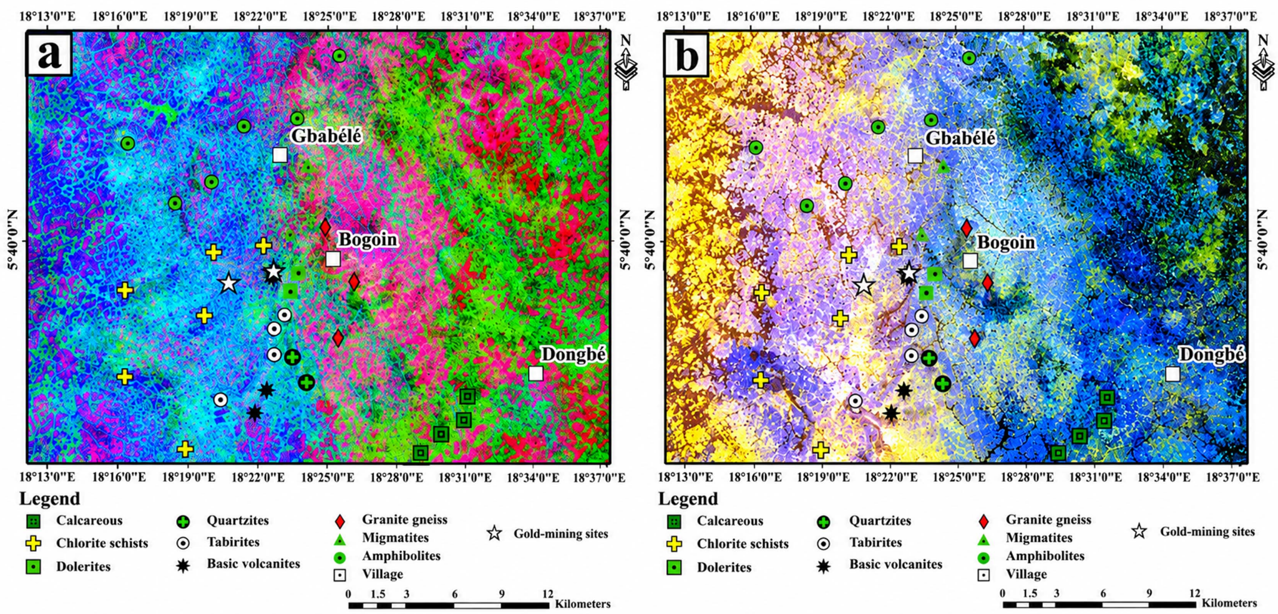

Figure 6. Lithological discrimination. (a) RGB color composition using band combinations 7/5/1; (b) RGB color composition using band combinations 7/5/2. Landsat 8 OLI imagery, USGS EarthExplorer (https://earthexplorer.usgs.gov/).

Table 3. Optimum Index Factor (OIF) of the seven (7) bands.

Highest ranking in the OIF index			
B1	B5	B7	86.74
B2	B5	B7	86. 17
B3	B5	B7	84.82
B4	B5	B7	84.27
B2	B4	B7	83.67
B1	B4	B7	83.56

3.2.3. Band Ratios

The band ratio method helps minimize topographic effects while enhancing the contrast between different mineral surfaces [41] [62]. This technique involves dividing the digital number (DN) of one spectral band by that of another for the same pixel [63]. It significantly improves the clarity of lithological boundaries (**Figure 7**). For this study area, the most effective band ratio combination was identified as (7/3, 2/7, 6/2) and (7/4, 6/3, 5/7) (**Figure 7(a)**, **Figure 7(b)**). Orthogneiss appears in varying tones-purple-blue in **Figure 7(a)** and light-yellow in **Figure 7(b)** corresponding to gneisses on Rolin's [57] geological map (**Figure 2**). Green-red tones indicate migmatites and chlorite schists, as confirmed by field observations. Additionally, the concordant contact between the blue-brown limestone and the orthogneiss, aligned along the fault plane, is distinctly visible (**Figure 7(b)**). According to Rolin and Stussi [64], this limestone is primarily composed of carbonate. To further analyse deformation structure in the Bogoin area, principal component analysis (PCA) and colour composite images were applied. The results obtained through band ratios and field investigations validated PCA. These field data, combined with visual interpretation of Landsat 8 OLI imagery, were used to create a detailed lithological map of the Bogoin area. This new map reveals variations in the distribution of rock units and their contacts compared to previously published geological maps by Rolin [57].

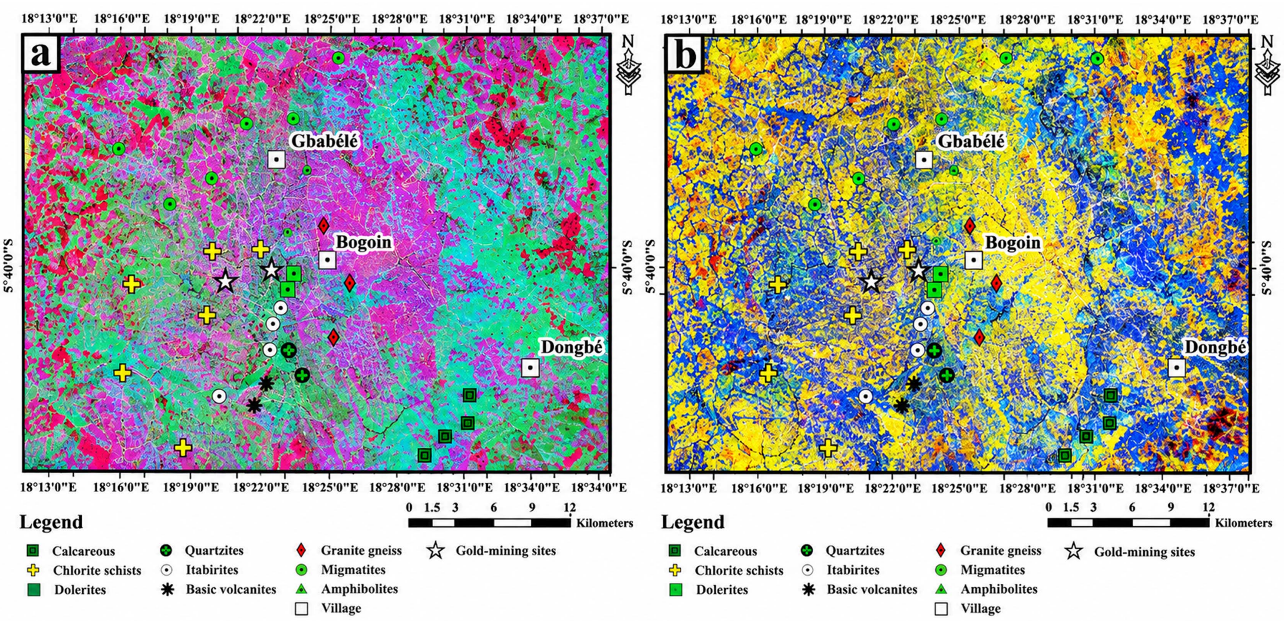

Figure 7. (a) RGB color composition of band ratios 7/3, 2/7, 6/2 [65] shows the different rock types of the Bogoin region; (b) RGB color composition of band ratios 7/4, 6/3, 5/7 [66]. Landsat 8 OLI imagery, USGS EarthExplorer (https://earthexplorer.usgs.gov/).

3.2.4. Principal Component Analysis (PCA)

Principal component analysis is a mathematical technique used to analyze data graphically bands and identify the directions in space that best represent correlations between multiple random variables. This method reduces the number of variables, making the information more concise and less redundant. To map the various lithological units and deformation structures in the Precambrian basement of the Bogoin, we applied PCA to the first seven (7) bands of the OLI instrument, covering the spectrum from visible to mid-infrared 2. This process generated seven principal components: PC1, PC2, PC3, PC4, PC5, PC6 and PC7. The statistical result indicates that band 1 (PC1) contains the highest amount of decorrelated information (Table 4). Additionally, the first three principal components (PC1, PC2, and PC3) provide the most significant information when displayed in RGB mode (Figure 8(a)), with eigenvalues exceeding 0.12.

Table 4. Eigenvector matrix in seven (7) Landsat 8 OLI bands.

Principal component	Band 1	Band 2	Band 3	Band 4	Band 5	Band 6	Band 7
PC1	0.149690	0.155996	0.167843	0.180453	0.213275	0.271205	0.241606
PC2	−0.056032	−0.058945	−0.028310	−0.169430	0.752016	−0.336239	−0.513972
PC3	−0.002993	−0.008739	−0.041015	−0.097688	−0.575547	−0.598686	−0.303180
PC4	0.046269	0.028277	−0.000687	0.102503	0.236703	−0.647892	0.680957
PC5	−0.548124	−0.513237	−0.401263	−0.364247	0.014571	0.122194	0.266583
PC6	−0.516340	−0.244076	0.190502	0.744248	0.002732	−0.039012	−0.171579
PC7	−0.118884	0.001006	0.126139	0.195747	−0.013933	−0.136543	0.128578

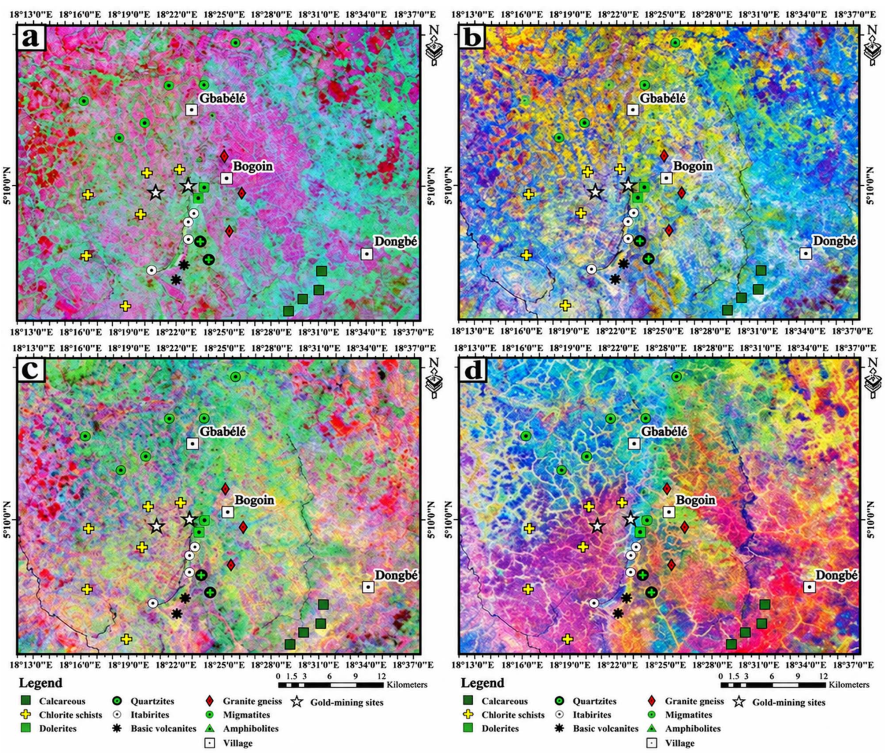

Figure 8. The following compositions highlight key differences in lithological features: (a) PC1-PC2-PC3 captures the maximum information after enhancement using inverse Maximum Noise Fraction (MNF) transformation; (b) PC1-PC2-PC4, providing an alternative colour contrast that helps distinguish the granite gneiss and quartzite units from the surrounding migmatites; (c) PC5-PC3-PC4, which enhances the discrimination of the dolerite and calcareous units in the south-eastern part of the study area; (d) PC5-PC6-PC7, highlighting subtle chromatic contrasts within the chlorite schist and itabirite units that complement the lithological boundaries identified in (a).

3.2.5. Matched Filtering

Directional filters are applied to enhance or suppress specific features in an image based on their texture-related frequency [63] [67] [68] and [41]. This technique modifies pixels' values to generate a new image based on the original data. The main objective of this study is to identify geologically significant lineaments, such as lithological boundaries, dykes, veins, foliations, and faults. To achieve this, the Sobel filter with a 7 × 7 gradient matrix (**Table 5**) was applied to the PC1 band, which contains the most relevant geological information. The filtered images were processed using ENVI software and subsequently exported to ArGiS for lineament extraction and digitization (**Figure 9** and **Figure 10**).

Table 5. Sobel and gradient filter matrices.

Sobel N-S							Sobel E-W						
1	1	1	2	1	1	1	−1	−1	−1	0	1	1	1
1	1	2	3	2	1	1	−1	−1	−2	0	2	1	1
1	2	3	4	3	2	1	−1	−2	−3	0	3	2	1
0	0	0	0	0	0	0	−2	−3	−4	0	4	3	2
−1	−2	−3	−4	−3	−2	−1	−1	−2	−3	0	3	2	1
−1	−1	−2	−3	−2	−1	−1	−1	−1	−2	0	2	1	1
−1	−1	−1	−2	−1	−1	−1	−1	−1	−1	0	1	1	1
Sobel NE-SW							**Sobel NW-SE**						
0	1	1	1	1	1	2	2	1	1	1	1	1	0
−1	0	2	2	2	3	1	1	3	2	2	2	0	−1
−1	−2	0	3	4	2	1	1	2	4	3	0	−2	−1
−1	−2	−3	0	3	2	1	1	2	3	0	−3	−2	−1
−1	−2	−4	−3	0	2	1	1	2	0	−3	−4	−2	−1
−1	−3	−2	−2	−2	0	1	1	0	−2	−2	−2	−3	−1
−2	−1	−1	−1	−1	−1	0	0	−1	−1	−1	−1	−1	−2

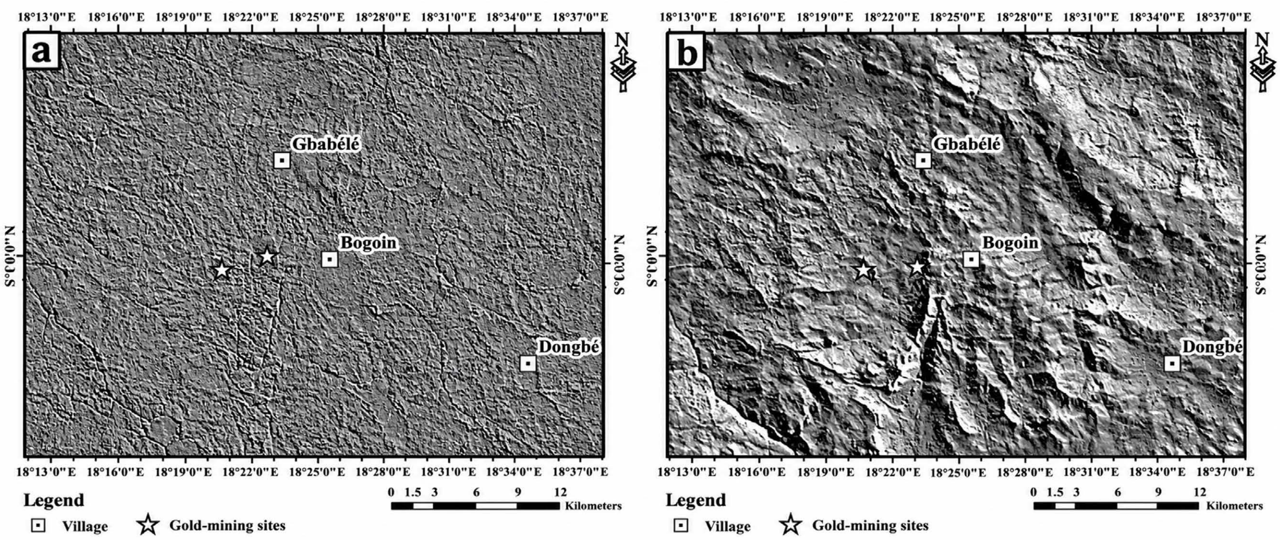

Figure 9. Images from Sobel directional filters. (a) Landsat 8-OLI image; (b) DEM image. To determine the linear discontinuities in the Bogoin area, the Sobel directional filter (0˚, 45˚, 90˚, 135˚) with a 7 × 7 convolution mask on Landsat-8 OLI band 1 and SRTM. Landsat 8 OLI imagery and SRTM Digital Elevation Model, USGS EarthExplorer (https://earthexplorer.usgs.gov/).

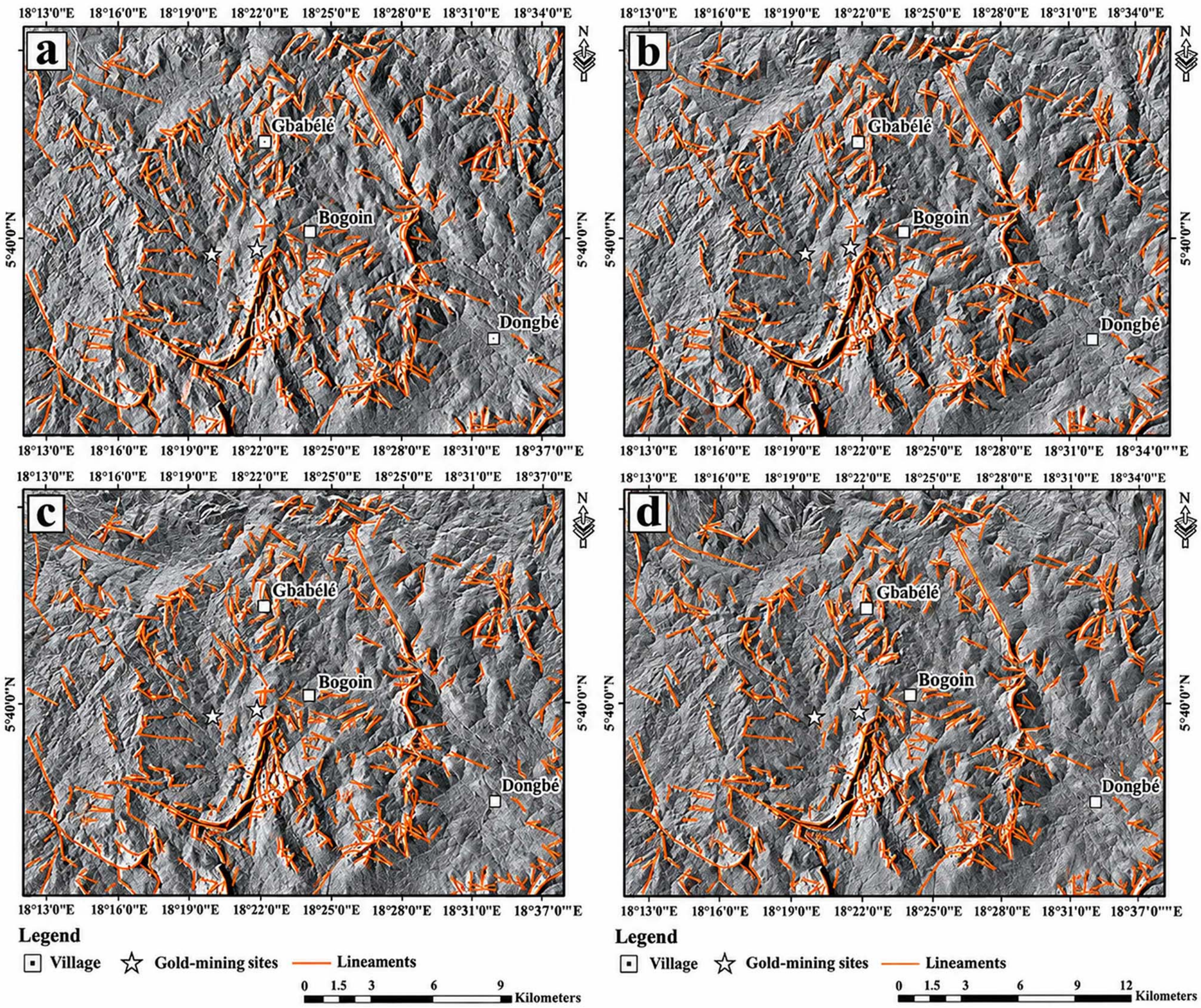

Figure 10. Image from Sobel directional filter. The lineaments largely correspond to river systems, fractures, and contacts between lithologies.

The synthesised lineament map (**Figure 11(a)**) reveals a predominant North-South (N-S) orientation, though it also displays structures with varying directions. The N-S lineaments appear to be the most significant features influencing the study area (**Figure 11(a)**, **Figure 11(b)**). Additionally, the lineament density map illustrates the frequency of lineaments per unit area (**Figure 12(a)**, **Figure 12(b)**). Following various analytical treatments, the lineament map identifies approximately 136 fractures of different lengths, ranging from 0.44 km to 0.92 km (**Figure 12(b)**). The directional rosette corresponding to the lineament map is shown in **Figure 11(a)**. Furthermore, **Figure 11(b)** presents statistical data obtained through automatic lineament mapping using Landsat-8 OLI and SRTM imagery. The analysis indicates that areas with a high density of lineaments are primarily located South and Southwest of Bogoin, in Gbélè, and Northeast of Bogoin (**Figure 12(a)**). The discontinuities identified from satellite images serve as the foundation for a frequency analysis, helping to determine structural orientations, which are then compared with field measurements. A comprehensive statistical analysis reveals three main orientations (**Figure 11(b)**):

1) The dominant N-S orientation, further categorized into two sub-classes: N0˚E and N010˚E.

2) A secondary NW-SE orientation, including two sub-classes N150˚E and N180˚E.

3) A less prominent W-E orientation, with two sub-classes N90˚E and N100˚E.

These findings provide insight into the structural characteristics of the study area, supporting further geological interpretations.

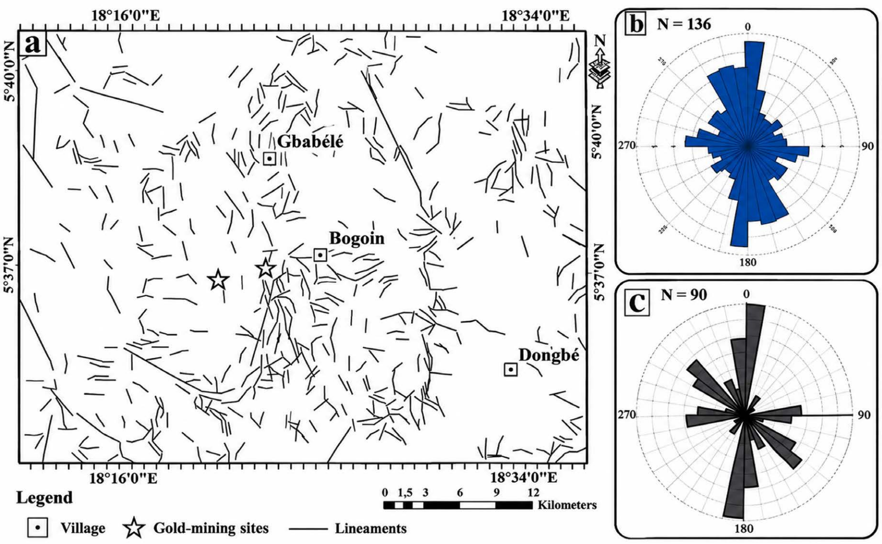

Figure 11. (a) Synthesis map, obtained from the lineament fusion of Landsat 8 OLI and DEM; (b) Rose diagram of lineament synthesis of the study area; (c) The rose diagram of faults, strike-slip, and quartz veins in the study area. Landsat 8 OLI imagery and SRTM DEM, USGS EarthExplorer (https://earthexplorer.usgs.gov/).

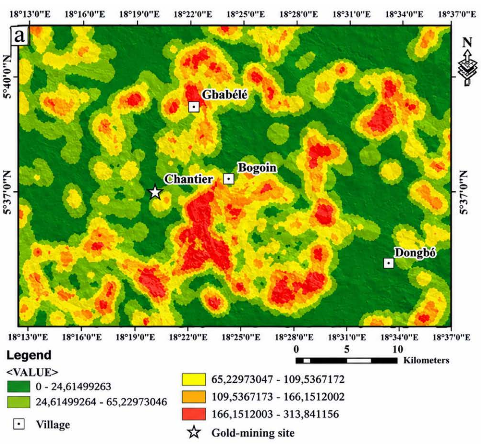

b	Statistical Summary
Calculation Method:	Frequency
Class Interval:	10,0 Degrees
Min.Len Filtering:	Deactivated
Max.Length Filtering:	Deactivated
Azimuth Filtering:	Deactivated
Data Type:	Bidirectional
Population:	1 207
Total Length of All Lineations:	15,75
Maximum Bin Population:	136,0
Mean Bin Population:	67,06
Standard Deviation of Bin Population:	28,0
Maximum Bin Population (%):	5,63
Mean Bin Population (%):	2,78
Standard Deviation of Bin Population (%):	1,16
Maximum Bin Length:	0,92
Mean Bin Length:	0,44
Standard Deviation of Bin Lengths:	0,19
Maximum Bin Length (%):	5,82
Mean Bin Length (%):	2,78
Standard Deviation of Bin Lengths (%):	1,24
Vector Mean:	162,7 Degrees
Confidence Interval:	342,67 Degrees (80 Percent)
R-mag:	0,21

Figure 12. (a) The frequency density map of Bogoin lineaments; (b) A summary of statistical data of lineament synthesis. Landsat 8 OLI imagery and SRTM DEM, USGS EarthExplorer (https://earthexplorer.usgs.gov/).

4. Results and Discussion

4.1. Results

4.1.1. Petrography

1) Condition of outcrop

The Bogoin area is a vast, undulating plain with an average altitude of 700 m, from which rise the Inselberg mountains. These massifs are gullied by a highly branched network of seasonal streams. They are composed of isolated hills, with V-shaped valleys between them, and are occupied by watercourses with almost rectilinear beds, bearing witness to the intense fracturing in the area. On the hillsides, basement formations outcrop in the form of slabs, boulders, and balls, presenting a chaotic landscape. In the valleys, the basement formations are found in the river beds.

Petrographic analyses enabled us to distinguish the different lithological units in the study area, namely, itabirites, amphibolites, micaschists, migmatites, dolerite dykes, orthogneiss, metavolcanites, quartzites, chloritoschists, and calcareous rocks.

2) Amphibolites

Amphibolites are the most common type of metamorphic rock formed by regional metamorphism, characterised by high pressure and temperature. Amphibolites are generally associated with micaschists and gneisses (**Figure 13(a)**). Schistosity formation in amphibolites is much less pronounced than in amphibole schists. Amphibolites outcrop in the northern part of Bogoin. They have massive, schistose structures. The structure of amphibolites is mainly influenced by the almost parallel alignment of prismatic hornblende crystals. The rocks often have a schistose appearance due to the semi-parallel arrangement of narrow bands, mainly composed of hornblende and plagioclase. They are dark in colour, with a medium to coarse texture. Microscopic observations show heterogranular and nematoblastic microstructures comprising approximately 60% amphibole, 12% biotite, 20% plagioclase, and 8% quartz (**Figure 13(b)**). Amphibole is represented by hornblende crystals containing inclusions of opaque minerals. It is subhedral to euhedral in grain size. Quartz is present in the form of xenomorphic crystals ranging in size from 0.1 to 0.2 mm; some of these crystals are rounded while others are elongated (**Figure 13(b)**). Plagioclase has hypidiomorphic grains with irregular boundaries and is characterised by local zonation (1.2 mm × 2.7 mm). This mineral occurs both as individual grains and in clusters next to the amphibole. Biotite crystals are millimeter-sized. Opaque minerals are euhedral and vary in size and shape.

3) Mica-schist

Mica-schists are the most common type of metamorphic rock formed by regional metamorphism, characterised by high pressure and temperature (**Figure 13(c)**). They are generally associated with mica-schist and mica. Schistosity formation in mica-schist outcrops is much more highly pronounced in the northern part of Bogoin. They have massive, schistose structures. The structure of mica-schist is mainly influenced by the almost parallel alignment of prismatic muscovite crystals. The rocks often have a schistose appearance due to the semi-parallel arrangement of narrow bands, mainly composed of muscovite, biotite, quartz, and feldspar. They are silver-grey in colour, with a medium to foliate texture. Microscopic observations show heterogranular microstructures comprising approximately 24% plagioclase, 25% biotite, 15% microcline, 26% quartz, and 10% muscovite (**Figure 13(c)**, **Figure 13(d)**). Muscovite is represented by hornblende crystals containing inclusions of opaque minerals.

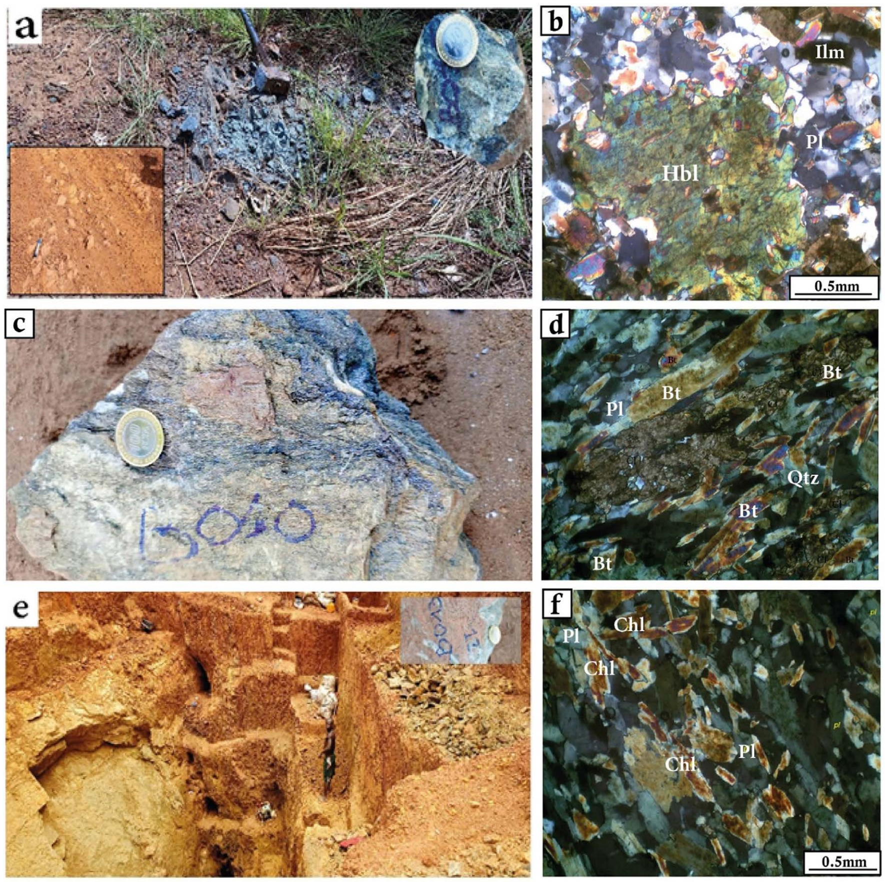

Figure 13. Field photographs and photomicrographs of representative samples of the Bogoin showing field relationships, textures, and mineralogical composition: (a) (b) Amphibolites are generally associated with mica-schists and gneisses. In cross-polarized light, the amphibolite shows a grano-nemato-lepidoblastic texture; (c) (d) Mica-schist. In cross-polarized light, it exhibits heterogranular microstructures; (e) (f) Chlorite schist. In cross-polarized light, it is characterized by a layered texture (schistosity) dominated by green minerals.

4) Chlorite-schist

The chlorite-schist outcrop is in slab-like formations that break into thin sheets. It exhibits a schistose texture with an abundance of chlorite, often associated with epidote and plagioclase (albite), and sometimes sericite, revealing intermediate-level metamorphism, often derived from mafic rocks such as metagabbros. It has a greenish hue and constitutes the dominant lithology of the gold mining area (**Figure 13(e)**). These rocks are intersected by synschistose veins, which are typically mineralized with gold.

Under a polarizing microscope (**Figure 13(f)**), chlorite schist is characterized by a layered texture (schistosity) dominated by green minerals (chlorite), often occurring as aggregates or flakes, exhibiting abnormal interference colors and pleochroism ranging from pale green to dark green, associated with other minerals such as quartz, muscovite, and albite.

5) Itabirite (Banded Iron Formations)

It occupies the western part, forming high hills (over 900 meters), and runs along the northern and southern parts of the region with a dip of 70 to 80˚W. Some of these itabirites are massive, while others consist of alternating beds of dark minerals composed of iron oxide (hematite, magnetite) and finely crystallized white minerals (quartz) with color variations ranging from grey-white to metallic black. Under microscopic examination, BIFs are typically identified by alternating grey-white quartz-rich and dark magnetite-rich bands (**Figure 14(a)**). These bands display a granoblastic microstructure (**Figure 14(b)**). The composition includes quartz ribbons constituting approximately 25% - 35% of the material, forming the silica-rich layers, along with euhedral and subhedral-shaped magnetite crystals (around 25% - 30%), plagioclase (about 4%), hornblende (8% - 25%), and minor amounts of disseminated limonite (approximately 4%) and sericite (around 1%) as accessory phases. These BIFs exhibit paragenesis that ranges from greenschist facies (Mgt + Qtz ± Pl + Ser ± Lm) to amphibolite facies (Mgt + Qtz ± Pl + Hbl ± Ser ± Lm).

6) Metadiorite

In the Bogoin area, metadiorite is situated along the right bank of the Ngbelet stream, exhibiting a gray color, coarse-grained and a gritty structure (**Figure 14(c)**). Minerals including quartz, biotite, amphibole and K-feldspar display NW-SE preferred orientation. Under microscope, metadiorite show plagioclase (14%), zoned and twinned K-feldspars (orthoclase 5% and 8% microcline), quartz with poecilitic textures wavy extinction amphibole (30%), biotite (10%) (**Figure 14(d)**) and ilmenite (10%).

7) Orthogneiss

Orthogneiss represents the main lithological unit of the locality of Bogoin, where the rock is intersected by late magmatic proto- dykes, two-mica pegmatite dykes, and dykes. This is a heterogeneous always oriented texture, especially at the contact with the quartzo-schistose series, where the textures are frankly gneissic (**Figure 14(e)**). It is medium to fine-grained, grey in colour, sometimes pink to red due to the presence of pinkish potassium feldspar, and contains enclaves of amphibolites. It consists of quartz, K-feldspars, including subautomorphic to xenomorphic orthoclase or microcline (**Figure 14(f)**), plagioclase which sometimes shows both albite and Carlsbad twinings, quartz which crystallizes in the microfractures of feldspar, biotite flakes containing apatite and zircon inclusions, some muscovite and epidotes especially found in the quartz-schistose contact, sericite and ilmenite. However, an average facies is impossible to define, as grain and texture can vary greatly even in the same outcrop. The rock is cut across by quartz-feldspar-rich veinlets sometimes showing a few biotite clusters and local pegmatitic folds.

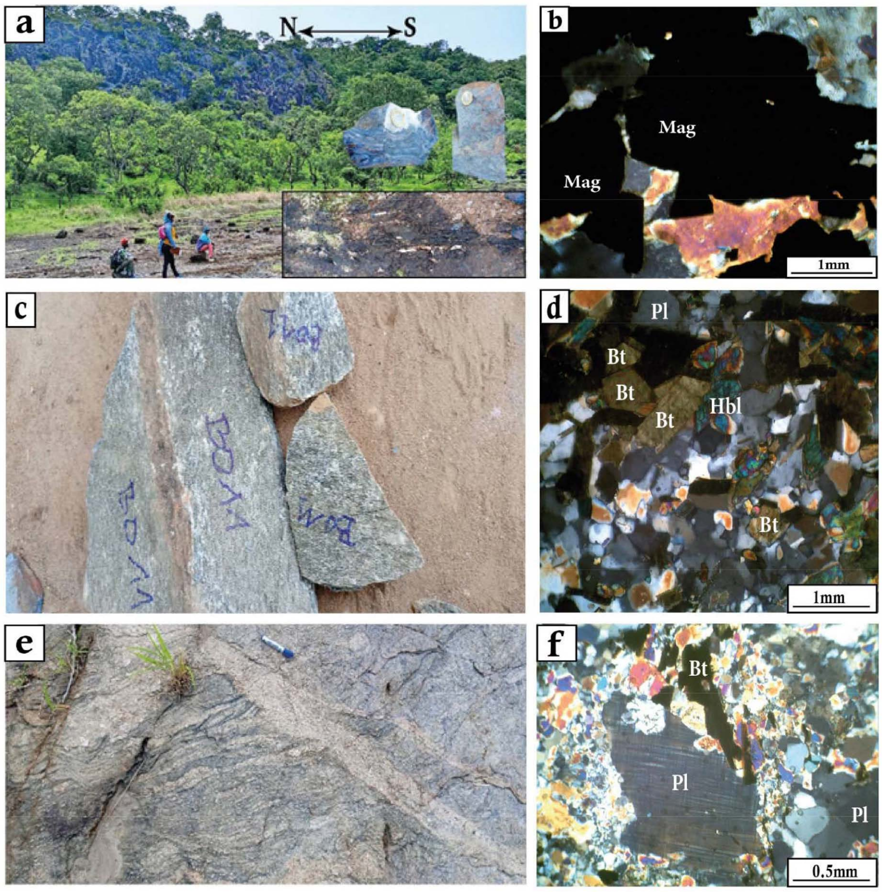

Figure 14. (a) (b) Itabirite (Banded Iron Formations). In cross-polarized light, it is typically identified by alternating bands of quartz-rich grey-white areas and magnetite-rich dark sections; (c) (d) Metadiorite. It is characterised by plagioclases, amphiboles, biotites and a small amount of quartz with poecilitic textures; (e) (f) Orthogneisses (granitic gneisses). Alkali feldspar crystals are either subautomorphic to xenomorphic orthoclase or microcline.

4.1.2. Structural Analysis

1) Fabric elements and folds

Structural features were observed in orthogeneiss, chloritoschist, itabirites, and dolerite dykes. The structural elements identified are foliation, mineral elongation lineation, folds, boudins, shearing, quartz veins, and diaclases grouped under three deformations phases D1, D2 and D3.

The D1 deformation event is characterized by the S1 bedding plane being overprinted by alternating millimetric to centimetric light quartz-feldspars rich bands and dark, milli-metric ferromagnesian minerals rich bands (**Figures 15(a)-(f)**).

The S1 foliations are found sporadically in the migmatitic gneisses to the west of Bo-goin. This original S1 foliation is poorly preserved and almost completely transposed into S2 foliation due to the strong D2 overprint (**Figure 15(b)**) characterized by leucomorph and melanosome macrozoning (**Figure 15(a)**, **Figure 15(b)**) to microzoning, and granitic gneisses, amphibolites, greenschists, and itabirites are visible. S1 is oriented NW-SE in gneiss and has moderate to steep dips (55˚ to 80˚) to the NE or SW (**Figure 15(a)**). The F1 folds are found in gneiss where it is strongly overprinted by the F2 folds (**Figure 15(c)**, **Figure 15(d)**). However, the stereographic projection shows that the overall trend of the F1 fold is NW-SE.

The D_2 event is characterized by S_2 mylonitic foliation (**Figure 15(b)**) and F_2 folds (**Figure 15(d)**). The S_2 foliation (**Figure 15(f)**) is highlighted by elongated, aligned or extended mineral bands of hornblende, K-feldspar, plagioclase, quartz, and magnetite (**Figure 15(e)**). The S_2 direction shows slight N-S to NNE-SSW variations and is associated with the foliation planes visible in the migmatitic gneisses, amphibolites, chlorito-schists and itabirites that underwent mylonitic shear deformation. This strong secondary planar structure is considered to be the most important structural foliation observed in the Bogoin Greenstone Belt, with an average strike of N0˚ and N05˚ and an average dip of 30˚ (**Figure 15(d)** and **Figure 15(f)**, respectively). Transposition of the NW-SE (N145˚E) foliation (S_1) into N-S (N05˚E) foliation (S_2) is observed along dextral shear planes in the migmatitic gneisses (**Figure 15(b)**). This shear deformation is also characterized by F_2 folds, asymmetrical boudins B_2 of the K-feldspar porphyroclasts parallel to the S_2 structure (**Figure 15(e)** and **Figure 15(f)**) [69] [70], and crenulation cliveage in the rock. L_2 stretching mineral lineation is observed in the mylonitic migmatitized gneisses of Bogoin. It is marked by NNE-SSW alignment of stretched and elongated biotite flakes and quartz ribbons on the foliation planes with gentle plunges between 05 and 10˚ towards the ESE and WNW (**Figure 15(a)**). F_2 folds are isopac folds, anisopac folds, and ptygmatitic. Isopac folds are generally observed in the migmatitic gneisses of Bogoin, where they have an amplitude of up to 7 cm and a wavelength varying between 3 and 5 cm. Their axes are oriented N05˚E with a slight dip towards SSW or NNE (**Figure 15(d)**, **Figure 15(e)**). The anisopac folds are remarkable for their stretched and laminated flanks, as well as for their thickened hinges in the migmatitic gneisses and itabirites, where they are underlined by quartzo-feldspathic levels. Their axes display N-S trend and N or S moderate (02˚ - 50˚) plung (**Figure 15(e)**, **Figure 15(g)**, **Figure 15(l)**) sub-parallel to the lineation of mineral elongation. Ptygmatic or disharmonic folds are observed in migmatitic gneisses where they are underlined by very tight hinges quartzo-feldspars rich vein (**Figure 15(c)** and **Figure 16(a)**).

Thrust observed indicates sinistral (**Figure 16(b)**) or dextral (**Figure 16(d)**) movement. The faults observed affect the quartz veins, which they displace regularly along horizontal planes. The rose diagrams of fault planes in the study area shows a major direction between N150˚E-N180˚E and N0˚E-N10˚E. The minor directions are N90˚E to N100˚E.

The "C2" shear planes are marked as sinistral movement display by quartz-feldspars veins (Figure 15(b), Figure 15(c), Figure 15(e), Figure 15(f), and Figure 16(c)). These shear patterns determine a rhythmic division of the rock, allowing the foliation to be reorganized into microliths (Figure 15(b)).

The D_3 deformation phase is characterized by faults, tension fractures, and normal dip-slip faults that intersect markers from previous geological events. These fractures predominantly exhibit NW, N-S, and NNE-SSW orientations. Notably, the main strike directions identified include N-S, NNE-SSW, NNW-SSE, ENE-WSW, WNW-ESE, and NW-SE, as recorded from minor faults as well as tension gashes and tension fractures.

The faults observed affect the quartz veins, which they displace regularly along horizontal planes. The rose diagrams of fault planes (Figure 17) show a major direction between N0˚E-N10˚E, N90˚E, and N150˚E. The minor directions are N20˚E to N100˚E. Fault planes are often marked by dry shear joints; these planes are often curved and are marked by the rerouting of the foliation and sometimes by the unhooking of veins on either side of the plane, thus indicating a dextral shear movement. Fault planes observed in the study area are centimetric dry joints that strike other dry joints or quartz lenses displaying sinistral movement. The dry joints observed in the orthogneiss (mylonites), migmatites, and dolerite dykes vary in length from centimeters to several tens of meters. The rose diagram of joints (Figure 11(c)) in the lithological units in the study area reveals three main directions: N-S, N90˚E, and N150˚E.

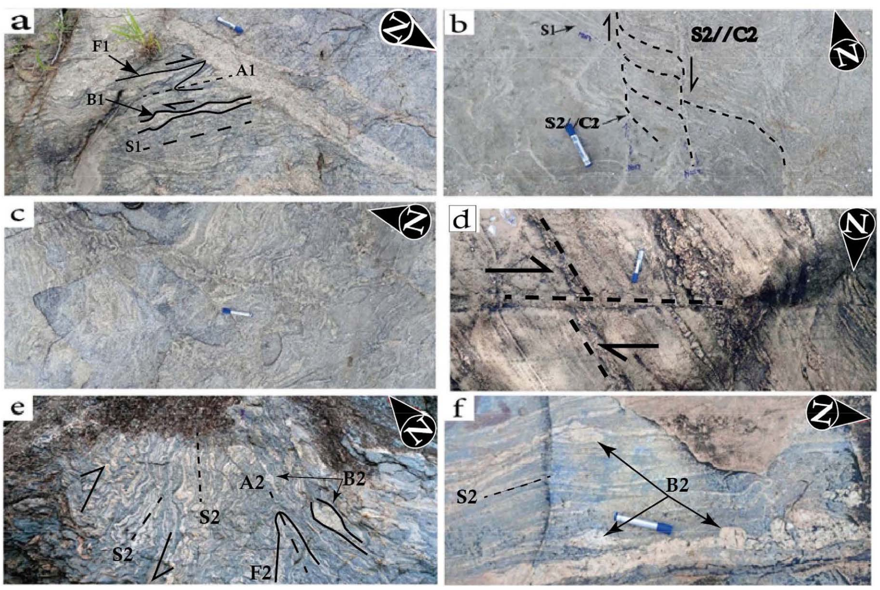

Figure 15. Field views of main structural elements in the Bogoin area. (a) Presence of a syn-schistose fold (F1) associated with first-generation fold axes (A1); (b) Ductile shear zone showing bending of previous schistosity/foliation planes (S1) towards a new parallel orientation (S2//C2); (c) Ptygmatic or disharmonic folds are present in migmatitic gneisses; (d) dextral C2 shear planes are associated with the de-velopment of S2 mylonitic foliation; (e) B2 Boudins and F2 folds are present in the Itabirites; (f) B2 Boudins are present in the or-thogneiss.

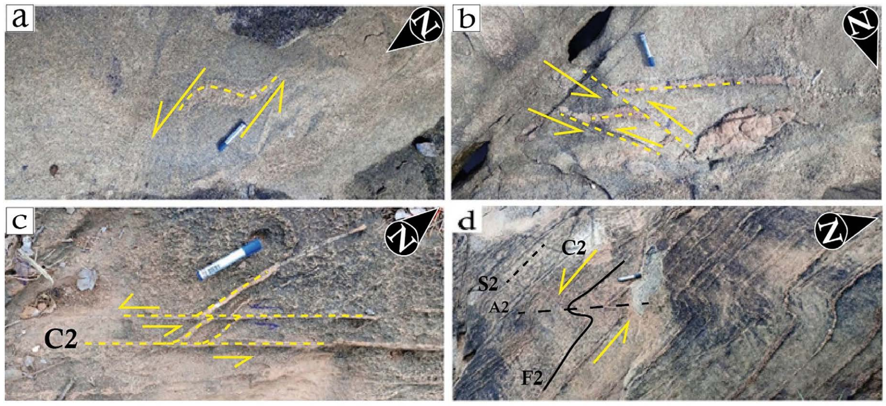

Figure 16. Field views of main structural elements on Bogoin area. Sinistral C2 shear plane associated with the development of S2 mylonitic foliation. (a) Ptygmatic (disharmonic) folds with tight hinges in quartzo-feldspathic veins within migmatitic gneisses; (b) sinistral C2 shear plane marked by folded and offset quartz-feldspar veins, indicating a sinistral sense of shear; (c) sinistral C2 shear planes highlighted by dis-placed quartz-feldspar veins; (d) dextral C2 shear plane associated with the F2 fold hinge (A2 axial plane) and S2 mylonitic foliation (S2), indicating a dextral sense of movement.

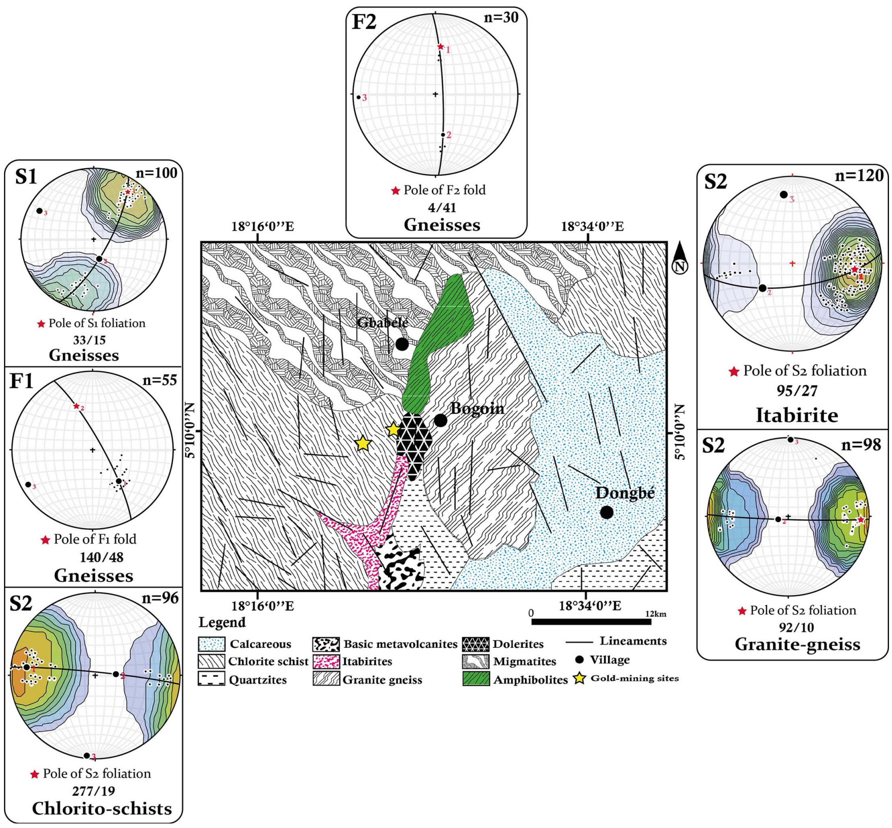

Figure 17. Litho-structural map of Bogoin. Base map: Landsat 8 OLI imagery, USGS EarthExplorer (https://earthexplorer.usgs.gov/); structural data compiled from field measurements by the authors.

4.1.3. Geochemical Results

1) Granitic gneisses (Orthogneiss)

a) Major elements

The bulk geochemical composition (major elements) of two representative samples of the granitic gneisses is listed in **Table 6**. The gneissic host rock associated with the Itabirites (IFs) for this study is orthogneiss. The geochemical characteristics of the granitic gneisses, notably the high silica content (68.72 - 71.44 wt.% SiO_2), combined with elevated alkali oxide ($Na_2O + K_2O$ = 8.16 - 8.29 wt.%), clearly indicate a felsic to intermediate magmatic origin. The granitic gneiss complex shows high Al_2O_3 ranging between 14.31 and 16.22 wt.%, reflecting a significant proportion of aluminium-bearing minerals such as K-feldspars and micas typical of felsic to intermediate rocks; the low MgO varies from 0.43 to 0.76 wt.%, indicating limited to moderate amounts of mafic minerals (*e.g.*, biotite, amphibole) within the granitic gneiss complex; and CaO concentrations range from 1.81 to 1.97 wt.%, consistent with the presence of calcic plagioclase feldspars supporting a granitoid composition with a balanced feldspar assemblage. These values collectively confirm the granitic-gneiss nature of the Bogoin complex, reflecting felsic-to-intermediate magmatic protoliths with some mafic mineral input, likely modified by high-grade metamorphism. **Figure 18(a)** shows the granitic gneisses plot in the granite field. Geochemical analyses of the sampled rocks revealed an A/CNK index value of 0.9 to 1.0, placing the samples at the boundary between the metaluminous and weakly peraluminous fields. This value suggests a magmatic origin with a calc-alkaline affinity, characteristic of I-type granitoids. It reflects a magmatic source likely derived from the partial melting of the lower crust or an enriched mantle within an orogenic tectonic setting typical of continental magmatic arcs. The absence of significant alumina oversaturation also suggests that aluminous minerals such as muscovite or garnet are not dominant in the primary mineral assemblage. Based on the geochemical classification for granitic rocks by Frost [71], samples displayed magnesian and metaluminous to peraluminous signatures like those described and dated by Djibril [72] (**Figure 18(b)** and **Figure 18(c)**).

b) Trace elements

Trace element concentrations in gneiss presented in **Table 6** show enrichment in light rare earth elements (LREE) (e.g., high La/YbCN: 30.20 - 90.13; CN stands for chondrite-normalized) and strong depletion in HREE (*e.g.*, low Yb: 0.32 - 0.75 ppm) with negative to weak positive Eu anomalies (Eu/Eu* = 0.40 - 1.1) (**Figure 18(d)**). In the primitive mantle-normalized multi-element spider diagrams, gneiss displays significant LILE positive and Nb, Ta, and Ti negative anomalies (**Figure 18(e)**). We can notice the conformity of the spider in gneiss of Mewengo iron deposits to suggest that they are identical (**Figure 18(d)** and **Figure 18(e)**).

c) Rare Earth Element (REE)

Chondritic normalized [77] REE concentrations of in gneiss, show a clear enrichment of LREE over HREE (La_{CN}/Yb_{CN} = 30.20 - 90.13). In addition, all samples show a negative to slightly positive europium anomaly (Eu/Eu* = 0.40 - 1.1; **Figure 18(d)**). Gneiss exhibit trace element and REE signature typical of evolved crustal magmatic sources, including LILE high concentrations e.g. Ba (598 - 1625 ppm) and Sr (131 - 489 ppm), Zr (179 - 188 ppm) and K_2O (3.26 - 4.03 wt.%), suggest derivation from a fertile continental crustal source, likely through low-degree partial melting of metasedimentary or lower crustal protoliths. It has a high content of light rare earth elements (LREE = 120.9 - 135.2 ppm) and a low content of heavy rare earth elements (HREE = 1.8 - 4.0 ppm).

Table 6. Trace and rare earth element compositions and element ratios of study rocks from Bogoin Area.

Rock type	Orthogneisses (granitic gneisses)		Itabirite (Banded Iron Formations)			Amphibolites			Metadiorite
Sample	**BO2**	**BO12**	**BO5A**	**BO5B**	**BO5C**	**BO10A**	**BO15**	**BO13**	**BO11**
SiO_2	71.44	68.72	1.08	1.43	1.28	40.15	50.05	46.73	60.98
Al_2O_3	14.308	16.223	0.316	0.416	0.478	6.572	7.718	7.673	14.035
Fe_2O_3	1.962	2.443	97.54	97.285	97.895	13.837	14.78	14.31	6.635
MnO	0.0279	0.0283	n.d.	n.d.	0.0176	0.1859	0.2327	0.2288	0.0938
MgO	0.432	0.763	n.d.	n.d.	n.d.	11.345	11.29	15.905	4.965
CaO	1.813	1.971	n.d.	n.d.	n.d.	12.48	12.1	9.61	4.606
Na_2O	4.255	4.903	n.d.	n.d.	n.d.	0.462	1.408	0.519	3.261
K_2O	4.033	3.257	n.d.	n.d.	n.d.	1.802	0.136	0.044	3.438
TiO_2	0.194	0.319	n.d.	n.d.	n.d.	0.635	0.682	0.647	0.493
P_2O_5	n.d.	n.d.	n.d.	n.d.	n.d.	n.d.	n.d.	n.d.	0.31
LOI	0.44	0.7	0.08	0.2	0.18	8.44	1.13	4.01	1.12
Total	98.9	99.33	99.02	99.33	99.85	95.91	99.53	99.68	99.93
Mg#	30.37	38.22	0	0	0	61.89	60.21	68.77	59.72
Na_2O/Al_2O_3	0.30	0.30				0.07	0.18	0.07	0.23
K_2O/Al_2O_3	0.28	0.20				0.27	0.018	0.0057	0.24
As	0.507	0.5617	11.66	187.13	24.64	21808.64	141.05	818.35	1.78
Ba	597.6755	1308.553	10.5038	11.2235	19.1254	413.2277	17.471	17.759	1625.3558
Be	1.3203	0.8408	0.0925	0.1111	0.0978	0.3699	0.601	0.2918	1.5905
Bi	0.1648	0.117	0.1577	0.4243	0.1802	2.9764	0.2016	0.241	0.2583
Cd	0.0463	0.0337	n.d.	n.d.	n.d.	0.3968	0.1366	0.6561	0.0497
Co	2.4295	4.5923	0.3463	0.4513	0.4236	48.452	71.4767	30.7299	22.1612
Cr	9.4843	4.2477	10.9194	9.7073	11.6803	532.6181	655.8544	1456.1059	186.1654
Cs	2.3932	1.1899	0.0339	0.0291	0.0338	48.8943	0.3621	0.0819	2.7846
Cu	2.8445	3.4207	5.2676	n.d.	n.d.	114.6061	37.3745	6.0405	34.1949
Ga	18.4306	20.6327	1.5289	1.5081	1.5447	11.1358	12.08	11.9907	18.6661
Ge	0.9237	0.6758	3.8584	3.7207	3.9189	1.2843	1.7282	2.5627	1.3478
Hf	5.8801	4.0735	0.086	0.0861	0.1089	1.0365	1.5026	1.7084	4.9074
In	n.d.	n.d.	n.d.	n.d.	n.d.	0.0523	0.055	0.043	0.0346

Continued

Mo	n.d.	n.d.	1.0584	1.0187	1.0514	1.6965	n.d.	n.d.	0.5055
Nb	6.7464	2.3149	0.1656	0.1622	0.1877	1.9936	1.799	2.4668	5.2622
Ni	4.7478	3.4124	5.3157	5.0164	4.911	369.8265	257.4621	436.2907	88.3505
Pb	37.26	17.2828	1.5249	1.9661	1.8846	2928.8094	17.207	3.3949	17.4461
Rb	137.6124	118.6252	0.4951	0.4999	0.5398	79.3067	2.4883	0.2393	120.5378
Sb	n.d.	n.d.	22.3286	20.3144	21.9576	27.2263	1.3248	0.6224	0.1169
Sc	3.33	2.33	0.64	n.d.	0.81	24.39	34.79	22.73	15.09
Sn	1.3142	0.9601	n.d.	n.d.	n.d.	0.8818	0.5579	0.3721	0.944
Sr	131.3601	489.314	3.0177	2.3037	4.72	54.11	127.3917	6.4811	451.2445
Ta	0.8868	0.1394	0.0421	0.0122	0.0196	0.152	0.1761	0.2393	0.5009
Th	39.1787	8.6088	0.1579	0.2029	0.2369	0.511	1.1716	1.077	16.2079
U	5.9861	0.6924	1.0887	1.0307	1.1537	0.14	0.2683	0.4079	3.0718
V	9.5812	18.3558	22.6404	21.8523	22.1438	168.778	218.6699	154.6458	108.5286
W	n.d.	n.d.	8.9502	8.6191	8.9356	91.5845	n.d.	n.d.	n.d.
Y	7.8245	3.8664	12.0037	25.7607	8.2294	14.9322	24.5296	330.2674	14.1267
Zn	40.4869	45.5156	n.d.	n.d.	n.d.	350.4179	134.0997	197.9085	64.5722
Zr	188.2105	178.8766	5.849	6.1122	7.1893	37.8972	54.0375	62.4766	186.5088
La	33.237	42.8426	2.277	2.0273	3.1355	3.9723	11.6104	57.7437	42.8818
Ce	57.9251	64.7105	5.4641	8.7653	11.8848	9.1878	13.2474	25.1279	77.651
Pr	6.0231	6.4615	0.4681	0.4566	0.7007	1.2926	3.5765	23.7369	8.7962
Nd	19.9598	19.1021	2.1128	1.9829	2.9089	5.8996	15.9966	106.2505	31.5192
Sm	3.7418	2.0425	0.5085	0.6385	0.6336	1.8329	4.2106	28.4828	5.3954
Eu	0.4379	0.6017	0.2771	0.4331	0.2682	0.6487	1.4453	9.3083	1.3739
Gd	2.788	1.1818	1.3427	2.2621	1.1038	2.21	4.7124	37.2157	3.7696
Tb	0.3378	0.1347	0.221	0.4404	0.178	0.382	0.7884	7.0529	0.4894
Dy	1.6447	0.7072	1.544	3.0153	1.1241	2.5413	4.8259	47.6171	2.6482
Ho	0.3001	0.1408	0.3444	0.7248	0.2541	0.5539	0.9933	10.7229	0.5358
Er	0.7482	0.3867	0.9256	1.9094	0.6012	1.493	2.5174	28.7935	1.4168
Tm	0.1135	0.0537	0.109	0.2566	0.0775	0.2165	0.361	4.064	0.2109
Yb	0.7476	0.3229	0.6821	1.4734	0.458	1.446	2.2408	23.7677	1.3707
Lu	0.1149	0.0474	0.1028	0.2287	0.0715	0.2194	0.3319	3.6498	0.2086
REE	139.274	144.9325	29.0229	50.3751	32.4393	71.2182	126.1775	766.5311	207.4842
(La/Yb)CN	30.20	90.13	2.27	0.93	4.65	1.87	3.52	1.65	21.25
(La/Sm)CN	5.55	13.10	2.80	1.98	3.09	1.35	1.72	1.27	4.96
(Gd/Yb)CN	2.92	2.87	1.54	1.20	1.89	1.20	1.65	1.23	2.15
Eu/Eu*	0.40	1.11	0.99	1.01	1.00	1.001	1.005	0.89	0.89
Ce/Ce*	0.87	0.78	1.12	2.00	1.77	0.97	0.49	0.17	0.88

Continued

Nb/Th	0.17	0.27	1.048	0.80	0.79	3.90	1.53	2.29	0.32
Nb/Ta	7.61	16.61	3.93	13.29	9.58	13.12	10.22	10.31	10.50
Nb/La	0.20	0.05	0.07	0.08	0.06	0.50	0.15	0.04	0.12
Ce/Yb	77.48	200.40	8.01	5.95	25.95	6.35	5.91	1.06	56.65
Th/Yb	52.40	26.66	0.23	0.14	0.52	0.35	0.52	0.045	11.82
Nb/Yb	9.02	7.17	0.24	0.110	0.41	1.38	0.80	0.10	3.84
Nb/U	1.13	3.34	0.152	0.16	0.16	14.24	6.70	6.047	1.713
(La/Sm)PM	5.73	13.541	2.89	2.05	3.19	1.40	1.78	1.31	5.13

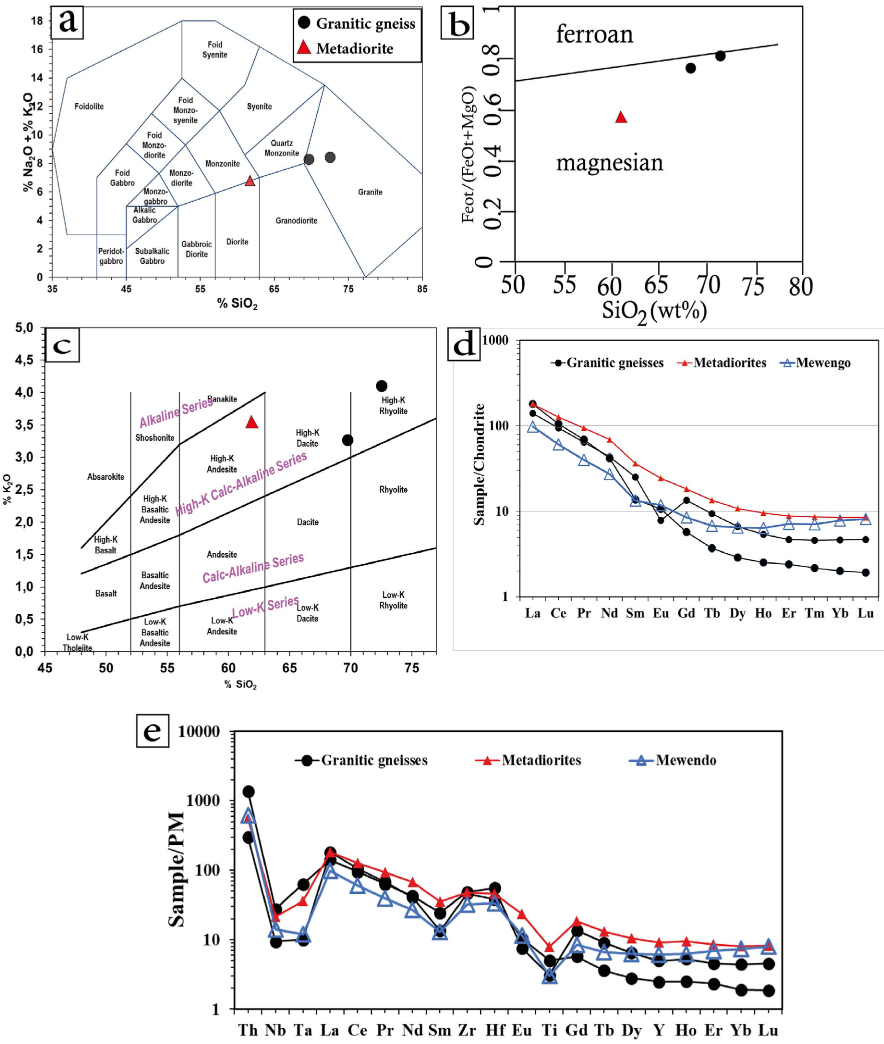

Figure 18. (a) TAS diagram showing the granitic composition of the protolith after [73]; (b) geochemical classification for granitic rocks by Frost [71], samples displayed a magnesian signature; (c) SiO_2 vs. K_2O diagram showing a high-K calc-alkaline series for Bogoin gneisses (after [74]); (d) (e) Chondrite-normalized [75] rare earth element (REE) patterns and primitive-mantle-normalized [76] multi-element plots (a) (b) granitic gneisses and metadiorites.

2) Metadiorite

a) Major elements

Compared to granitic gneiss (SiO_2 68.72 - 71.44 wt%; Al_2O_3 14.31 - 16.22 wt%), metadiorites have lower SiO_2 (60.91 wt%) and Al_2O_3 (14.04 wt%) contents. Mafic granulites have high levels of MgO (3.53 wt.%), CaO (3.18 wt.%), and Fe_2O_3 (12.68 wt.%). A comparison of the geochemical data for metadiorites and granitic gneisses from the Bogoin iron deposit with those for granitic gneisses from Mewengo reveals similarities between these rocks within the Nyong Complex. Metadiorites have TiO_2 concentrations of 0.49 wt%.

The TAS diagrams of magmatic rocks SiO_2 versus $Na_2O + K_2O$ according to [73] revealed that our samples originate from dioritic protoliths of intermediate composition, bearing a subalkaline signature (**Figure 18(a)**).

b) Trace elements

In the Bogoin Complex, a gradual increase in concentrations of large ion lithophile elements (LILE) such as Ba, Rb, Cs, K and Sr, as well as high field strength elements (HFSE) such as Nb, Ta, Zr and Hf, is observed from metadiorites to granitic gneisses.

c) Rare earth elements (REE)

The Metadiorite REE patterns exhibit mild to strong fractionation (La_{CN}/Yb_{CN} = 21.25), a minor enrichment of LREE (La_{CN}/Sm_{CN} = 4.96) versus HREE (Gd_{CN}/Yb_{CN} = 2.15), and considerable negative Eu anomalies (Eu/Eu* = 0.89). The chondrite-normalized REE patterns show a slightly fractionated pattern and very mild enrichment in LREE and HREE (**Figure 18(d)**). The primitive mantle- normalized multielement pattern is characterized by negative Nb, Ta, and Sm anomalies, small negative Ti anomalies, and enrichment of LILE over the HFSE (**Figure 18(e)**).

Overall, the trace element distribution patterns of the metadiorites are comparable to those of the granitic gneisses of the Mewengo (**Figure 18(d)** and **Figure 18(e)**).

3) Amphibolites

Figure 18(a) illustrates that amphibolites have subalkaline and tholeiitic basalts as protoliths. These host rocks have an iron-rich tholeiitic affinity (**Figure 19(b)** and **Figure 19(c)**).

a) Major elements

Samples are basaltic in composition (Mg# ≈ 0.60 - 0.69). SiO_2 (40.15 - 50.05 wt.%), Fe_2O_3 (13.84 - 14.78 wt.%), CaO (9.61 - 12.48 wt.%), Al_2O_3 (6.57 - 7.72 wt.%), and MgO (11.29 - 15.91 wt.%) concentrations are consistent with mafic rocks.

The total of alkalis ($Na_2O + K_2O$) ranges from 0.56 to 2.26 wt.%. All the studied samples display low contents of TiO_2 (≤1 wt%) and MnO (≤0.2 wt%). The high CaO content (9.61 - 12.48 wt%) indicates plagioclase accumulation in mafic host rocks.

Based on the CaO-MgO-FeOt triangular discrimination diagram, the samples showed an ortho-amphibolite signature, with the exception of sample BO13, which showed a para-amphibolite signature (**Figure 19(d)** and **Figure 19(e)**) similar to that described by Kwamou Wanang [79] within the Ntem series and by Topien [47] within the Central Africa Fold Belt.

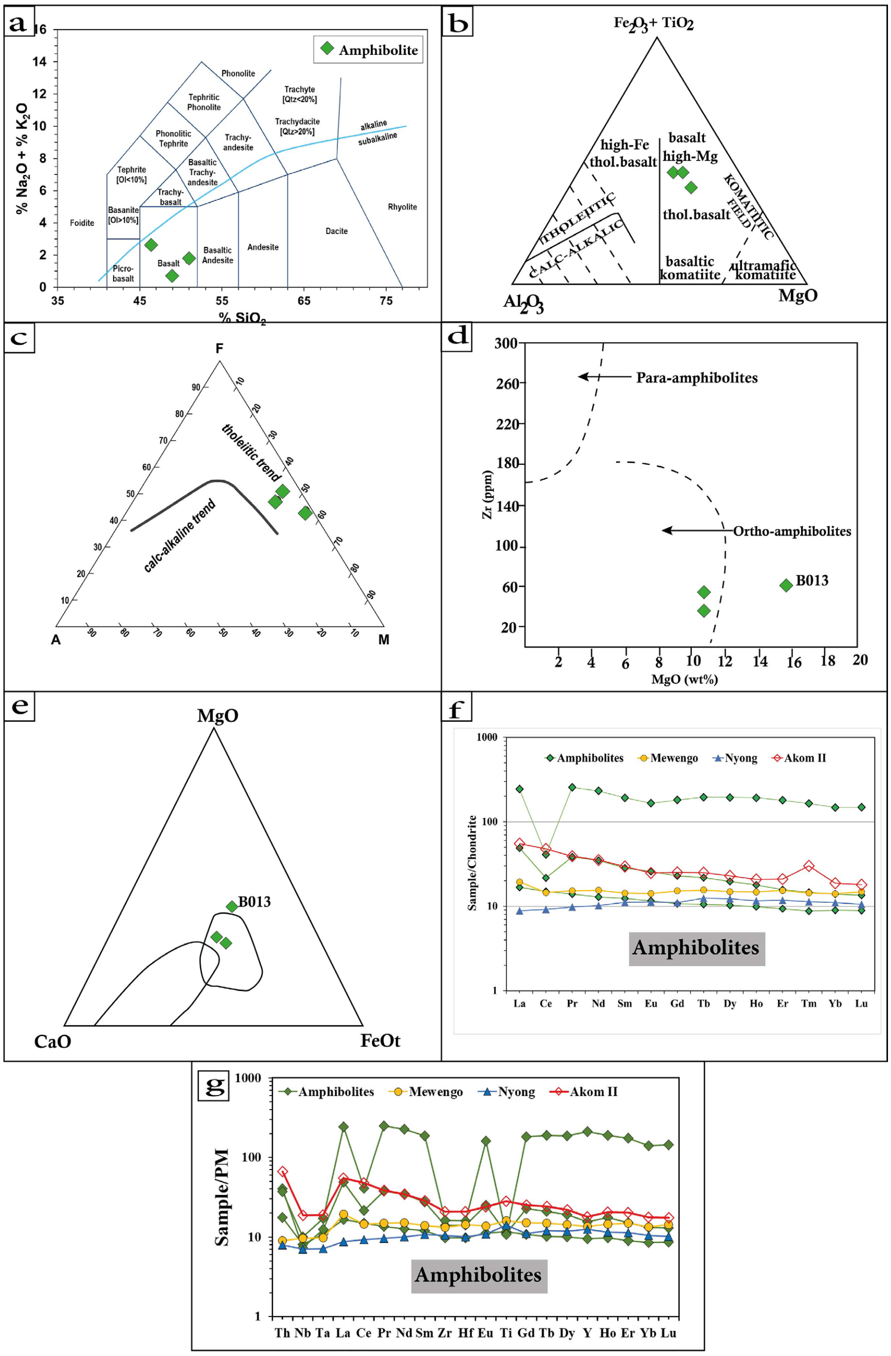

Figure 19. Magma characterization diagrams of mafic rocks: (a) Total alkali versus SiO_2 diagram for the classification of mafic-ultramafic metavolcanic rocks after [73]; (b) Al_2O_3-Fe_2O_3 + TiO_2-MgO ternary diagram [78]; (c) AFM plot showing the basaltic composition and the tholeiitic affinity of the Bogoin amphibolite's protolith; (d) Zr vs. MgO and (e) CaO MgO FeOt diagrams for amphibolites showing the ortho-amphibolite origin; (f) and (g) Chondrite-normalized [77] rare earth element (REE) patterns and primitive-mantle-normalized [76] multi-element plots of mafic metavolcanic rocks.

b) Trace elements and rare earth elements (REE)

HFSE concentration including Nb, Ta, Zr, Th, and U in amphibolite samples are lower than 10 ppm, except for Zr (37.9 - 62.50 ppm) and Y (14.9 - 330 ppm). Rb (0.24 - 79.3 ppm) and other large-ion lithophile elements (LILE: Rb, Ba, Sr, Ce, and Li) have extremely low concentrations, whereas Sr (6.5 - 127 ppm) and Ba (17.5 - 413 ppm) have slightly higher values. It has high Cr concentrations that vary from 533 to 1456 ppm, Cr indicating strong mafic to ultramafic rocks of a primitive mantle source or cumulate enrichment. Altogether, these geochemical features are typical of metavolcanic rocks in greenstone terranes formed in arc-related or back-arc settings.

Chondrite-normalized REE patterns (**Figure 19(f)**; [76]) show a slight enrichment in LREE $(La/Yb)_N$ = 1.65 - 1.87, except sample BO15, which shows a high enrichment in LREE $(La/Yb)_N$ = 3.52) compared to HREE $(Gd/Yb)_N$ = 1.20 - 1.63). Eu anomaly is positive (Eu/Eu* = 0.89) to negative (Eu/Eu* = 1.00 - 1.01). Low Ce anomaly is observed in the samples (Ce/Ce* = 0.17 - 0.97). The trace element patterns show LILE enrichment and HFSE such as Nb and Ta depletion (**Figure 19(g)**) similar to those of arc volcanic rocks. Rocks are enriched in transition metals such as V (155 - 219 ppm), Cu (37.4 - 115 ppm), Ni (257 - 436 ppm), and Co (30.7 - 71.5 ppm), reflecting their mantle origin (**Figure 19(f)** and **Figure 19(g)**).

4) Itabirite (Banded Iron Formation)

a) Major elements

Major elements data of the representative samples of the Bogoin iron prospect are reported in **Table 6**. The bulk chemical composition of the analyzed rock samples shows SiO_2 and Fe_2O_3t values ranging from 1.08 to 1.43 wt.% (average: 1.26 wt.%) and 97.29 to 97.90 wt.% (average: 97.57 wt.%), respectively, which suggests that SiO_2 and Fe_2O_3 are the dominant components. These two major oxides are the most important components in the Bogoin iron deposit, and they represent 98.83% of the bulk rock composition, while the other major elements represent 0.40%. All samples have significantly low Al_2O_3 (0.32 wt% - 0.48 wt%, with an average of 0.40 wt%) and below the detection limit with TiO_2 (<0.02 wt%) concentrations. Assuming that Al_2O_3 represents the detrital fraction of sedimentary rocks (*e.g.*, [80]), the presence of clay material in the iron formation, of which alumina is an index, indicates an initial clastic contribution in the basin of deposition. Thus, the lower contents of Al_2O_3 in the samples of the study area could suggest less detrital input to the depositional site.

The alkali contents are below the detection limit in all the samples with Na_2O (<0.02 wt%) and K_2O (<0.03 wt%). MgO (<0.03 wt%) and CaO (<0.03 wt%) are below the detection limit in all the samples. The absence of concentrations of both elements, particularly when combined with low volatile matter (LOI) content, indicates an absence or very low quantity of silicate minerals (chlorite and biotite), which is also confirmed by petrographic studies.

b) Trace elements and rare earth elements (REE)

The whole-rock trace and rare earth element (REE) concentrations of Bogoin

BIFs samples are presented in **Table 6**.

The transition metals Zn, Cr, Sr and V occur at low concentrations in the Bogoin itabirites (Zn: n.d.; Cr: 9.71 - 11.68 ppm; Sr: 2.30 - 4.72 ppm; V: 21.85 - 22.64 ppm; **Table 6**) markedly lower than in the associated amphibolites (Section 4.1.3.3).b). These transition metals are commonly used as indicators of direct volcanogenic hydrothermal input in chemical precipitates [81] [82]. Zr, Hf, Rb, Y, and Sr are commonly derived from the weathering of crustal felsic rocks, whereas Cr, Ni, Co, V and Sc have a mafic source [83] [84]. In contrast to the associated amphibolites, the Bogoin itabirites are not enriched in Cr, consistent with a negligible contribution of crustal mafic material to the BIFs. However, when compared to upper continental crust, extremely low concentrations are observed with incompatible elements such as Th (0.92 ppm), Hf (1.42 ppm), Sc (27.30 ppm), and Zr (51.50 ppm). This reflects a non-detrital origin for the silicates [85]. Detrital contribution is also excluded for the low concentration of HFSE (Th, Zr, Hf and Sc), which are normally enriched in evolved crust.

Yttrium shows a similar chemical behavior to REE, so it was inserted between Dy and Ho based on its ionic radius [86]-[88]. The REY (REE + Y) for all samples is normalized to the post-Archean Australian shale (PAAS, subscript SN, [87]), Upper Continental Crust (UCC, [89]; **Figure 20(a)**), and Chondrite (CI, subscript CN, [90]). The REY ratios of iron ores calculated as $(Pr/Yb)_{SN}$ = PrPAAS/YbPAAS, $(Tb/Yb)_{SN}$ = TbPAAS/YbPAAS, La/La* = LaPAAS/(3PrPAAS − 2NdPAAS), Ce/Ce* = CePAAS/(2PrPAAS − NdPAAS) [91], Eu/Eu* = EuPAAS /(0.67SmPAAS + 0.33TbPAAS) [86], Y/Y* = 2YPAAS/(DyPAAS + HoPAAS).

When compared to PAAS, the iron-bearing formations at Bogoin contain low REE concentrations (mean ΣREE = 37.28 ppm) with $(Pr/Yb)_{SN}$ and $(Tb/Yb)_{SN}$ values of 0.20 - 0.47 and 1.01 - 1.31, respectively, indicating light REE (LREE) depletion and relative heavy REE (HREE) enrichment for all samples. The PAAS-normalized diagrams (**Figure 20(b)**) exhibit a positive but weak Eu anomaly $(Eu/Eu^*)_{SN}$ = 1.53 - 1.61 with an average of 1.6, characteristic of late Paleoproterozoic iron formations [92]. The HREE patterns are flat and parallel. These diagrams show positive La, Gd, Y, Eu, and Ce anomalies and chondritic to superchondritic Y/Ho ratios (La/La^*_{SN} = 1.4 - 2.0, average: 1.7; Gd/Gd^*_{SN} = 1.25 - 1.38, average: 1.30; Y/Y^*_{SN} = 0.97 - 1.26, average: 1.11; Ce/Ce^*_{SN} = 1.74 - 2.70, average: 2.22; and Y/Ho = 26.96 - 30.80, average: 27.48), which suggests the influence of both ambient seawater and, especially, a hydrothermal fluid. Lanthanum enrichment, together with the well-known Ce enrichment, has been identified in modern seawaters. Bau and Dulski [86] have proposed the use of the Ce/Ce*(SN) vs. Pr/Pr*(SN) binary diagram to discriminate 'true' Ce anomalies (**Figure 20(c)**). The Ce/Ce* vs Pr/Pr* diagram of Bogoin BIF (**Figure 20(c)**) shows that the majority of samples have true positive Ce anomaly. The true positive cerium anomaly is a distinctive feature between Archaean to early Paleoproterozoic BIF and late Paleoproterozoic BIF [92]. On the chondrite-normalized REE diagram (**Figure 20(d)**), all of the samples show obviously positive Ce anomalies and an enrichment in

LREE ($(La/Yb)_{CN}$ = 0.93 - 4.62) and depletion in HREE ($(Tb/Yb)_{CN}$ = 0.13 - 0.17). Weak positive Eu anomalies are observed, and the Eu/Eu* values vary between 1.59 and 2.36 (**Table 6**). It has been suggested (*e.g.*, [86] [93]) that the size of the positive Eu anomaly of BIF decreases with age, with the largest Eu anomalies in Eoarchean BIFs and the smallest in Mesoproterozoic BIFs. The loss of positive Eu anomaly on the chondrite- normalized patterns is thus indicative of a Paleoproterozoic age of the studied BIFs. Additionally, the chondrite-normalized REE patterns differ from the HREE-enriched trends (Sm_{CN}/Yb_{CN} = 0.92 < 1), which characterized most Archaean BIF (*e.g.*, [94]).

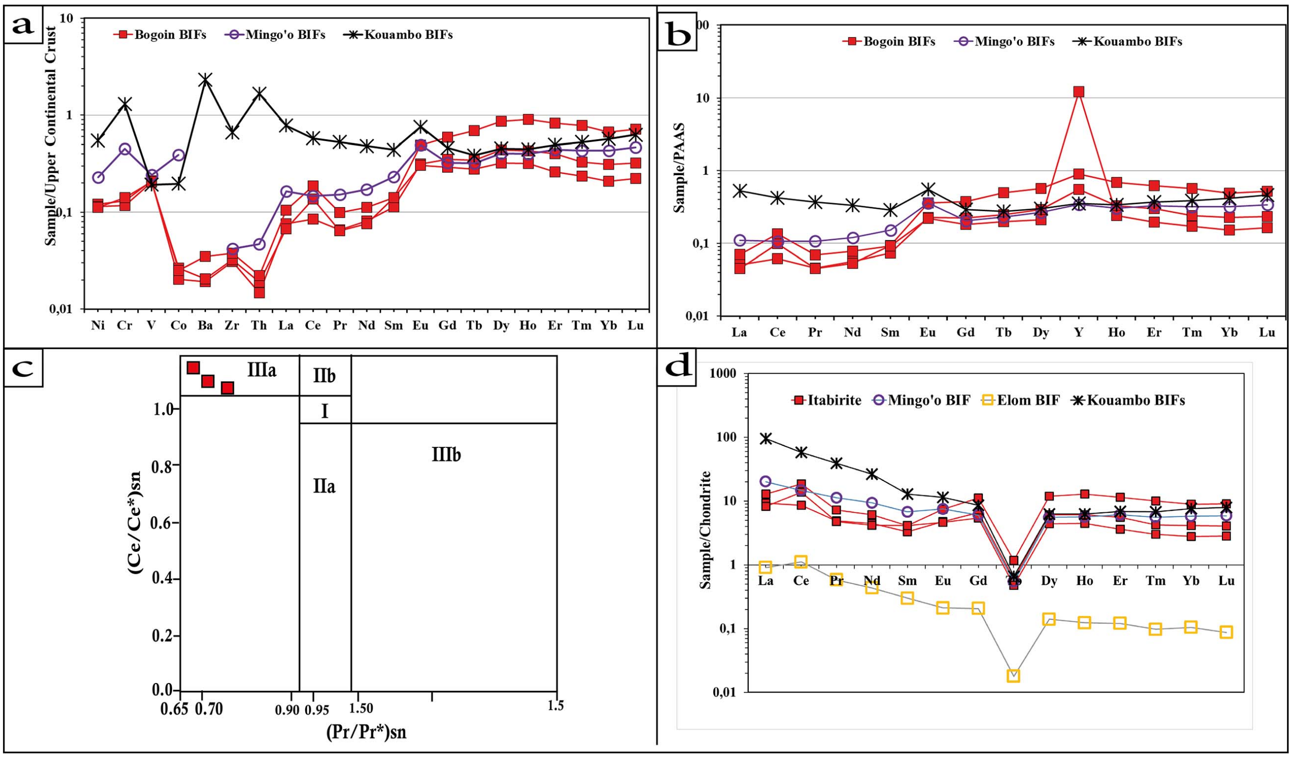

Figure 20. (a) Upper Continental Crust (UCC, [89]); (b) The REY (REE + Y) for all samples are normalized to the post-Archean Australian shale (PAAS, subscript SN, [95]); (c) (Ce/Ce*)SN vs. (Pr/Pr*)SN diagram (after [86]) for the Bogoin BIF. Field I: neither Ce nor La anomaly; field IIa: positive La anomaly, no Ce anomaly; field IIb: negative La anomaly, no Ce anomaly; field IIIa: positive Ce anomaly; field IIIb: negative Ce anomaly; (d) Chondrite-normalized REE spider diagram for the Itabirite from the Bogoin area; normalizing values are from [90].

4.2. Discussion

4.2.1. Petrogenesis of the Bogoin Complex

1) Gneiss

The Bogoin gneiss and metadiorite yield a low loss of ignition (LOI < 1 wt%, **Table 6**) and are characterized by a lack of Ce anomalies (Ce/Ce* = 1.08 - 1.09, **Table 6**), which indicate that the studied rocks were not significantly overprinted by late alteration and their elements can mostly reflect their primary geochemical features as described by Polat and Hofmann [96].

The Y versus Sr/Y diagram can be used to evaluate residual mineralogy and depth of melting of TTGs. Gneiss samples plot along the trajectory of model curve I, clearly indicating an Archaean mafic crustal source (**Figure 21(a)**). Furthermore, they show moderate Sr (131 - 489 ppm), Ba (598 - 1309 ppm), variable Y (3.87 - 7.82 ppm), and Sr/Y (16.79 - 126.56) ratios along with slight negative to positive Eu anomalies (Eu/Eu* = 0.46 - 1.15) suggesting that plagioclase may have existed as a residual or fractionated phase. It show slight enriched LREE relative to HREE patterns with moderate $(La/Yb)_N$ = 30.01 - 89.56) ratios and Yb_N values (1.96 - 4.53), which are consistent with garnet in the residue [97]. Generally, there are two common tectonic settings which can produce TTG magma [98] [99]: 1) melting of subducted-related crust and 2) partial melting of hydrated metabasaltic rocks (amphibolites) at depth within the stability field of garnet. Recently, Liou and Guo [100], and Laurent *et al.*, [101] have proposed that TTGs may have been generated through fractional crystallization processes.

The subduction-related TTG magmas generally depict high Mg#, Cr, and Ni contents due to interactions between the TTG melts and the slab-derived mantle wedge [102]. However, the granitic gneisses of the Bogoin display low Mg# (30 - 38), Cr (4.2 - 9.5 ppm), and Ni (3.4 - 4.7 ppm) contents suggesting that their magmatic precursors were not contaminated by mantle materials. This could confirm field observations showing the absence of mafic enclaves within granitic gneiss. In the Ce/Sm versus Ce (ppm) diagram, the variations of Bogoin TTG rocks are dominantly controlled by the fractional crystallization processes (**Figure 21(b)**).

In addition, Moyen [98] proposes three types of TTG suites: the high-pressure (P > 20 Kbar), medium-pressure (P = 10 - 20 Kbar), and low-pressure (P < 10 Kbar) TTG rocks. The high-pressure TTG rocks commonly show low HREE, Nb, and Ta and high Sr concentrations and contain garnet and rutile as major residual mineral phases, while the low-pressure TTG rocks exhibit high HREE, Nb, and Ta, and low Sr concentrations, with amphibole, plagioclase, and minor garnet as major residual minerals [98]. In comparison to the average Sr content of continental crust (Sr = 348 ppm; [103]), all of the gneiss samples display low Sr contents (131 - 489 ppm, average Sr = 310 ppm) and negative to positive Eu anomalies. However, plagioclase fractionation can decrease Sr concentrations in TTG rocks. Hence, the overall low Sr contents in these samples may indicate that, the Sr was controlled by plagioclase-rich source residual phase rather than plagioclase fractionation.

Moreover, rutile and amphibole are index minerals that usually contain abundant Nb and Ta and are very important for understanding the residual minerals in the source region and possible tectonic setting. Due to high partition coefficient for Ta relative to Nb in rutile, experimental results showed that, if minor rutile appears in the residual source, the Nb/Ta ratios in the coexisting partial melts will increase [104], while Nb is more compatible than Ta in amphibole and small amount of amphibole as residual mineral could lead to lower Nb/Ta ratios [104]. In the Bogoin area, the granitic gneisses display lower to high Nb/Ta ratios (7.61 - 16.61), showing the compositional source of amphibole and rutile minerals. This is confirmed by the Nb/Ta vs. Zr/Sm diagram, where all the samples plot between the field of amphibole and rutile (**Figure 21(c)**), indicating that an amphibole and a rutile-rich residual mineralogy were necessary during TTG generation. The relatively low HREE, Yb, and Y (**Table 6**) are compatible with garnet [105] and indicate that minor garnet could be a residual. The combination of all the geochemical features shows that the Bogoin granitic gneisses protoliths were probably derived from partial melting of juvenile crustal materials under a relatively low-pressure environment, which were equilibrated with a certain amount of amphibole-rutile and plagioclase and minor garnet in the residue.

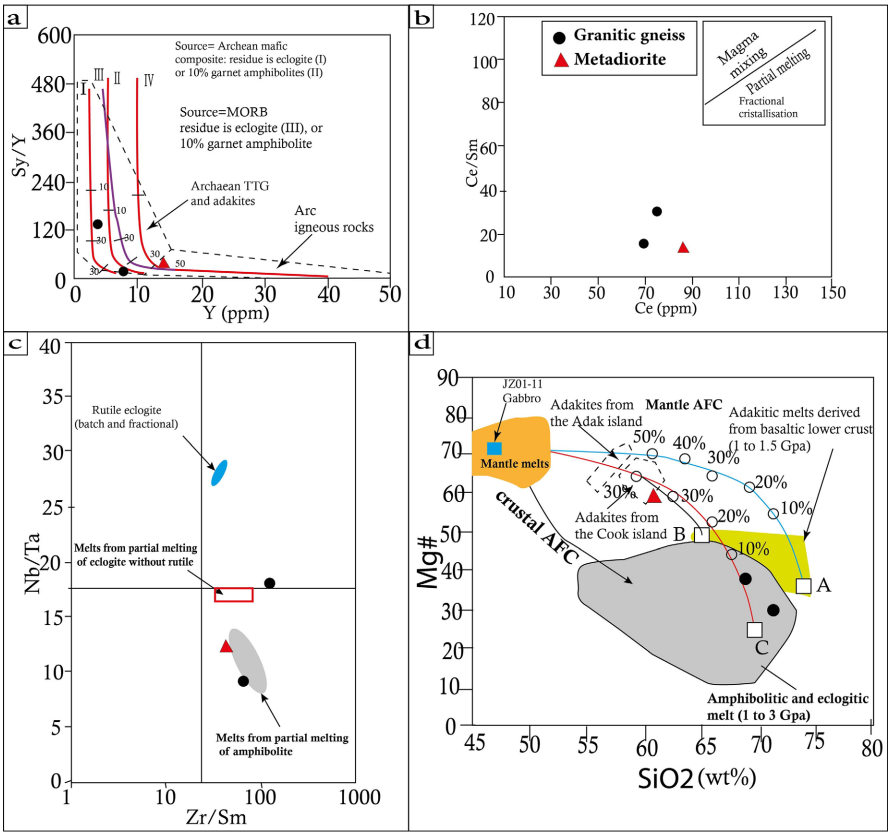

Figure 21. (a) Sr/Y versus Y diagram [106]; (b) Ce/Sm versus Ce diagram [107]; (c) Nb/Ta vs. Zr/Sm diagram (from [108]); (d) SiO_2 vs. Mg# diagram (after [109]). Field for adakitic melts derived from basaltic lower crust under conditions of 1 - 1.5 Gpa and 800˚C - 900˚C is after [110].

2) Metadiorite

The metadiorite have high Sr (451 ppm) and Ba (1625 ppm) contents, high ratios of Sr/Y (31.94), and weakly negative to no Eu anomalies (Eu/Eu* = 0.89), typical of adakites (**Table 6**; **Figure 21(d)**, [106]). The sample plot in the adakite field on the Sr/Y versus Y, presents values in $(La/Yb)_N$ = 21.12 and Yb_N = 8.30 (**Figure 21(a)**) further supports this inference. Geochemically, the metadiorite has relatively high SiO_2 content (60.98 wt%), low MgO content (4.94 wt%), indicating a predominantly crustal origin.

The mantle magma generated a large number of mafic rocks during fractional crystallization to form granitoid. However, the Bogoin area lacks contemporaneous basalt, and most akakites derived from the mantle are high-Mg andesites with Mg# >60. Furthermore, the metadiorites have SiO_2 contents of >60 wt%, and MgO contents of <5 wt%, which proves that they did not originate from the partial melting of a wedge mantle metasomatised by the previous adakitic melts [111]. Additionally, the high-SiO_2 adakitic melts could be obtained by the partial melting of the subducted oceanic crust, which displays relatively low K_2O content (3.44 wt%) and low K_2O/Na_2O ratios (1.05) [106] [111].

The metadiorite displays higher values of Mg# (60) and higher Cr (186 ppm) and Ni (88.4 ppm) contents than those produced entirely by the partial melting of the crustal materials (**Figure 21(c)**). This also reflects the contribution of the melts that were derived from the mantle. This view is also consistent with the presence of mafic enclaves within metadiorites.

The metadiorite could be produced by a mix of 30% mafic melt and 80% - 90% felsic melt according to the calculation of a mixing line (**Figure 21(d)**). Thus, it was formed by the partial melting of the normal lower continental crust, which then mixed with the high-Mg# melts, derived from an enriched lithospheric mantle.

3) Amphibolite

Magma compositions are generally influenced by the nature of the mantle source, processes such as partial melting, fractional crystallization, crustal contamination, and post-magmatic alteration [112]. These processes are examined here using major and trace element data.

The LOI values of the amphibolites range from 1.13 to 8.44 wt% (**Table 6**), and their total alkali content ($Na_2O + K_2O = 0.56$ - 2.26 wt%) is also variable; both are higher and more variable than expected for strictly unaltered basaltic rocks, indicating that these samples record variable degrees of low-grade metamorphic and/or hydrothermal alteration rather than being entirely fresh. Because major elements and alkalis (Na_2O, K_2O, CaO) are susceptible to mobility during such alteration, the petrogenetic and tectonic interpretations below rely primarily on elements considered immobile under these conditions (*e.g.*, Ti, Zr, Nb, Y, Th, REE) and on their ratios. Major-element-based discrimination diagrams (*e.g.*, the TAS and AFM diagrams, **Figure 19(a)**, **Figure 19(c)**) are retained for a first-order classification but are interpreted with caution and cross-checked against the immobile-element diagrams presented below (*e.g.*, the Zr/Ti vs. Nb/Y diagram, **Figure 22(a)**).

The positions of the studied amphibolites in the Zr vs. MgO diagram for ortho and para amphibolites indicate that they are orthoderived, with an igneous source for the parental rocks (**Figure 19(d)**). The same results are described in the Congo craton from Akom II [113] and Mewongo [79] areas. The geochemical classification of extrusive rocks diagram using Nb/Y vs. Zr/Ti adapted from [114] shows the volcanic origin of those rocks (**Figure 22(a)**), where the main samples plot in the alkali-basalt field, except one sample falling within the basalts field, probably due to some contamination of the magma source.

Alkali basalts are characterized by highest Na_2O and K_2O content than the basic basalts, and low SiO_2 contents (40.15 - 50.05 wt%) [115], they are located behind the arc. However, they are not likely to form at depths shallower than 50 - 60 km [116] [117]. This hypothesis is confirmed by the high values in Ni (257 - 436 ppm) and Co (30.7 - 71.5 ppm), which are evidence of a (deep) mantle source [118]. Amphibole and rutile as residual minerals can be used to constrain this source.

Indeed, rutile and amphibole are index minerals that usually contain abundant Nb and Ta. In the rutile mineral composition, Ta is relative to Nb, and the experimental results showed that, if minor rutile appears in the residual source, the Nb/Ta ratios in the coexisting partial melts will increase [104].

On the other hand, Nb is more compatible than Ta in amphibole, and a small amount of amphibole as a residual mineral could lead to lower Nb/Ta ratios [104].

All samples of amphibolites display lower Nb/Ta ratios (10.22 - 13.12), indicating the compositional source of amphibole minerals.

Certain chemical parameters can be used to evaluate the level of contamination. For example, the major element TiO_2 is a well-founded discrimination between arc and spreading ridge basalts [119] [120]. He is relatively immobile during alteration. Low TiO_2 content suggests that the protolith is in an arc system [120]. But the TiO_2 content of the study amphibolites is low to medium (0.64 - 0.68 wt%), which needs others explanations to give a conclusion. In the same vein, ratios of some trace elements can constrain the crustal contamination in basaltic rocks. Those that are affected by crustal contamination exhibit La/Ta = 26.13 - 241.30 and La/Nb = 1.99 - 23.41 [121].

The studied amphibolites exhibit low to moderate La/Ta and La/Nb ratios, ranging from 26.13 to 241.30 and from 1.99 to 23.41, respectively, which confirms the role of contamination during magmatic evolution. In addition, incompatible trace elements such as Ta, Yb and Th are considered to determine crustal contamination. The crustal contamination affects Th more than Ta and Yb. The contamination shows high Th/Yb values [122]. The studied amphibolites show low values of Th/Yb (0.05 - 0.52), and this suggests no or minimal crustal contamination for Bogoin amphibolites parent rocks.

Bogoin amphibolite shows obvious depletion in Nb and Ta, which are generally regarded as basaltic rocks derived from the partial melting of mantle wedges in subduction zones with an influence of a continental crust component.

The fractionation occurs during the formation of the protoliths of those amphibolites. The REE patterns are marked by TiO_2, Nb, Ta and Eu anomalies (**Figure 19(f)**). The TiO_2 anomaly in multi-element diagram suggests a Ti-oxides fractionation.

The fractionation of plagioclase is confirmed by the presence of Eu anomaly (Eu/Eu*: 0.89 - 1.05) in the chondrite-normalized REE diagrams of Bogoin amphibolites, which indicate a plagioclase-depleted crustal source or fractionation during magmatic differentiation.

The $K_2O + Na_2O$ vs. $K_2O/(K_2O + Na_2O)$ diagram [123], displays an assimilation and fractional crystallization trend (**Figure 22(b)**). We can see through this plot the role of the fractionation in the rock's emplacement. The combination between low MgO value and moderate to high Fe_2O_3 contents also suggests fractional crystallization, but the fractional crystallization of Mg-rich minerals (*i.e.*, pyroxene), which is typical of tholeiitic magmas [124]. In the same way, the parental basaltic magma from which the Bogoin amphibolites were derived is inferred to belong to the tholeiitic series, as shown by the SiO_2 vs. FeOt/MgO diagram (**Figure 22(c)**) of Miyashiro, [125], like in the Nyong area, southern domain, Cameroon [79]. All the samples of Bogoin amphibolites plot in the tholeiitic series area and display a tholeiitic trend as demonstrated in the Mg# vs. SiO_2/Al_2O_3 diagram, showing the primitive basalts field and differentiation [124] and mineral fractionation trends (**Figure 22(d)**) adapted after [126].

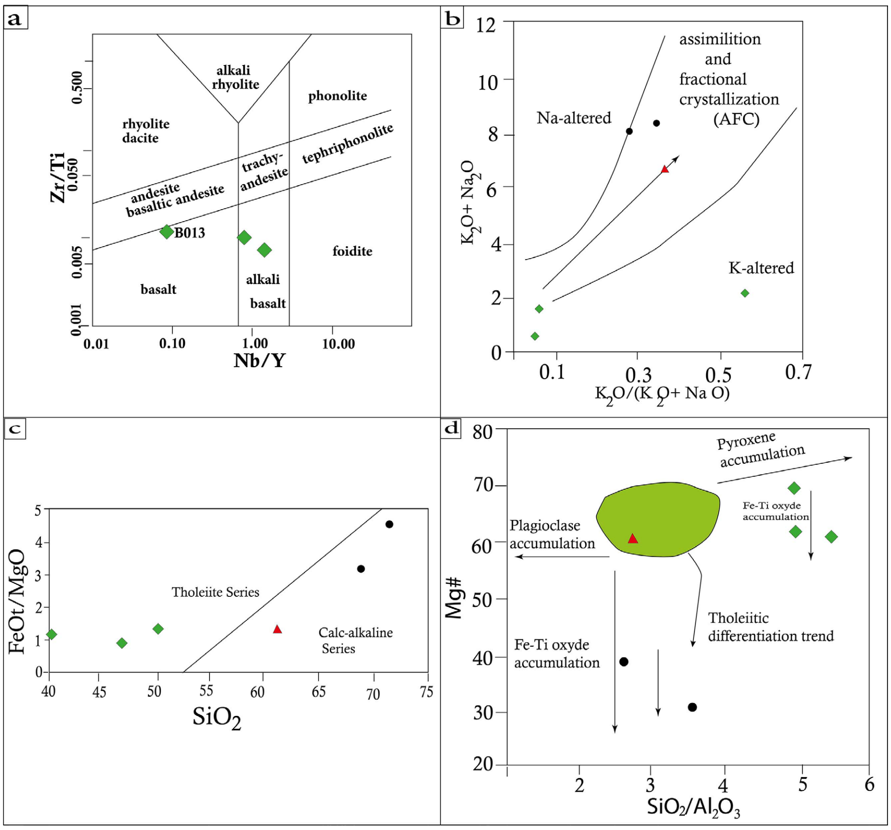

Figure 22. (a) Zr/Ti vs. Nb/Y Plot of amphibolites protolites [114]; (b) $K_2O + Na_2O$ vs. $K_2O/(K_2O + Na_2O)$ diagram of igneous rocks (adapted from [123]; (c) FeOt/MgO vs. SiO_2 Plot of [127]; (d) Mg# vs. SiO_2/Al2O_3 diagram showing the primitive basalts field [128] and differentiation and mineral fractionation trends (after [126]).

4) Itabirite

a) Detrital input

Even though BIFs are typically thought of as pure chemical sediments, the deposition of terrigenous materials of felsic or mafic origin has frequently affected their composition (*e.g.*, [82] [129]-[131]).

The high concentrations of Fe_2O_3 (average: 97.57 wt%) and low concentrations of SiO_2 (average: 1.26 wt%) in the Bogoin itabirites, respectively (**Table 6**), suggest that these are almost pure chemical precipitates.

The low Al_2O_3 (mean: 0.40 wt%) and TiO_2 (Below the detection limit) contents of the Bogoin indicate trivial incorporation of a terrigenous component. It is noteworthy that Al_2O_3 does not have a significant relationship with Zr for the studied BIFs (**Figure 23(a)**), indicating near absence of detrital input during chemical precipitation of the Bogoin BIFs.

Moreover, the low ΣREY content (mean: 37.28 ppm; **Table 6**) as well as no to weak correlation between ΣREY and Zr (**Figure 23(b)**) suggest that the contribution of detrital components to their composition was insignificant.

Lower admixture of any contaminant in chemical sediments precipitated in the seawater would lower the superchondritic Y/Ho ratio to similar to that of seawater (>44), and co-variation between Y/Ho and Zr would be seen because the crustal material (such as felsic and basaltic rocks) had a constant Y/Ho ratio of 26 [132]. The itabirite have Y/Ho ratios ranging from 32.39 to 35.54 (**Table 6**), which are above the chondritic ratios (28.75) of McDonough and Sun [75]. There is striking evidence against contamination of the Bogoin BIFs during their precipitation as shown by the weak correlation (r = 0.85, respectively) between Zr and Y/Ho (**Figure 23(c)**).

This suggests that the decrease in Y/Ho ratios in the original BIFs is not related to crustal contamination. In summary, we suggest that the Bogoin BIFs were formed by chemical precipitation with insignificant admixture of detrital components, which is similar for most of the Ntem Complex BIFs (*e.g.*, [130] [131] [133]) and other BIFs worldwide (*e.g.*, [81] [91] [134]).

b) Hydrothermal versus seawater input

Numerous writers have shown that diagenesis and metamorphism do not substantially alter the basic Rare Earth Element + Yttrium (REY) content of BIFs (*e.g.*, [86] [91] [133] [135]). Thus, the REE+Y signatures of BIFs are strong pieces of evidence for constraining their origin (*e.g.*, [92]).

Shale-normalized REE+Y patterns of most BIFs worldwide display seawater signatures, including 1) positive La, Gd, and Y anomalies, 2) high Y/Ho ratios (>40), and 3) LREE depletion (*e.g.*, [86] [91] [136]). The REE+Y patterns of the Bogoin samples are depleted in LREEs and show positive La, Gd, and Y anomalies, whereas their average Y/Ho ratios are 32.39 and 35.54, respectively (**Figure 20(b)**; **Table 6**). Some authors (*e.g.*, [86] [137]) have proposed that the Y/Ho ratios of hydrothermal fluids at a vent site display a chondritic value of ~28, while seawater has a superchondritic Y/Ho ratio (~44).

Therefore, the Bogoin BIFs' near-chondritic average Y/Ho ratio was most likely inherited from hydrothermal solutions. On the other hand, it is commonly accepted that positive Eu anomalies in BIFs reflect the influence of hydrothermal fluids on seawater composition (*e.g.*, [86] [91] [92]). Hydrothermal alteration of oceanic crust is caused by high-temperature (high-T, >300˚C) or low-temperature (low-T, <200˚C) hydrothermal fluids. High-T hydrothermal solutions display a large positive Eu anomaly (Eu/Eu* > 1.52), similar to that of Archaean and early Proterozoic BIFs in which Fe and Si were mainly derived from high-T hydrothermal fluids [91] [93] [139]. The decrease in Eu anomaly with the decreasing depositional age of BIFs is attributed to the contribution of low-T hydrothermal solutions to the REE source [94] [140]. The PAAS-normalized REE+Y patterns of latest Proterozoic and Neoproterozoic BIFs worldwide exhibit weak positive to no Eu anomalies.

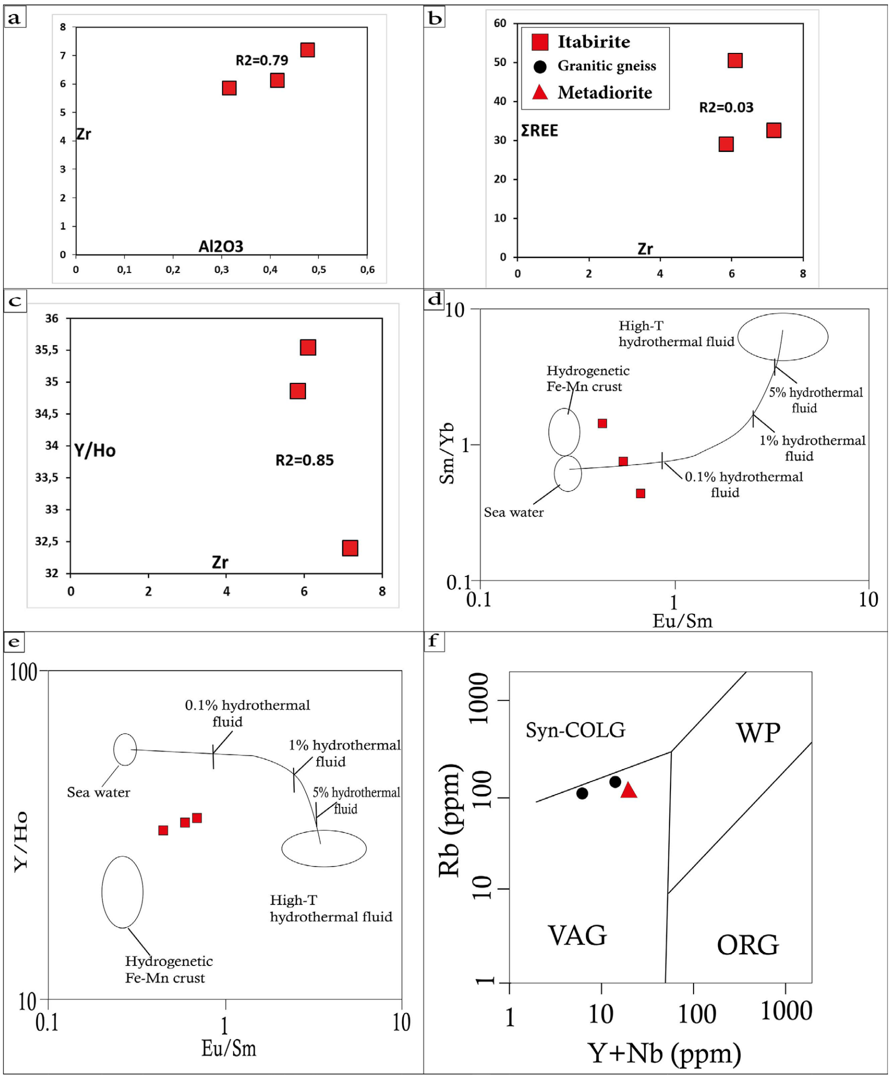

Figure 23. (a) (b) and (c) Harker variation diagrams for the Bogoin BIFs. (a) Zr versus Al_2O_3; (b) ΣREE versus Zr and (c) Y/Ho versus Zr; (d and e) Two-component conservation mixing lines (after Alexander *et al.*, 2008) of (d) Sm/Yb versus Eu/Sm and (e) Y/Ho versus Eu/Sm ratios for the Bogoin BIFs; (f) Tectonic discriminant diagram of studied sample, Rb versus Y + Nb [138].

The PAAS-normalized REE + Y patterns of the Bogoin BIFs exhibit positive Eu anomalies with a mean $(Eu/Eu^*)_{SN}$ of 1.56, respectively (**Figure 18(b)**; **Table 6**).

However, the average Eu anomaly of the Bogoin BIFs is 1.56, which is comparable to that of the early Proterozoic Hamersley BIFs (Eu/Eu^*_{SN} = 1.52, [93]. This result is consistent with the contribution of low-T hydrothermal fluids during the deposition of the Bogoin BIFs formed at c. 2500 Ma during early Paleoproterozoic time (*e.g.*, [86] [91]).

The REE + Y distribution patterns of the Bogoin BIFs show the characteristics of both low-T hydrothermal fluids (weak positive Eu anomaly) and seawater (LREE depletion relative to HREEs, positive Ce anomaly) (**Figure 20(b)**). This indicates that Fe and Si in the Bogoin BIFs were probably derived from the mixing of low-T hydrothermal solutions and seawater. Derry & Jacobsen [93] proposed that Paleoproterozoic surface seawater and high-T hydrothermal fluids have Y/Ho ratios of c. 65 and 28, respectively. The mean Y/Ho ratio of the detritus-free oxide facies BIFs is 34.26. This value suggests that the Bogoin BIFs would be precipitated from solutions composed of a ~30% seawater component and 70 % hydrothermal component. This result is further corroborated by the conservative two-component mixing models of Alexander *et al.* [141] (**Figure 23(d)** and **Figure 23(e)**). In both diagrams, it appears that a small seawater component and a significant low-T hydrothermal component have contributed to the precipitation of the studied BIFs, similar to those of the Ntem Complex BIFs [130] [133] [142]-[144]. From the above results, we propose that the Bibole BIFs were formed by precipitation from low-T hydrothermal fluids and seawater.

The average concentration of REE (ΣREE = 37.28 ppm) is comparable to other oxide-facies BIFs from the Archean to the Proterozoic around the world; the REE depletion of the Bogoin BIFs is consistent with REE data from Archean iron formations elsewhere [144]-[146]. Similar to REE profiles from other Archean BIFs [143] [147] [148], PASS-normalized REE profiles from the Bogoin area show slightly positive Eu anomalies (Eu/Eu^* = 1.56) relative to HREE (Tb_{SN}/Yb_{SN} = 1.14) with positive Ce anomalies (Ce/Ce^* = 0.96). Archean, early (>2.4 Ga) and late (<2.0 Ga) Paleoproterozoic banded iron formations are characterized by negative Ce anomalies [143] [146]. Due to their low positive Eu anomalies, which are comparable to those of late Paleoproterozoic BIFs, we consequently suggest that the Bogoin BIFs were most likely deposited between the early and late Paleoproterozoic [146]. Moreover, Fryer [147] proposed that Archean BIFs have Eu/Sm ratios ranging between 0.40 and 1.22, while Proterozoic BIFs range between 0.24 and 0.40. The Eu/Sm ratio of the Bogoin BIFs, which include Archean BIFs, ranges between 0.42 and 0.68.

4.2.2. Geodynamic and Tectonic Framework

No new geochronological data were generated in this study. The temporal framework adopted here for the Bogoin complex therefore combines ages inherited from previous regional studies, the 2.08 Ga U-Pb zircon age of the Yangana, type granite [31], the c. 2.3 Ga Pb-Pb/Sm-Nd isochron age proposed for the upper Bogoin amphibolites, [20] [34], and the c. 2.15 Ga post-tectonic Mbolene granite, with depositional-age constraints inferred in this study from the Eu and Ce anomaly systematics of the Bogoin BIFs (Section 4.1.3.4).b), which point to a Paleoproterozoic rather than a Neoarchean depositional age. Accordingly, the subduction-collision event responsible for the deformation and metamorphism of the Bogoin complex is attributed throughout this paper to the Paleoproterozoic Eburnean-Trans-Amazonian orogeny, consistent with the correlative event described in the Nyong Complex of Cameroon.

The geodynamic and tectonic framework of granitic gneisses and metadiorite is indicated by the tectonic discrimination diagrams Rb vs. Y + Nb, Nb versus Y + Nb, and Ta versus Yb (**Figure 23(f)**, **Figures 24(a)-(c)**) and the Hf-Rb/30-Ta*3 ternary plot proposed by Harris *et al.*, [149]. The granitic gneiss and metadiorite samples from the Bogoin area are comparable to those of the syn-collisional to post-orogenic mantle-fractionated granites of Batchelor and Bowden [150] (**Figure 23(f)**, **Figure 24(a)**, **Figure 24(b)**). These parameters indicate that the composition of the granitic gneisses and metadiorite samples from the Bogoin area is similar to the orthogneiss of the syn-collisional to post-orogenic in the northern border of the Congo craton in Cameroon, described by Kamguia Kamani *et al.*, [151]. The ternary diagram Hf-Rb/30-Ta_3, proposed by Harris *et al.* [149], displays most of the granitic gneiss and metadiorite samples of the Bogoin area plots in the volcanic arc field (**Figure 24(c)**).

Jung *et al.*, [152] developed a binary diagram based on REE to determine the facies (garnet or spinel) and, consequently, the depth of the magma source. All samples of amphibolite in the Bogoin area show no residual garnet and predominantly show ca. 4% partial melting of an amphibole-spinel-peridotite source in the Dy/Yb versus La/Yb plot (**Figure 24(d)**; [152]). Rooney's work [153] shows that sources containing garnet have a ratio $(Gd/Yb)_{CN} > 2$ or $(Tb/Yb)_{CN} > 1.8$. The average $(Gd/Yb)_{CN}$ ratio of the studied amphibolite rocks is $(Gd/Yb)_{CN} = 1.36$ and $(Tb/Yb)_{CN} = 1.36$, respectively, suggesting that garnet was not involved in their source.

We, therefore, propose that the metasomatized spinel peridotite source, which has undergone varying degrees of crystal fractionation and crustal contamination, served as the principal magma source for the Bogoin Complex metabasite rocks. Ce, an incompatible element, is significantly impacted by even minor changes in the source mineralogy (such as garnet or spinel). At the same time, Yb is well compatible with garnet but not with clinopyroxene or spinel. As a result, their Ce/Yb ratios are almost the same as those of the mantle, and as a result, they almost form a horizontal trend line with the primitive mantle. In contrast, partial melts from a garnet-lherzolite source have Ce/Yb values that are significantly higher than those of the mantle, and as a result, they exhibit an upper curve trend [154]. **Figure 24(e)** shows that samples of all amphibolite rocks from the Bogoin Complex plot parallel to the horizontal trend line for spinel-lherzolite.

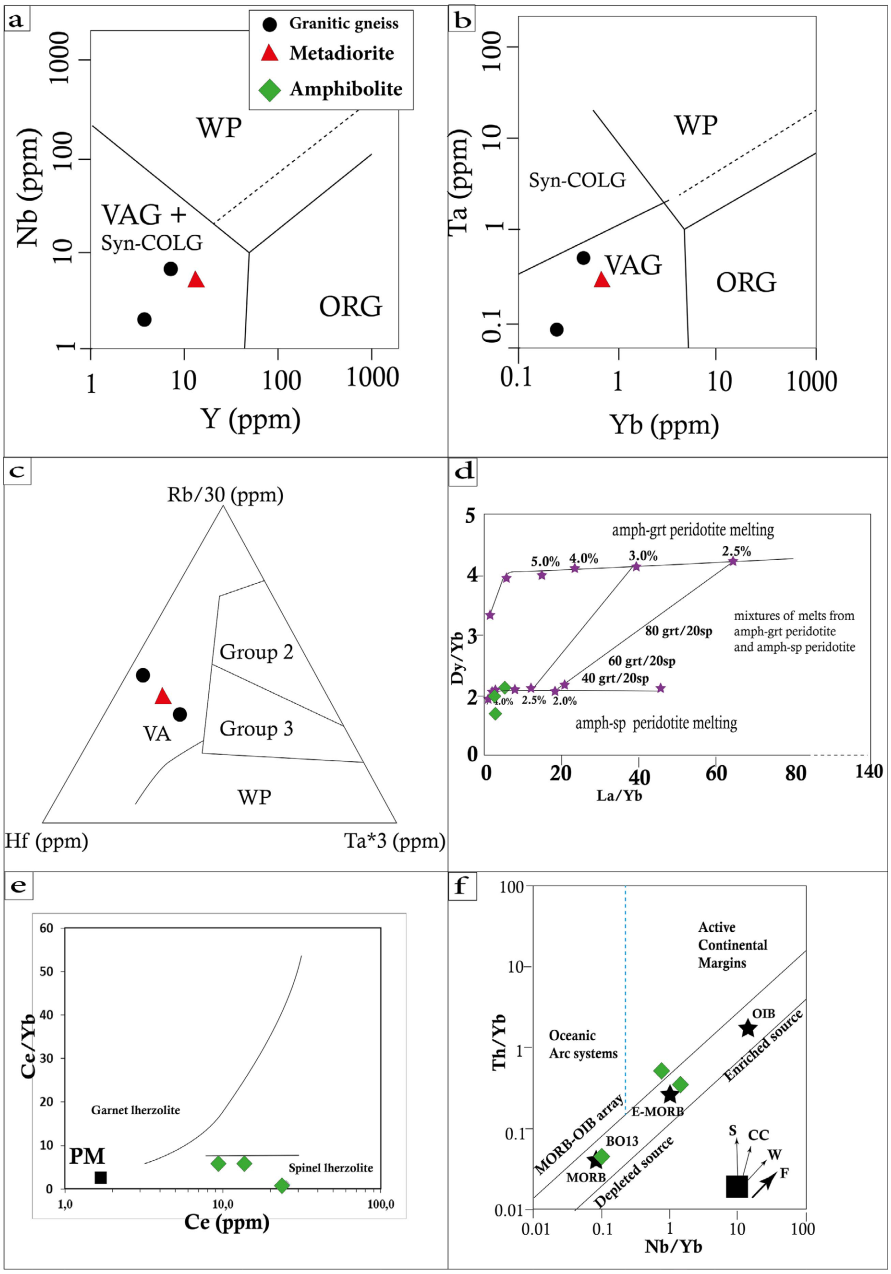

Figure 24. (a) (b) Tectonic discriminant diagrams of studied sample, (a) Nb versus Y + Nb and (b) Ta versus Yb [138]; (c) The Hf-Rb/30-Tax*3 ternary plot proposed by [149]; (d) Ce/Sm versus Ce diagram [107]; (e) Ce versus Ce/Yb plot (after [154]). PM: primitive mantle [76]; (f) Nb/Yb versus Th/Yb plot of [155]. Trends of the arrow: S: subduction component; CC: crustal contamination; W: within-plate variation; F: Fractionation.

The Th/Yb versus Nb/Yb diagram (**Figure 24(f)**; after [155]) demonstrates the affinity of the amphibolite samples with subduction zone arcs, except the BO13 sample, which falls within the oceanic arc systems. The Nb/Th versus Nb/Yb plot diagram for the amphibolites of the Bogoin area (**Figure 25(a)**; after [156]) reveals the influence of slab-derived fluids over slab-derived melt in the mafic rocks of the Bogoin area. When Nb/Th fluctuation is shown against Nb/Yb variation in

Figure 25(b) (with the OPB, AVR, and TTG compositional fields after [156]), the significance of slab-derived fluids in enriching the mantle sources becomes more obvious [156]. The minimal variance in Nb/Th vs Nb/Yb indicates that slab-derived fluids rather than slabderived melt were more important in the crystallization of the metamorphosed host rocks of the Bogoin Complex rocks. All samples of granitic gneiss and metadiorite are located in the tonalite-TTG field, while samples of amphibolite are located close to the arc volcanic rock (AVR) field (Figure 25(b)) in the Nb/Th versus $(La/Sm)_{PM}$ diagrams.

The samples were also plotted in a variety of tectonic discriminating diagrams, such as Shervais [157] Ti/1000 versus V, in which all samples amphibolite are plotted in the MORB and BAAB fields (Figure 25(c)).

In addition, to evaluate the geochemical and tectonic affinities of a wide range of basaltic magmas produced in divergent, convergent, and intraplate environments in the Bogoin Complex, Saccani [158] proposed discrimination diagrams (Figure 25(d) and Figure 25(e)) based on Th and Nb normalized to the N-MORB composition ([76]; Table 6).

These figures distinguish three different types of convergent plate margin settings that delineate distinct fields for island arcs with complex polygenetic crustal signatures: 1) increasing Th/Nb compositions, indicating the interaction between subduction components and mantle wedge, and 2) decreasing Th/Nb compositions, defining an array of mantle depletion without input from subduction-derived components.

Back-arc basin basalts have been divided into immature and mature intra-oceanic back-arcs, which are separated by fields with varying contributions from subduction and crystal materials (Back arc "A") and no contributions from subduction and crystal materials (Back arc "B"), respectively. In the tectonic discriminating plot between Th_N and Nb_N (Figure 25(d)), the majority of the amphibolite samples are found in the field of back-arc basin basalts. All granitic gneisses and metadiorite samples exhibit an affinity for arc-generated calc-alkaline basalts (CAB).

In mature, ensimatic volcanic arc environments, calc-alkaline basalts (CAB) frequently develop (*e.g.*, Sierra Nevada, California; Guatemala-Cuba-Venezuela, Central America). They are frequently found in volcanic-arc rocks, which are distinct from ophiolites from supra-subduction zones by having a thicker and more developed arc crust [159].

According to Dilek *et al.*, [159], the polygenetic crustal structure of volcanic arc settings substantially favours crustal chemical input and wall rock assimilation, which results in a significant enrichment in Th and LREE relative to Nb and HREE, respectively. More often than not, these basalts exhibit Ta, P, and Ti depletion, which is thought to indicate partial melting of depleted mantle sources (*e.g.*, [160]).

According to Pearce [161], P-MORB and E-MORB arise at plume-distal ridge settings, whereas N-MORB occurs at plume-proximal ridge settings. In agreement with this result, the amphibolite samples of the Bogoin Complex show a preference for ridge placements in an intra-oceanic arc (**Figure 25(d)**, **Figure 25(e)**). Furthermore, the majority of granitic gneisses and metadiorite samples exhibit Nb, Ta, and Ti depletion in the primitive mantle-normalized multi-element plots (**Figure 18(e)**), which are often observed in the arc basalt environment [162]-[164]. The granitic gneisses and metadiorite samples of the Bogoin area **Figure 25(e)** also correlate to a continental edge volcanic arc (**Figure 25(d)**, **Figure 25(e)**. The amphibolite samples of the Bogoin area exhibiting affinity towards back-arc 'A' are characterized by the input of subduction or crustal components as evidenced by immature back-arcs (**Figure 25(e)**).

Many tectonic discrimination diagrams based on immobile components are used to limit the geodynamic setting of metamorphosed mafic rocks [161] [165]. Similar to the Mewengo garnet amphibolite presented for comparison, the studied amphibolites display back-arc and E-MORB [79] [166]-[170] characteristics in the La/10-Nb/8-Y/15 ternary diagram (**Figure 25(f)**) published by Cabanis [171]. The examined amphibolite samples generally feature arc tholeiites and back-arc characteristics in contrast to those in the south domain of Cameroon (Nyong complex).

The Bogoin region is located in the same extension of the southern domain of Cameroon [47]. During this studie, the geochemical characteristics of the Bogoin rocks were similar to those of the Nyong complex. Recent geochemical, isotopic and geochronological studies conducted in the southern domain of Cameroon, more specifically in the Nyong complex, have highlighted the significance of early Palaeoproterozoic accretionary episodes, which indicate significant crustal growth and reworking events (*e.g.*, [166] [167] [170] [172] [173]). Paleoproterozoic subduction may have taken place beneath a concealed Archean block (*i.e.*, a continental arc), according to many Neo- and Meso-archean zircon crystals in IFs of the Nyong Complex. The tectonic environment of the Nyong Complex during the Trans-Amazonian Eburnean Orogeny is associated with this geodynamic evolution (*e.g.*, [131] [167] [168] [170] [174] [175]). From silica-poor phases linked to the early stages of convergent plate boundary development to highly advanced magmas signifying the end of subduction, continental arcs contain a wide variety of compositions [6]. The Nyong Complex's mafic and ultramafic metavolcanic rocks are remnants of an early arc stage dated at around 2.1 Ga in previous regional studies [131] [170] [175]. During this time, partial mantle melting and IF deposition at around 2422 ± 50 Ma (a published U-Pb zircon age) produced tholeiitic magmas. Given the age that corresponds with the typical Cordilleran phase and the emplacement of the meta-to-peraluminous magma associated with this study, it is possible that the latter was produced during continuous subduction, which inevitably involved a brief collisional episode in which calc-alkaline affinity magmas were generated. The evolution of the Alto Moxoto Complex in northeastern Brazil is comparable to this orogeny [176].

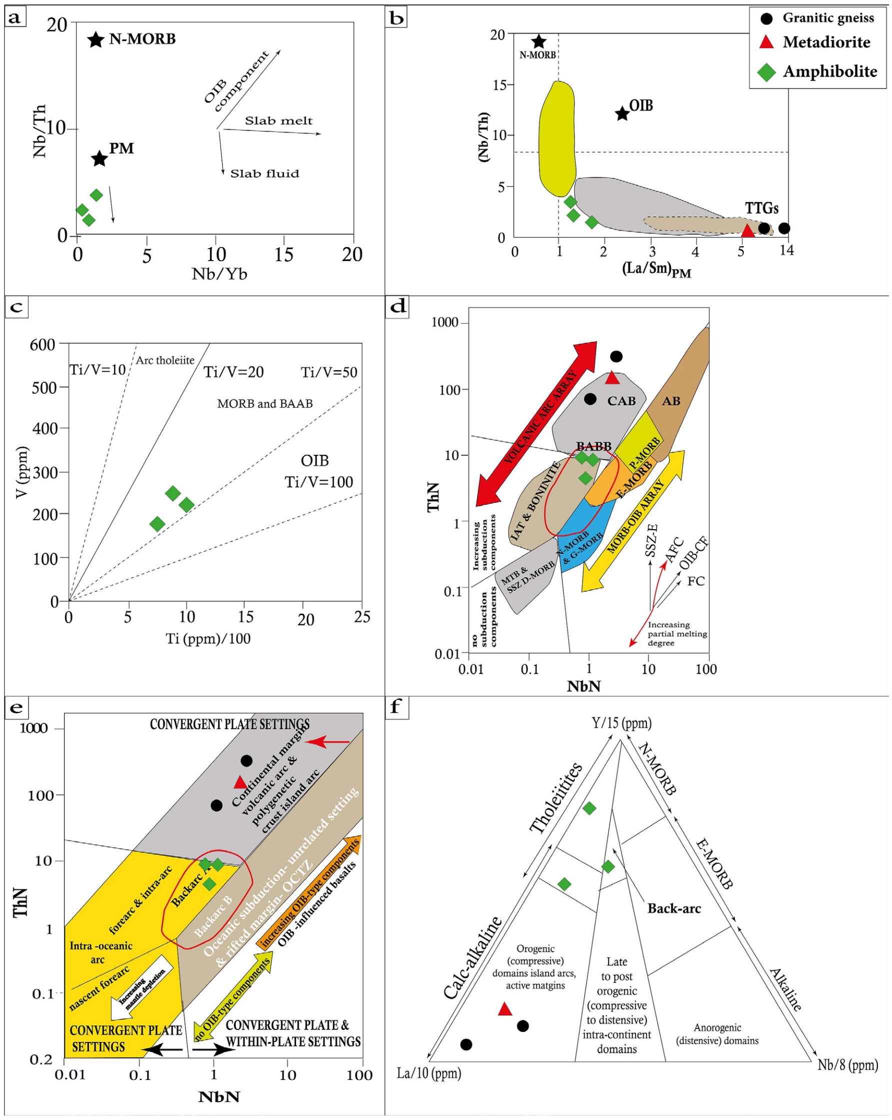

Figure 25. (a) Nb/Th versus Nb/Yb plot for the mafic rocks of the study area (after [156]); (b) Nb/Th vs. (La/Sm)$_{PM}$ for the sample rocks of Bogoin, N-MORB: normal mid-oceanic ridge basalts, OIB: oceanic island basalts, OPB: oceanic plateau basalts, AVR: arc volcanic rocks, TTGs: tonalite-trondhjemite-granodiorites. Dashed lines indicate primitive mantle values [76]. MORB, OIB, and primitive mantle-normalizing values are from [76]. Shaded areas for OPB, AVR, and TTGs are from [177]; (c) Ti versus V diagram by [157]; (d) (e) (Th)$_N$ versus (Nb)$_N$ diagram (after [158]) showing different tectonic settings of magmatic rocks of diverse composition; (f) La/10-Nb/8- Y/15 after [171].

4.2.3. Brittle-Ductile Tectonic

The Bogoin area was heavily affected by ductile deformation. However, field and petrographic data indicate the presence of both brittle and ductile structures in the ore layer. The D_2 event was superimposed on the D_1, transposing S1 foliation into S_2 foliation along C_2 sinistral shear planes (**Figure 15(b)**). C_2 shear planes are present at all scales within this greenstone belt (refer to **Figure 15(b)**). These planes are characterized by blastomylonitic shear zones at both mesoscopic and macroscopic scales. The C_2 blastomylonitic shear bands observed in the migmatite gneiss, itabirites, amphibolites and chloritoschistes with dextral to sinistral shear movements. D3 phase is characterized by NNE-SSW to NE-SW dextral shear markers. The tectonic history of Bogoin area is characterized by a D1 compressive phase, and aerly sinistral syn-D_2 and late dextral syn-D_3 transcurrent shear deformation evidenced by 1) transpressional shear markers such as high-angle reverse faulting that were subsequently reactivated by strike-slip faults.

The lineament map shows a preferential N-S direction for the Bogoin zone consistent with D_2 deformation phase. It shows structures with variable directions. The N-S lineament direction appears to be the main one affecting the study area. In addition, the lineament density map shows the frequency of lineaments per unit area. The rose diagram of directions corresponding to the lineament map in **Figure 17** shows that areas with the highest density of lineaments are located to the south and south-west of Bogoin, at Gbélét, Dongbara, and to the north-east of Bogoin (**Figure 12(a)**). The discontinuities identified from map form the basis for a frequency analysis that reveals the main directions, which can then be compared with the structural data measured in the field (**Figure 17**).

The overall statistical analysis of Bogoin lineaments shows three preferred directions, broadly oriented N-S, W-E and NW-SE (**Figure 17**): 1) the dominant direction oriented N-S. It comprises two sub-classes: The N0˚E sub-class and the N010˚E sub-class; 2) the second, less dominant direction is oriented NW-SE. It also includes two sub-classes oriented N150˚E and N180˚E, 3) the third class has a less pronounced direction and is oriented W-E. It includes two sub-classes oriented N150˚E and N180˚E. It includes two sub-classes oriented N90˚E and N100˚E.

5. Conclusions

Cartographic studies combined with satellite image processing have enabled the production of a lithostructural map of the Bogoin area. Petrographic studies have classified the area as a metamorphic complex divided into two main groups: the iron deposit and the metamorphosed host rocks that form the granitoid basement of the Bogoin complex, composed of orthogneiss and mafic rocks.

Geochemical data show that the metamorphosed mafic rocks display metaluminous and tholeiitic magmas affinities but tend towards a calc-alkaline nature suggesting a mixed source crystallized in a continental crust-arc-related setting and mantle input, and also reveal an immature back-arcs and thickened crust during the Eburnean Trans-Amazonian orogenic belts in the Bogoin Complex.

The geotectonic evolution of the host rocks associated with the iron formation of the Bogoin iron deposit is related to the Paleoproterozoic (Eburnean-Trans-Amazonian) process of subduction and collision along an extending continental margin, where the dominant iron-bearing rock assemblages undergo a sequential geodynamic change from extension to compression similar to Nyong complex in Cameroon.

The Bogoin area was heavily affected by three phases of deformation: a compressive D_1 deformation, an early sinistral D_2 deformation, and a late dextral D3 deformation, with D_2 and D_3 corresponding to transcurrent deformation.

Acknowledgements

This study was carried out as part of the research activities conducted on the northern edge of the Congo Craton by the first author. We extend our sincere thanks to the publisher and the anonymous reviewers for their critical comments on the manuscript.

Author Contributions

Conceptualization, Rodrigue Martial Topien; methodology, Rodrigue Martial Topien and Maurice Kwékam; software, Rodrigue Martial Topien; validation, Rodrigue Martial Topien, Jules Tcheumenak Kouémo and Maurice Kwékam; formal analysis, Rodrigue Martial Topien; investigation, Rodrigue Martial Topien, Cyrille Prosper Ndepete and José Kpéou; resources, Rodrigue Martial Topien and Cyrille Prosper Ndepete; data curation, Rodrigue Martial Topien; writing—original draft preparation, Rodrigue Martial Topien; writing—review and editing, Rodrigue Martial Topien, Jules Tcheumenak Kouémo, Cyrille Prosper Ndepete, José Kpéou, Gaetan Moloto-A-Kenguemba and Maurice Kwékam; visualization, Rodrigue Martial Topien; supervision, Gaetan Moloto-A-Kenguemba and Maurice Kwékam; project administration, Rodrigue Martial Topien. All authors have read and agreed to the published version of the manuscript.

Conflicts of Interest

The authors declare no conflicts of interest regarding the publication of this paper.

References

[1] de Wit, M.J. and Ashwal, L.D. (1995) Greenstone Belts: What Are They? *South African Journal of Geology*, **98**, 505-520. https://hdl.handle.net/10520/EJC-943d19ff8

[2] Thallapalli, B., Kumari, V., Krishna, K., Ravi, C. and Prasad, S. (2017) Petrogenesis of Ultramafics and Mafics of Batampudi Complex, Khammam District, Telangana state, South India. *International Journal of Applied Environmental Sciences*, **12**, 1091-1110. https://www.researchgate.net/publication/318110142_Petrogenesis_of_ultramafics_and_mafics_of_batampudi_complex_Khammam_district_Telangana_state_South_India

[3] Su, B., Qin, K., Sakyi, P.A., Li, X., Yang, Y., Sun, H., *et al.* (2011) U-Pb Ages and Hf-O Isotopes of Zircons from Late Paleozoic Mafic-Ultramafic Units in the Southern Central Asian Orogenic Belt: Tectonic Implications and Evidence for an Early-Permian Mantle Plume. *Gondwana Research*, **20**, 516-531. https://doi.org/10.1016/j.gr.2010.11.015

[4] Cai, K., Sun, M., Yuan, C., Zhao, G., Xiao, W. and Long, X. (2012) Keketuohai Mafic-Ultramafic Complex in the Chinese Altai, NW China: Petrogenesis and Geodynamic Significance. *Chemical Geology*, **294**, 26-41.

https://doi.org/10.1016/j.chemgeo.2011.11.031

[5] Zhang, J., Yu, M., Wang, H., Li, B., Feng, C., Dick, J.M., *et al.* (2021) Geodynamic Setting and Cu-Ni Potential of Late Permian Xiwanggou Mafic-Ultramafic Rocks, East Kunlun Orogenic Belt, NW China. *Frontiers in Earth Science*, **9**, Article ID: 666967. https://doi.org/10.3389/feart.2021.666967

[6] de Lira Santos, L.C.M., Lages, G.A., Caxito, F.A., Dantas, E.L., Cawood, P.A., Lima, H.M., *et al.* (2022) Isotopic and Geochemical Constraints for a Paleoproterozoic Accretionary Orogen in the Borborema Province, NE Brazil: Implications for Reconstructing Nuna/Columbia. *Geoscience Frontiers*, **13**, Article 101167. https://doi.org/10.1016/j.gsf.2021.101167

[7] Cassidy, K.F., Champion, D.C. and Huston, D.L. (2005) Crustal Evolution Constraints on the Metallogeny of the Yilgarn Craton. In: Mao, J. and Bierlein, F.P., Eds., *Mineral Deposit Research*: *Meeting the Global Challenge*, Springer, 901-904. https://doi.org/10.1007/3-540-27946-6_229

[8] Singh, S.P., Subramanyam, K.S.V., Manikyamba, C., Santosh, M., Rajanikanta Singh, M. and Chandan Kumar, B. (2018) Geochemical Systematics of the Mauranipur-Babina Greenstone Belt, Bundelkhand Craton, Central India: Insights on Neoarchean Mantle Plume-Arc Accretion and Crustal Evolution. *Geoscience Frontiers*, **9**, 769-788. https://doi.org/10.1016/j.gsf.2017.08.008

[9] Zhang, H., Chen, L., Santosh, M. and Menzies, M.A. (2013) Construction and Destruction of Cratons: Preface. *Gondwana Research*, **23**, 1-3. https://doi.org/10.1016/j.gr.2012.06.006

[10] Yang, Q., Santosh, M., Shen, J. and Li, S. (2014) Juvenile vs. Recycled Crust in NE China: Zircon U-Pb Geochronology, Hf Isotope and an Integrated Model for Mesozoic Gold Mineralization in the Jiaodong Peninsula. *Gondwana Research*, **25**, 1445-1468. https://doi.org/10.1016/j.gr.2013.06.003

[11] Singh, M.R., Manikyamba, C., Ray, J., Ganguly, S., Santosh, M., Saha, A., *et al.* (2016) Major, Trace and Platinum Group Element (PGE) Geochemistry of Archean Iron Ore Group and Proterozoic Malangtoli Metavolcanic Rocks of Singhbhum Craton, Eastern India: Inferences on Mantle Melting and Sulphur Saturation History. *Ore Geology Reviews*, **72**, 1263-1289. https://doi.org/10.1016/j.oregeorev.2015.04.024

[12] Zhou, M. (1994) PGE Distribution in 2.7-Ga Layered Komatiite Flows from the Belingwe Greenstone Belt, Zimbabwe. *Chemical Geology*, **118**, 155-172. https://doi.org/10.1016/0009-2541(94)90174-0

[13] Song, X.-Y. and Li, X.-R. (2009) Geochemistry of the Kalatongke Ni-Cu-(PGE) Sulfide Deposit, NW China: Implications for the Formation of Magmatic Sulfide Mineralization in a Postcollisional Environment. *Mineralium Deposita*, **44**, 303-327. https://doi.org/10.1007/s00126-008-0219-x

[14] Song, X., Wang, Y. and Chen, L. (2011) Magmatic Ni-Cu-(PGE) Deposits in Magma Plumbing Systems: Features, Formation and Exploration. *Geoscience Frontiers*, **2**, 375-384. https://doi.org/10.1016/j.gsf.2011.05.005

[15] Ebah Abeng, S.A., Ndjigui, P., Beyanu, A.A., Teutsong, T. and Bilong, P. (2012) Geochemistry of Pyroxenites, Amphibolites and Their Weathered Products in the Nyong Unit, SW Cameroon (NW Border of Congo Craton): Implications for Au-PGE Exploration. *Journal of Geochemical Exploration*, **114**, 1-19. https://doi.org/10.1016/j.gexplo.2011.11.003

[16] Kepezhinskas, P.K., Eriksen, G.M.D. and Kepezhinskas, N.P. (2016) Geochemistry of Ultramafic to Mafic Rocks in the Norwegian Lapland: Inferences on Mantle Sources and Implications for Diamond Exploration. *Earth Science Research*, **5**, 148-187.

https://doi.org/10.5539/esr.v5n2p148

[17] Ramiz, M.M., Mondal, M.E.A. and Farooq, S.H. (2019) Geochemistry of Ultramafic-Mafic Rocks of the Madawara Ultramafic Complex in the Southern Part of the Bundelkhand Craton, Central Indian Shield: Implications for Mantle Sources and Geodynamic Setting. *Geological Journal*, **54**, 2185-2207. https://doi.org/10.1002/gj.3290

[18] Santosh, M. and Groves, D.I. (2022) Global Metallogeny in Relation to Secular Evolution of the Earth and Supercontinent Cycles. *Gondwana Research*, **107**, 395-422. https://doi.org/10.1016/j.gr.2022.04.007

[19] Biandja, J. (1988) Approche métallogénique du "Greenstone Belt" de Bogoin (RCA). Sa minéralisation en or. Ph.D. Thesis, Université Pierre et Marie Curie—Paris VI. https://theses.hal.science/tel-01053229

[20] Poidevin, J. (1994) Boninite-Like Rocks from the Palaeoproterozoic Greenstone Belt of Bogoin, Central African Republic: Geochemistry and Petrogenesis. *Precambrian Research*, **68**, 97-113. https://doi.org/10.1016/0301-9268(94)90067-1

[21] Simonet, V., Hippert, F., Audier, M. and Bellissent, R. (2001) Local Order in Liquids Forming Quasicrystals and Approximant Phases. *Physical Review B*, **65**, Article 024203. https://doi.org/10.1103/physrevb.65.024203

[22] Rosière, C.A., Baars, F.J., Seoane, J.C.S., Lobato, L.M., da Silva, L.L., de Souza, S.R.C., *et al.* (2006) Structure and Iron Mineralisation of the Carajás Province. *Applied Earth Science*, **115**, 126-133. https://doi.org/10.1179/174327506x138986

[23] Martins Pereira, S.L., Lobato, L.M., Ferreira, J.E. and Jardim, E.C. (2007) Nature and Origin of the Bif-Hosted São Bento Gold Deposit, Quadrilátero Ferrífero, Brazil, with Special Emphasis on Structural Controls. *Ore Geology Reviews*, **32**, 571-595. https://doi.org/10.1016/j.oregeorev.2005.03.018

[24] Angerer, T., Hagemann, S.G. and Danyushevsky, L.V. (2012) Geochemical Evolution of the Banded Iron Formation-Hosted High-Grade Iron Ore System in the Koolyanobbing Greenstone Belt, Western Australia. *Economic Geology*, **107**, 599-644. https://doi.org/10.2113/econgeo.107.4.599

[25] Egglseder, M.S., Cruden, A.R., Dalstra, H.J. and Nicholas, L. (2017) The Role of Deformation in the Formation of Banded Iron Formation-Hosted High-Grade Iron Ore Deposits, Hamersley Province (Australia). *Precambrian Research*, **296**, 62-77. https://doi.org/10.1016/j.precamres.2017.04.034

[26] Swiffa Fajong, I., Nzepang Tankwa, M., Fossi, D.H., Ganno, S., Moudioh, C., Soh Tamehe, L., *et al.* (2022) Lithostratigraphy, Origin, and Geodynamic Setting of Iron Formations and Host Rocks of the Anyouzok Region, Congo Craton, Southwestern Cameroon. *Minerals*, **12**, Article 1198. https://doi.org/10.3390/min12101198

[27] Ndema Mbongué, J.-L., Sigué, C., Djomo Michel, C., Nga Essomba Tsoungui, P.E., Mukete, C.D. and Kamdoum Tchouatchou, S.G. (2023) Petrogenetic Characterization of Banded Iron Formations of Bidjouka Area, Nyong Complex, Southern Cameroon: Implication for the Origin and Depositional Environment of Paleoproterozoic BIFs. *SSRN*.

[28] Poidevin, J.L., Dostal, J. and Dupuy, C. (1981) Archaean Greenstone Belt from the Central African Republic (Equatorial Africa). *Precambrian Research*, **16**, 157-170. https://doi.org/10.1016/0301-9268(81)90011-5

[29] Bessoles, B. and Trompette, R. (1980) Geologie de l'afrique, la chaine panafricaine "Zone mobile d'afrique centrale (partie sud) et zone mobile soudanaise". https://pascal-francis.inist.fr/vibad/index.php?action=getRecordDetail&idt=PASCALGEODEBRGM8120168309

[30] Jackson, N.J. and Ramsay, C.R. (1980) Time-Space Relationships of Upper Precambrian Volcanic and Sedimentary Units in the Central Arabian Shield. *Journal of the Geological Society*, **137**, 617-628. https://doi.org/10.1144/gsjgs.137.5.0617

[31] Poidevin, J.L. and Pin, C. (1986) 2 Ga U-Pb Zircon Dating of Mbi Granodiorite (Central African Republic) and Its Bearing on the Chronology of the Proterozoic of Central Africa. *Journal of African Earth Sciences* (1983), **5**, 581-587. https://doi.org/10.1016/0899-5362(86)90024-2

[32] Pin, C. and Poidevin, J. (1987) U-Pb Zircon Evidence for a Pan-African Granulite Facies Metamorphism in the Central African Republic. A New Interpretation of the High-Grade Series of the Northern Border of the Congo Craton. *Precambrian Research*, **36**, 303-312. https://doi.org/10.1016/0301-9268(87)90027-1

[33] Cornacchia, M. and Giorgi, L. (1989) Discordances majeures et magmatismes des séries précambriennes de la région de Bogoin (Centre ouest de la République Centrafricaine). *Journal of African Earth Sciences* (*and the Middle East*), **9**, 221-226. https://doi.org/10.1016/0899-5362(89)90065-1

[34] Lavreau, J., Poidevin, J.L., Ledent, D., Liegeois, J.P. and Weis, D. (1990) Contribution to the Geochronology of the Basement of the Central African Republic. *Journal of African Earth Sciences* (*and the Middle East*), **11**, 69-82. https://doi.org/10.1016/0899-5362(90)90078-s

[35] Rolin, P. (1992) Présence d'un chevauchement ductile majeur d'âge panafricain dans la partie centrale de la République Centrafricaine: Résultats préliminaires. *Comptes Rendus de l'Académie des Sciences. Série II, Mécanique-Physique, Chimie, Sciences de la Terre et de l'Univers*, **315**, 467-470. http://pascal-francis.inist.fr/vibad/index.php?action=getRecordDetail&idt=5582424

[36] Nzenti, J.P. (1998) Neoproterozoic Alkaline Meta-Igneous Rocks from the Pan-African North Equatorial Fold Bel (Yaounde, Cameroon): Biotitites and Magnetite Rich Pyroxenites. *Journal of African Earth Sciences*, **26**, 37-47. https://doi.org/10.1016/s0899-5362(97)00135-8

[37] Hubert, M., Emilien, D.Y.P., Nzenti, J.P., Jean, B., Boniface, K. and Emmanuel, S.C. (2011) Major Structural Features and the Tectonic Evolution of the Bossangoa-Bossembele Basement, Northwestern Central African Republic. *The Open Geology Journal*, **5**, 21-32. https://doi.org/10.2174/1874262901105010021

[38] Topien, R.M. (2012) Pétrologie structurale et géochimique des granitoïdes de la région de Fambélé Garoua-Boulaï (Ouest RCA). Master's Thesis, Université de Dschang. https://www.researchgate.net/publication/384908582_Petrologie_structurale_et_geochimie_des_granitoides_de_la_region_de_Fambele-Garoua_Boulai_Ouest_RCA

[39] Ouabego Kourtene, M. (2013) Contribution à l'étude de la chaine panafricaine des Oubanguides en République Centrafricaine. Ph.D. Thesis, Aix-Marseille Université.

[40] Danguene, P.E.Y., Ngnotue, T., Ganno, S., Biandja, J., Kankeu, B. and Nzenti, J.P. (2014) Paleoproterozoic synkinematic magnesian high-K magmatism from the Tamkoro-Bossangoa Massif, along the Bossangoa-Bossembele shear zone in North-Western Central African Republic. *Journal of Geosciences and Geomatics*, **2**, 151-164.

[41] Topien, R.M., Moloto-A-Kenguemba, G., Traore, M., Rajendran, S. and Kouassi, B.R. (2023) Litho-Structural Mapping and Structural Evolution of the Bocaranga Pluton, Northwest Adamawa-Yadé Domain, Central African Republic. *Journal of African Earth Sciences*, **198**, Article 104793. https://doi.org/10.1016/j.jafrearsci.2022.104793

[42] Topien, R.M. (2012) Cartographie, pétrologie et analyse structurale du complexe plutonique de Bocaranga, domaine nord de la Ceinture Orogénique d'Afrique Centrale

en RCA. Ph.D. Thesis, Université de Bangui. https://hal.science/tel-05151333/

[43] Cornacchia, M. and Dars, R. (1983) Un trait structural majeur du continent Africain; les lineaments centrafricains du Cameroun au Golfe d'Aden. *Bulletin de la Société Géologique de France*, **7**, 101-109. https://doi.org/10.2113/gssgfbull.s7-xxv.1.101

[44] Toteu, S.F., Van Schmus, W.R., Penaye, J. and Michard, A. (2001) New U-Pb and Sm-Nd Data from North-Central Cameroon and Its Bearing on the Pre-Pan African History of Central Africa. *Precambrian Research*, **108**, 45-73. https://doi.org/10.1016/s0301-9268(00)00149-2

[45] Toteu, S.F., Penaye, J. and Djomani, Y.P. (2004) Geodynamic Evolution of the Pan-African Belt in Central Africa with Special Reference to Cameroon. *Canadian Journal of Earth Sciences*, **41**, 73-85. https://doi.org/10.1139/e03-079

[46] Topien, R.M., Tcheumenak Kouémo, J., Kpéou, J., Moloto-A-Kenguemba, G. and Kwékam, M. (2024) Petrology of the Pan-African High-K Alkali-Calcic Bocaranga Plutonic Complex in the Adamawa-Yadé Domain (Central African Republic): Nature, Origin and Contribution to Geodynamic Reconstruction of the Central African Fold Belt. *Solid Earth Sciences*, **9**, Article 100211. https://doi.org/10.1016/j.sesci.2024.100211

[47] Topien, R.M., Tcheumenak Kouémo, J., Kpéou, J., Moloto-A-Kenguemba, G. and Kwékam, M. (2025) Mineralogy and Bulk-Rock Geochemistry of Mafic Rocks from Bocaranga, Adamawa-Yadé Domain of Central African Republic: Evidence of Paleao-Oceanic Crust on the Northern Edge of the Congo Craton. *Geological Journal*, **60**, 2380-2416. https://doi.org/10.1002/gj.5177

[48] Poidevin, J.-L. (1991) Les ceintures de roches vertes de la République Centrafricaine (Bandas, Boufoyo, Bogoin, Mbomou). Contribution à la connaissance du Précambrien du nord du craton du Congo. Ph.D. Thesis, Université Blaise Pascal, Clermont-Ferrand II. https://theses.fr/1991CLF2E423

[49] Abdelsalam, M.G., Gao, S.S. and Liégeois, J. (2011) Upper Mantle Structure of the Saharan Metacraton. *Journal of African Earth Sciences*, **60**, 328-336. https://doi.org/10.1016/j.jafrearsci.2011.03.009

[50] Meert, J.G. and Lieberman, B.S. (2008) The Neoproterozoic Assembly of Gondwana and Its Relationship to the Ediacaran-Cambrian Radiation. *Gondwana Research*, **14**, 5-21. https://doi.org/10.1016/j.gr.2007.06.007

[51] Mestraud, J.L. and Bessoles, B. (1982) Géologie et ressources minérales de la République Centrafricaine: État des connaissances à fin 1963. Editions du BRGM (Mémoires du BRGM, no 60). https://pascal-francis.inist.fr/vibad/index.php?action=getRecordDetail&idt=PASCALGEODEBRGM8220223850

[52] Moloto-A-Kenguemba, G.R. (2002) Evolution géotectonique paléoprotérozoïque à néoprotérozoïque de la couverture du craton archéen du Congo aux confins du Congo, du Cameroun et de Centrafrique. Ph.D. Thesis, Université d'Orléans. https://theses.fr/2002ORLE2034

[53] Tchakounté, J.N., Toteu, S.F., Schmus, W.R.V., Penaye, J., Deloule, É., Ondoua, J.M., *et al.* (2007) Evidence of Ca 1.6-Ga Detrital Zircon in the Bafia Group (Cameroon): Implication for the Chronostratigraphy of the Pan-African Belt North of the Congo Craton. *Comptes Rendus. Géoscience*, **339**, 132-142. https://doi.org/10.1016/j.crte.2007.01.004

[54] Van Schmus, W.R., Oliveira, E.P., Da Silva Filho, A.F., Toteu, S.F., Penaye, J. and Guimarães, I.P. (2008) Proterozoic Links between the Borborema Province, NE Brazil, and the Central African Fold Belt. In: Pankhurst, R.J., Trouw, R.A.J., Brito Neves,

B.B. and De Wit, M.J., Eds., *West Gondwana: Pre-Cenozoic Correlations across the South Atlantic Region* (Vol. 294), Geological Society, 69-99.
https://pubs.geoscienceworld.org/books/edited-volume/1664/chapter/107478924

[55] Cornacchia, M. and Giorgi, L. (1986) Les séries précambriennes d'origine sédimentaire et volcano-sédimentaire de la République Centrafricaine. Musée Royal de l'Afrique Centrale (Annales du Musée Royal de l'Afrique Centrale. Sciences Géologiques, no 93).
https://pascal-francis.inist.fr/vibad/index.php?action=getRecordDetail&idt=7088652

[56] Giorgi, L., Cornacchia, M., Vicat, J.-P., Blondin, P., Babet, N. and Minot, J.-B. (1990) Géochimie des métavolcanites de la ceinture de roches vertes de Bogoin-Boali, République Centrafricaine. *Publication Occasionnelle-Centre International Pour la Formation et les Échanges Géologiques*, No. 22, 37-40.
http://pascal-francis.inist.fr/vibad/index.php?action=getRecordDetail&idt=6453318

[57] Rolin, P. (1995) La zone de décrochements panafricains des Oubanguides en République Centrafricaine. Comptes Rendus de l'Académie des Sciences. *Série II, Sciences de la Terre et des Planètes*, **320**, 63-69.
http://pascal-francis.inist.fr/vibad/index.php?action=getRecordDetail&idt=3427469

[58] Boulvert, Y. (1995) Documents phytogéographiques sur les savanes centrafricaines. ORSTOM Éditions.
https://horizon.documentation.ird.fr/exl-doc/pleins_textes/pleins_textes_2/etudes_theses/43230.pdf

[59] Jawahar Raj, N. and Prabhakaran, A. (2018) Lineaments of Kodaikanal-Palani Massif, Southern Granulitic Terrain of Tamil Nadu, India: A Study Using SRTM DEM and LANDSAT Satellite's OLI Sensor's FCC. *Geology, Ecology, and Landscapes*, **2**, 188-202. https://doi.org/10.1080/24749508.2018.1452477

[60] Hashim, M., Ahmad, S., Johari, M.A.M. and Pour, A.B. (2013) Automatic Lineament Extraction in a Heavily Vegetated Region Using Landsat Enhanced Thematic Mapper (ETM+) Imagery. *Advances in Space Research*, **51**, 874-890.
https://doi.org/10.1016/j.asr.2012.10.004

[61] Boardman, J.W., Kruse, F.A. and Green, R.O. (1995) Mapping Target Signatures via Partial Unmixing of AVIRIS Data. *Summaries of the Fifth Annual JPL Airborne Earth Science Workshop*, **1**, 23-26. https://ntrs.nasa.gov/citations/19950027316

[62] Anzar, F., Soulaimani, A., Jaffal, M., Ilmen, S. and Kassoui, W. (2025) Structural Analysis and Hydrothermal Alteration Detection Using Satellite Imagery: Implications for Ore Prospecting in the Proterozoic Bou Azzer-El Graara Inlier (Central Anti-Atlas, Morocco). *Mediterranean Geoscience Reviews*, **7**, 1057-1078.
https://doi.org/10.1007/s42990-025-00192-4

[63] Amri, K., Mahdjoub, Y. and Guergour, L. (2011) Use of Landsat 7 ETM+ for Lithological and Structural Mapping of Wadi Afara Heouine Area (Tahifet-Central Hoggar, Algeria). *Arabian Journal of Geosciences*, **4**, 1273-1287.
https://doi.org/10.1007/s12517-010-0180-8

[64] Rolin, P. and Stussi, J.M. (1991) Decrochements intracrustaux et intrusions granitiques carboniferes dans le Morvan (Massif Central Francais). *Bulletin de la Société Géologique de France*, **162**, 123-130. https://doi.org/10.2113/gssgfbull.162.1.123

[65] Abrams, M.J., Rothery, D.A. and Pontual, A. (1988) Mapping in the Oman Ophiolite Using Enhanced Landsat Thematic Mapper Images. *Tectonophysics*, **151**, 387-401.
https://doi.org/10.1016/0040-1951(88)90254-5

[66] Gad, S. and Kusky, T. (2006) Lithological Mapping in the Eastern Desert of Egypt,

the Barramiya Area, Using Landsat Thematic Mapper (TM). *Journal of African Earth Sciences*, **44**, 196-202. https://doi.org/10.1016/j.jafrearsci.2005.10.014

[67] Himyari, M.S., Hoepffner, C., Benzakour, M. and El Hadani, D. (2002) Etude structurale du haut atlas oriental (Maroc) à l'aide de l'analyse linéamentaire des images HRV (XS) de SPOT. *Télédétection*, **2**, 243-253. https://www.researchgate.net/publication/228580720_Etude_structurale_du_Haut_Atlas_Oriental_Maroc_a_l'aide_de_l'analyse_lineamentaire_des_images_HRV_XS_de_SPOT

[68] Djemai, S., Bendaoud, A., Deroin, J.-P., *et al.* (2012) Apport des images Landsat 7 ETM+ pour la cartographie géologique des terrains précambriens en zone aride: Exemple de la région d'Amesmessa (Sud in Ouzzal, Hoggar, Algérie). *Photo Interprétation, European Journal of Applied Remote Sensing*, **48**, 7-12. https://www.semanticscholar.org/paper/APPORT-DES-IMAGES-LANDSAT-7-ETM%2B-POUR-LA-G%C3%89OLOGIQUE-Djemai-Bendaoud/7ce3df8c572c24868699dabafb5a0112be71ed92#related-papers

[69] Goscombe, B.D. and Passchier, C.W. (2003) Asymmetric Boudins as Shear Sense Indicators—An Assessment from Field Data. *Journal of Structural Geology*, **25**, 575-589. https://doi.org/10.1016/s0191-8141(02)00045-7

[70] Goscombe, B.D., Passchier, C.W. and Hand, M. (2004) Boudinage Classification: End-Member Boudin Types and Modified Boudin Structures. *Journal of Structural Geology*, **26**, 739-763. https://doi.org/10.1016/j.jsg.2003.08.015

[71] Frost, B.R., Barnes, C.G., Collins, W.J., Arculus, R.J., Ellis, D.J. and Frost, C.D. (2001) A Geochemical Classification for Granitic Rocks. *Journal of Petrology*, **42**, 2033-2048. https://doi.org/10.1093/petrology/42.11.2033

[72] Djibril, K.N.G., Dieudonné, M., Estelle, N.E.T.P., Marion, K.W.M., Patrick, A.K., Brice, K.W., *et al.* (2022) Geochemistry and U-Pb Zircon Geochronology of Granitic Gneisses in the Mewengo Iron Deposits: Evidence of Archean Fingerprints within the Paleoproterozoic Nyong Group, Cameroon. *Arabian Journal of Geosciences*, **15**, Article No. 1498. https://doi.org/10.1007/s12517-022-10775-2

[73] Bas, M.J.L., Maitre, R.W.L., Streckeisen, A. and Zanettin, B. (1986) A Chemical Classification of Volcanic Rocks Based on the Total Alkali-Silica Diagram. *Journal of Petrology*, **27**, 745-750. https://doi.org/10.1093/petrology/27.3.745

[74] Peccerillo, A. and Taylor, S.R. (1976) Geochemistry of Eocene Calc-Alkaline Volcanic Rocks from the Kastamonu Area, Northern Türkiye. *Contributions to Mineralogy and Petrology*, **58**, 63-81. https://doi.org/10.1007/bf00384745

[75] McDonough, W.F. and Sun, S.-S. (1995) The Composition of the Earth. *Chemical Geology*, **120**, 223-253. https://doi.org/10.1016/0009-2541(94)00140-4

[76] Sun, S.-S. and McDonough, W.F. (1989) Chemical and Isotopic Systematics of Oceanic Basalts: Implications for Mantle Composition and Processes. *Geological Society, London, Special Publications*, **42**, 313-345. https://doi.org/10.1144/gsl.sp.1989.042.01.19

[77] Anders, E. and Grevesse, N. (1989) Abundances of the Elements: Meteoritic and Solar. *Geochimica et Cosmochimica Acta*, **53**, 197-214. https://doi.org/10.1016/0016-7037(89)90286-X

[78] Jensen, L.S. (1976) A New Cation Plot for Classifying Subalkalic Volcanic Rocks. Miscellaneous Paper No. 66, Ontario Division of Mines. https://cir.nii.ac.jp/crid/1370002218265210893

[79] Marion, K.W.M., Djibril, K.N.G., Guimollaire, N.D. and Patrick, A.K. (2021) Petro-

genesis and U-Pb Zircon Dating of Amphibolite in the Mewengo Iron Deposit, Nyong Series, Cameroon: Fingerprints of Iron Depositional Geotectonic Setting. *Arabian Journal of Geosciences*, **14**, Article No. 872.
https://doi.org/10.1007/s12517-021-07235-8

[80] Murray, R.W., Buchholtz ten Brink, M.R., Gerlach, D.C., Russ, G.P. and Jones, D.L. (1992) Interoceanic Variation in the Rare Earth, Major, and Trace Element Depositional Chemistry of Chert: Perspectives Gained from the DSDP and ODP Record. *Geochimica et Cosmochimica Acta*, **56**, 1897-1913.
https://doi.org/10.1016/0016-7037(92)90319-e

[81] Pecoits, E., Gingras, M.K., Barley, M.E., Kappler, A., Posth, N.R. and Konhauser, K.O. (2009) Petrography and Geochemistry of the Dales Gorge Banded Iron Formation: Paragenetic Sequence, Source and Implications for Palaeo-Ocean Chemistry. *Precambrian Research*, **172**, 163-187. https://doi.org/10.1016/j.precamres.2009.03.014

[82] Basta, F.F., Maurice, A.E., Fontboté, L. and Favarger, P. (2011) Petrology and Geochemistry of the Banded Iron Formation (BIF) of Wadi Karim and Um Anab, Eastern Desert, Egypt: Implications for the Origin of Neoproterozoic Bif. *Precambrian Research*, **187**, 277-292. https://doi.org/10.1016/j.precamres.2011.03.011

[83] Rao, T.G. and Naqvi, S.M. (1995) Geochemistry, Depositional Environment and Tectonic Setting of the Bif's of the Late Archaean Chitradurga Schist Belt, India. *Chemical Geology*, **121**, 217-243. https://doi.org/10.1016/0009-2541(94)00116-p

[84] Raju, P.V.S. (2009) Petrography and Geochemical Behaviour of Trace Element, REE and Precious Metal Signatures of Sulphidic Banded Iron Formations from the Chikkasiddavanahalli Area, Chitradurga Schist Belt, India. *Journal of Asian Earth Sciences*, **34**, 663-673. https://doi.org/10.1016/j.jseaes.2008.10.005

[85] Mloszewska, A.M., Pecoits, E., Cates, N.L., Mojzsis, S.J., O'Neil, J., Robbins, L.J., *et al.* (2012) The Composition of Earth's Oldest Iron Formations: The Nuvvuagittuq Supracrustal Belt (Québec, Canada). *Earth and Planetary Science Letters*, **317**, 331-342.
https://doi.org/10.1016/j.epsl.2011.11.020

[86] Bau, M. and Dulski, P. (1996) Distribution of Yttrium and Rare-Earth Elements in the Penge and Kuruman Iron-Formations, Transvaal Supergroup, South Africa. *Precambrian Research*, **79**, 37-55. https://doi.org/10.1016/0301-9268(95)00087-9

[87] Pourmand, A., Dauphas, N. and Ireland, T.J. (2012) A Novel Extraction Chromatography and MC-ICP-MS Technique for Rapid Analysis of REE, Sc and Y: Revising CI-Chondrite and Post-Archean Australian Shale (PAAS) Abundances. *Chemical Geology*, **291**, 38-54. https://doi.org/10.1016/j.chemgeo.2011.08.011

[88] Sun, D., Meng, D., Cai, Y., Fan, B., Li, Y., Jiang, W., *et al.* (2015) Non-Fullerene-Acceptor-Based Bulk-Heterojunction Organic Solar Cells with Efficiency over 7%. *Journal of the American Chemical Society*, **137**, 11156-11162.
https://doi.org/10.1021/jacs.5b06414

[89] McLennan, S.M. (2001) Relationships between the Trace Element Composition of Sedimentary Rocks and Upper Continental Crust. *Geochemistry*, *Geophysics*, *Geosystems*, **2**, 2000GC000109. https://doi.org/10.1029/2000gc000109

[90] Evensen, N.M., Hamilton, P.J. and O'Nions, R.K. (1978) Rare-Earth Abundances in Chondritic Meteorites. *Geochimica et Cosmochimica Acta*, **42**, 1199-1212.
https://doi.org/10.1016/0016-7037(78)90114-x

[91] Bolhar, R., Kamber, B.S., Moorbath, S., Fedo, C.M. and Whitehouse, M.J. (2004) Characterisation of Early Archaean Chemical Sediments by Trace Element Signatures. *Earth and Planetary Science Letters*, **222**, 43-60.
https://doi.org/10.1016/j.epsl.2004.02.016

[92] Planavsky, N., Bekker, A., Rouxel, O.J., Kamber, B., Hofmann, A., Knudsen, A., *et al.* (2010) Rare Earth Element and Yttrium Compositions of Archean and Paleoproterozoic Fe Formations Revisited: New Perspectives on the Significance and Mechanisms of Deposition. *Geochimica et Cosmochimica Acta*, **74**, 6387-6405. https://doi.org/10.1016/j.gca.2010.07.021

[93] Derry, L.A. and Jacobsen, S.B. (1990) The Chemical Evolution of Precambrian Seawater: Evidence from Rees in Banded Iron Formations. *Geochimica et Cosmochimica Acta*, **54**, 2965-2977. https://doi.org/10.1016/0016-7037(90)90114-z

[94] Bau, M. and Möller, P. (1993) Rare Earth Element Systematics of the Chemically Precipitated Component in Early Precambrian Iron Formations and the Evolution of the Terrestrial Atmosphere-Hydrosphere-Lithosphere System. *Geochimica et Cosmochimica Acta*, **57**, 2239-2249. https://doi.org/10.1016/0016-7037(93)90566-f

[95] McLennan, S.M. (1989) Chapter 7. Rare Earth Elements in Sedimentary Rocks: Influence of Provenance and Sedimentary Processes. In: Lipin, B.R. and McKay, G.A., Eds., *Geochemistry and Mineralogy of Rare Earth Elements*, De Gruyter, 169-200. https://doi.org/10.1515/9781501509032-010

[96] Polat, A. and Hofmann, A.W. (2003) Alteration and Geochemical Patterns in the 3.7-3.8 Ga Isua Greenstone Belt, West Greenland. *Precambrian Research*, **126**, 197-218. https://doi.org/10.1016/s0301-9268(03)00095-0

[97] Martin, L.A.J., Ballèvre, M., Boulvais, P., Halfpenny, A., Vanderhaeghe, O., Duchêne, S., *et al.* (2010) Garnet Re-Equilibration by Coupled Dissolution-Reprecipitation: Evidence from Textural, Major Element and Oxygen Isotope Zoning of 'Cloudy' Garnet. *Journal of Metamorphic Geology*, **29**, 213-231. https://doi.org/10.1111/j.1525-1314.2010.00912.x

[98] Moyen, J. (2011) The Composite Archaean Grey Gneisses: Petrological Significance, and Evidence for a Non-Unique Tectonic Setting for Archaean Crustal Growth. *Lithos*, **123**, 21-36. https://doi.org/10.1016/j.lithos.2010.09.015

[99] Halla, J. (2020) The TTG-Amphibolite Terrains of Arctic Fennoscandia: Infinite Networks of Amphibolite Metatexite-Diatexite Transitions. *Frontiers in Earth Science*, **8**, Article No. 252. https://doi.org/10.3389/feart.2020.00252

[100] Liou, P. and Guo, J. (2019) Generation of Archaean TTG Gneisses through Amphibole-Dominated Fractionation. *Journal of Geophysical Research*: *Solid Earth*, **124**, 3605-3619. https://doi.org/10.1029/2018jb017024

[101] Laurent, O., Guitreau, M., Bruand, E. and Moyen, J. (2024) At the Dawn of Continents: Archean Tonalite-Trondhjemite-Granodiorite Suites. *Elements*, **20**, 174-179. https://doi.org/10.2138/gselements.20.3.174

[102] Jayananda, M., Santosh, M. and Aadhiseshan, K.R. (2018) Formation of Archean (3600-2500 Ma) Continental Crust in the Dharwar Craton, Southern India. *Earth-Science Reviews*, **181**, 12-42. https://doi.org/10.1016/j.earscirev.2018.03.013

[103] Gao, S., Rudnick, R.L., Yuan, H., Liu, X., Liu, Y., Xu, W., *et al.* (2004) Recycling Lower Continental Crust in the North China Craton. *Nature*, **432**, 892-897. https://doi.org/10.1038/nature03162

[104] Rapp, R.P., Shimizu, N. and Norman, M.D. (2003) Growth of Early Continental Crust by Partial Melting of Eclogite. *Nature*, **425**, 605-609. https://doi.org/10.1038/nature02031

[105] Rollinson, H.R. (1993) A Terrane Interpretation of the Archaean Limpopo Belt. *Geological Magazine*, **130**, 755-765. https://doi.org/10.1017/s001675680002313x

[106] Defant, M.J. and Drummond, M.S. (1990) Derivation of Some Modern Arc Magmas

by Melting of Young Subducted Lithosphere. *Nature*, **347**, 662-665. https://doi.org/10.1038/347662a0

[107] Schiano, P., Monzier, M., Eissen, J., Martin, H. and Koga, K.T. (2010) Simple Mixing as the Major Control of the Evolution of Volcanic Suites in the Ecuadorian Andes. *Contributions to Mineralogy and Petrology*, **160**, 297-312. https://doi.org/10.1007/s00410-009-0478-2

[108] Foley, S., Tiepolo, M. and Vannucci, R. (2002) Growth of Early Continental Crust Controlled by Melting of Amphibolite in Subduction Zones. *Nature*, **417**, 837-840. https://doi.org/10.1038/nature00799

[109] Stern, C.R. and Kilian, R. (1996) Role of the Subducted Slab, Mantle Wedge and Continental Crust in the Generation of Adakites from the Andean Austral Volcanic Zone. *Contributions to Mineralogy and Petrology*, **123**, 263-281. https://doi.org/10.1007/s004100050155

[110] Qian, Q. and Hermann, J. (2013) Partial Melting of Lower Crust at 10-15 Kbar: Constraints on Adakite and TTG Formation. *Contributions to Mineralogy and Petrology*, **165**, 1195-1224. https://doi.org/10.1007/s00410-013-0854-9

[111] Martin, H., Smithies, R.H., Rapp, R., Moyen, J. and Champion, D. (2005) An Overview of Adakite, Tonalite-Trondhjemite-Granodiorite (TTG), and Sanukitoid: Relationships and Some Implications for Crustal Evolution. *Lithos*, **79**, 1-24. https://doi.org/10.1016/j.lithos.2004.04.048

[112] Zhang, H., He, H., Ai, G., Hou, D., Zeng, T. and Chen, L. (2025) Geochronology and Geochemistry of the Yajiangqiao Plutonic Rocks in the Central South China Block: Implication for Petrogenesis and Tectonic Setting. *Geochemistry International*, **63**, 391-421. https://doi.org/10.1134/s0016702924601736

[113] Aye, B.A., Sababa, E. and Ndjigui, P. (2017) Geochemistry of S, Cu, Ni, Cr and Au-PGE in the Garnet Amphibolites from the Akom II Area in the Archaean Congo Craton, Southern Cameroon. *Geochemistry*, **77**, 81-93. https://doi.org/10.1016/j.chemer.2017.01.009

[114] Winchester, J.A. and Floyd, P.A. (1977) Geochemical Discrimination of Different Magma Series and Their Differentiation Products Using Immobile Elements. *Chemical Geology*, **20**, 325-343. https://doi.org/10.1016/0009-2541(77)90057-2

[115] Jakes, P. and Gill, J. (1970) Rare Earth Elements and the Island Arc Tholeiitic Series. *Earth and Planetary Science Letters*, **9**, 17-28. https://doi.org/10.1016/0012-821x(70)90018-x

[116] Perchuk, L.L. (1968) Pyroxene-Garnet Equilibrium and the Depth Facies of Eclogites. *International Geology Review*, **10**, 280-318. https://doi.org/10.1080/00206816809474875

[117] Kushiro, I. (1990) Partial Melting of Mantle Wedge and Evolution of Island Arc Crust. *Journal of Geophysical Research*: *Solid Earth*, **95**, 15929-15939. https://doi.org/10.1029/jb095ib10p15929

[118] Bédard, J.H. (2006) A Catalytic Delamination-Driven Model for Coupled Genesis of Archaean Crust and Sub-Continental Lithospheric Mantle. *Geochimica et Cosmochimica Acta*, **70**, 1188-1214. https://doi.org/10.1016/j.gca.2005.11.008

[119] Pearce, J.A. and Cann, J.R. (1973) Tectonic Setting of Basic Volcanic Rocks Determined Using Trace Element Analyses. *Earth and Planetary Science Letters*, **19**, 290-300. https://doi.org/10.1016/0012-821x(73)90129-5

[120] Pearce, T.H., Gorman, B.E. and Birkett, T.C. (1975) The TiO_2-K_2O-P_2O_5 Diagram: A Method of Discriminating between Oceanic and Non-Oceanic Basalts. *Earth and*

Planetary Science Letters, **24**, 419-426.
https://doi.org/10.1016/0012-821x(75)90149-1

[121] Abdel-Rahman, A.M. and Nassar, P.E. (2004) Cenozoic Volcanism in the Middle East: Petrogenesis of Alkali Basalts from Northern Lebanon. *Geological Magazine*, **141**, 545-563. https://doi.org/10.1017/s0016756804009604

[122] Moghazi, A.M. (2003) Geochemistry of a Tertiary Continental Basalt Suite, Red Sea Coastal Plain, Egypt: Petrogenesis and Characteristics of the Mantle Source Region. *Geological Magazine*, **140**, 11-24. https://doi.org/10.1017/s0016756802006994

[123] Hughes, C.J. (1973) Late Precambrian Volcanic Rocks of Avalon, Newfoundland—A Spilite/Keratophyre Province: Recognition and Implications. *Canadian Journal of Earth Sciences*, **10**, 272-282. https://doi.org/10.1139/e73-024

[124] Irvine, T.N. and Baragar, W.R.A. (1971) A Guide to the Chemical Classification of the Common Volcanic Rocks. *Canadian Journal of Earth Sciences*, **8**, 523-548.
https://doi.org/10.1139/e71-055

[125] Miyashiro, A. (1978) Nature of Alkalic Volcanic Rock Series. *Contributions to Mineralogy and Petrology*, **66**, 91-104. https://doi.org/10.1007/bf00376089

[126] Kempton, P.D. and Harmon, R.S. (1992) Oxygen Isotope Evidence for Large-Scale Hybridization of the Lower Crust during Magmatic Underplating. *Geochimica et Cosmochimica Acta*, **56**, 971-986. https://doi.org/10.1016/0016-7037(92)90041-g

[127] Miyashiro, A. (1974) Volcanic Rock Series in Island Arcs and Active Continental Margins. *American Journal of Science*, **274**, 321-355.
https://doi.org/10.2475/ajs.274.4.321

[128] Irvine, T.N. and Baragar, W.R.A. (1972) Muskox Intrusion and Coppermine River lavas, Northwest Territories, Canada. 24*th International Geological Congress*, Montreal, 21-30 août 1972.

[129] Gourcerol, B., Kontak, D.J., Thurston, P.C. and Duparc, Q. (2016) Do Magnetite Layers in Algoma-Type Banded Iron Formations (BIF) Preserve Their Primary Geochemical Signature? A Case Study of Samples from Three Archean Bif-Hosted Gold Deposits. *The Canadian Mineralogist*, **54**, 605-624.
https://doi.org/10.3749/canmin.1500090

[130] Ndime, E.N., Ganno, S. and Nzenti, J.P. (2019) Geochemistry and Pb-Pb Geochronology of the Neoarchean Nkout West Metamorphosed Banded Iron Formation, Southern Cameroon. *International Journal of Earth Sciences*, **108**, 1551-1570.
https://doi.org/10.1007/s00531-019-01719-5

[131] Soh Tamehe, L., Wei, C., Ganno, S., Rosière, C.A., Nzenti, J.P., Gatse Ebotehouna, C., *et al.* (2021) Depositional Age and Tectonic Environment of the Gouap Banded Iron Formations from the Nyong Group, SW Cameroon: Insights from Isotopic, Geochemical and Geochronological Studies of Drillcore Samples. *Geoscience Frontiers*, **12**, 549-572. https://doi.org/10.1016/j.gsf.2020.07.009

[132] Bau, M. (1996) Controls on the Fractionation of Isovalent Trace Elements in Magmatic and Aqueous Systems: Evidence from Y/Ho, Zr/Hf, and Lanthanide Tetrad Effect. *Contributions to Mineralogy and Petrology*, **123**, 323-333.
https://doi.org/10.1007/s004100050159

[133] Sylvestre, G., Evine Laure, N.T., Gus Djibril, K.N., Arlette, D.S., Cyriel, M., Timoléon, N., *et al.* (2017) A Mixed Seawater and Hydrothermal Origin of Superior-Type Banded Iron Formation (BIF)-Hosted Kouambo Iron Deposit, Palaeoproterozoic Nyong Series, Southwestern Cameroon: Constraints from Petrography and Geochemistry. *Ore Geology Reviews*, **80**, 860-875.
https://doi.org/10.1016/j.oregeorev.2016.08.021

[134] Peng, Z., Wang, C., Tong, X., Zhang, L. and Zhang, B. (2018) Element Geochemistry and Neodymium Isotope Systematics of the Neoarchean Banded Iron Formations in the Qingyuan Greenstone Belt, North China Craton. *Ore Geology Reviews*, **102**, 562-584. https://doi.org/10.1016/j.oregeorev.2018.09.008

[135] Morris, R.C. (1993) Genetic Modelling for Banded Iron-Formation of the Hamersley Group, Pilbara Craton, Western Australia. *Precambrian Research*, **60**, 243-286. https://doi.org/10.1016/0301-9268(93)90051-3

[136] Alibo, D.S. and Nozaki, Y. (1999) Rare Earth Elements in Seawater: Particle Association, Shale-Normalization, and Ce Oxidation. *Geochimica et Cosmochimica Acta*, **63**, 363-372. https://doi.org/10.1016/s0016-7037(98)00279-8

[137] Douville, E., Bienvenu, P., Charlou, J.L., Donval, J.P., Fouquet, Y., Appriou, P., *et al.* (1999) Yttrium and Rare Earth Elements in Fluids from Various Deep-Sea Hydrothermal Systems. *Geochimica et Cosmochimica Acta*, **63**, 627-643. https://doi.org/10.1016/s0016-7037(99)00024-1

[138] Pearce, J.A., Lippard, S.J. and Roberts, S. (1984) Characteristics and Tectonic Significance of Supra-Subduction Zone Ophiolites. *Geological Society*, *London*, *Special Publications*, **16**, 77-94. https://doi.org/10.1144/gsl.sp.1984.016.01.06

[139] Kato, Y., Ohta, I., Tsunematsu, T., Watanabe, Y., Isozaki, Y., Maruyama, S., *et al.* (1998) Rare Earth Element Variations in Mid-Archean Banded Iron Formations: Implications for the Chemistry of Ocean and Continent and Plate Tectonics. *Geochimica et Cosmochimica Acta*, **62**, 3475-3497. https://doi.org/10.1016/s0016-7037(98)00253-1

[140] Danielson, A., Möller, P. and Dulski, P. (1992) The Europium Anomalies in Banded Iron Formations and the Thermal History of the Oceanic Crust. *Chemical Geology*, **97**, 89-100. https://doi.org/10.1016/0009-2541(92)90137-t

[141] Alexander, B.W., Bau, M., Andersson, P. and Dulski, P. (2008) Continentally-Derived Solutes in Shallow Archean Seawater: Rare Earth Element and Nd Isotope Evidence in Iron Formation from the 2.9 Ga Pongola Supergroup, South Africa. *Geochimica et Cosmochimica Acta*, **72**, 378-394. https://doi.org/10.1016/j.gca.2007.10.028

[142] Teutsong, T., Bontognali, T.R.R., Ndjigui, P., Vrijmoed, J.C., Teagle, D., Cooper, M., *et al.* (2017) Petrography and Geochemistry of the Mesoarchean Bikoula Banded Iron Formation in the Ntem Complex (Congo Craton), Southern Cameroon: Implications for Its Origin. *Ore Geology Reviews*, **80**, 267-288. https://doi.org/10.1016/j.oregeorev.2016.07.003

[143] Soh Tamehe, L., Nzepang Tankwa, M., Chongtao, W., Ganno, S., Ngnotue, T., Kouankap Nono, G.D., *et al.* (2018) Geology and Geochemical Constrains on the Origin and Depositional Setting of the Kpwa-Atog Boga Banded Iron Formations (BIFs), Northwestern Congo Craton, Southern Cameroon. *Ore Geology Reviews*, **95**, 620-638. https://doi.org/10.1016/j.oregeorev.2018.03.017

[144] Edjo-Minko, R., Isaac Bertrand Mbowou, G., Daama, I., Nguihdama, D. and Mienlam Essi, M. (2024) The Petrography and Geochemistry of Iron-Bearing Units from Mingo'o Area (Ntem Complex, Southern Cameroon). *International Journal of Advanced Geosciences*, **12**, 35-46. https://doi.org/10.14419/00a8vb15

[145] Klein, C. (2005) Some Precambrian Banded Iron-Formations (BIFs) from around the World: Their Age, Geologic Setting, Mineralogy, Metamorphism, Geochemistry, and Origins. *American Mineralogist*, **90**, 1473-1499. https://doi.org/10.2138/am.2005.1871

[146] Smith, A.J.B., Beukes, N.J. and Gutzmer, J. (2013) The Composition and Depositional Environments of Mesoarchean Iron Formations of the West Rand Group of the Wit-

watersrand Supergroup, South Africa. *Economic Geology*, **108**, 111-134. https://doi.org/10.2113/econgeo.108.1.111

[147] Fryer, B.J. (1977) Rare Earth Evidence in Iron-Formations for Changing Precambrian Oxidation States. *Geochimica et Cosmochimica Acta*, **41**, 361-367. https://doi.org/10.1016/0016-7037(77)90263-0

[148] Ganno, S., Tsozué, D., Kouankap Nono, G.D., Tchouatcha, M.S., Ngnotué, T., Gamgne Takam, R., *et al.* (2018) Geochemical Constraints on the Origin of Banded Iron Formation-Hosted Iron Ore from the Archaean Ntem Complex (Congo Craton) in the Meyomessi Area, Southern Cameroon. *Resource Geology*, **68**, 287-302. https://doi.org/10.1111/rge.12172

[149] Harris, N.B.W., Pearce, J.A. and Tindle, A.G. (1986) Geochemical Characteristics of Collision-Zone Magmatism. *Geological Society*, *London*, *Special Publications*, **19**, 67-81. https://doi.org/10.1144/gsl.sp.1986.019.01.04

[150] Batchelor, R.A. and Bowden, P. (1985) Petrogenetic Interpretation of Granitoid Rock Series Using Multicationic Parameters. *Chemical Geology*, **48**, 43-55. https://doi.org/10.1016/0009-2541(85)90034-8

[151] Kamguia Kamani, M.S., Wang, W., Tchouankoue, J., Huang, S., Yomeun, B., Xue, E., *et al.* (2021) Neoproterozoic Syn-Collision Magmatism in the Nkondjock Region at the Northern Border of the Congo Craton in Cameroon: Geodynamic Implications for the Central African Orogenic Belt. *Precambrian Research*, **353**, Article 106015. https://doi.org/10.1016/j.precamres.2020.106015

[152] Jung, C., Jung, S., Hoffer, E. and Berndt, J. (2006) Petrogenesis of Tertiary Mafic Alkaline Magmas in the Hocheifel, Germany. *Journal of Petrology*, **47**, 1637-1671. https://doi.org/10.1093/petrology/egl023

[153] Rooney, T.O. (2010) Geochemical Evidence of Lithospheric Thinning in the Southern Main Ethiopian Rift. *Lithos*, **117**, 33-48. https://doi.org/10.1016/j.lithos.2010.02.002

[154] Niu, Y., Waggoner, D.G., Sinton, J.M. and Mahoney, J.J. (1996) Mantle Source Heterogeneity and Melting Processes beneath Seafloor Spreading Centers: The East Pacific Rise, 18°-19°S. *Journal of Geophysical Research*: *Solid Earth*, **101**, 27711-27733. https://doi.org/10.1029/96jb01923

[155] Pearce, J.A. and Peate, D.W. (1995) Tectonic Implications of the Composition of Volcanic ARC Magmas. *Annual Review of Earth and Planetary Sciences*, **23**, 251-285. https://doi.org/10.1146/annurev.ea.23.050195.001343

[156] Münker, C. (2000) The Isotope and Trace Element Budget of the Cambrian Devil River Arc System, New Zealand: Identification of Four Source Components. *Journal of Petrology*, **41**, 759-788. https://doi.org/10.1093/petrology/41.6.759

[157] Shervais, J.W. (1982) Ti-V Plots and the Petrogenesis of Modern and Ophiolitic Lavas. *Earth and Planetary Science Letters*, **59**, 101-118. https://doi.org/10.1016/0012-821x(82)90120-0

[158] Saccani, E. (2015) A New Method of Discriminating Different Types of Post-Archean Ophiolitic Basalts and Their Tectonic Significance Using Th-Nb and Ce-Dy-Yb Systematics. *Geoscience Frontiers*, **6**, 481-501. https://doi.org/10.1016/j.gsf.2014.03.006

[159] Dilek, Y., Furnes, H. and Shallo, M. (2008) Geochemistry of the Jurassic Mirdita Ophiolite (Albania) and the MORB to SSZ Evolution of a Marginal Basin Oceanic Crust. *Lithos*, **100**, 174-209. https://doi.org/10.1016/j.lithos.2007.06.026

[160] Pearce, J.A. (1982) Trace Element Characteristics of Lavas from Destructive Plate Boundaries. In: Thorpe, R.S., Ed., *Andesites*: *Orogenic Andesites and Related Rocks*, John Wiley and Sons, 525-548. https://orca.cardiff.ac.uk/id/eprint/8625/

[161] Pearce, J.A. (2008) Geochemical Fingerprinting of Oceanic Basalts with Applications to Ophiolite Classification and the Search for Archean Oceanic Crust. *Lithos*, **100**, 14-48. https://doi.org/10.1016/j.lithos.2007.06.016

[162] Deschamps, F., Godard, M., Guillot, S. and Hattori, K. (2013) Geochemistry of Subduction Zone Serpentinites: A Review. *Lithos*, **178**, 96-127. https://doi.org/10.1016/j.lithos.2013.05.019

[163] Yellappa, T., Venkatasivappa, V., Koizumi, T., Chetty, T.R.K., Santosh, M. and Tsunogae, T. (2014) The Mafic-Ultramafic Complex of Aniyapuram, Cauvery Suture Zone, Southern India: Petrological and Geochemical Constraints for Neoarchean Suprasubduction Zone Tectonics. *Journal of Asian Earth Sciences*, **95**, 81-98. https://doi.org/10.1016/j.jseaes.2014.04.023

[164] Wang, W., Liu, S., Cawood, P.A., Bai, X., Guo, R., Guo, B., *et al.* (2016) Late Neoarchean Subduction-Related Crustal Growth in the Northern Liaoning Region of the North China Craton: Evidence from ~2.55 to 2.50 Ga Granitoid Gneisses. *Precambrian Research*, **281**, 200-223. https://doi.org/10.1016/j.precamres.2016.05.018

[165] El-Shazly, A.K., Khalil, K.I. and Helba, H.A. (2019) Geochemistry of Banded Iron Formations and Their Host Rocks from the Central Eastern Desert of Egypt: A Working Genetic Model and Tectonic Implications. *Precambrian Research*, **325**, 192-216. https://doi.org/10.1016/j.precamres.2019.02.011

[166] Loose, D. and Schenk, V. (2018) 2.09 Ga Old Eclogites in the Eburnian-Transamazonian Orogen of Southern Cameroon: Significance for Palaeoproterozoic Plate Tectonics. *Precambrian Research*, **304**, 1-11. https://doi.org/10.1016/j.precamres.2017.10.018

[167] Houketchang Bouyo, M., Penaye, J., Mouri, H. and Toteu, S.F. (2019) Eclogite Facies Metabasites from the Paleoproterozoic Nyong Group, SW Cameroon: Mineralogical Evidence and Implications for a High-Pressure Metamorphism Related to a Subduction Zone at the NW Margin of the Archean Congo Craton. *Journal of African Earth Sciences*, **149**, 215-234. https://doi.org/10.1016/j.jafrearsci.2018.08.010

[168] Moudioh, C., Tamehe, L.S., Ganno, S., Nzepang Tankwa, M., Brando Soares, M., Ghosh, R., *et al.* (2020) Tectonic Setting of the Bipindi Greenstone Belt, Northwest Congo Craton, Cameroon: Implications on BIF Deposition. *Journal of African Earth Sciences*, **171**, Article 103971. https://doi.org/10.1016/j.jafrearsci.2020.103971

[169] Mvodo, H., Ganno, S., Kouankap Nono, G.D., Fossi, D.H., Nga Essomba, P.E., Nzepang Tankwa, M., *et al.* (2022) Petrogenesis, LA-ICP-MS Zircon U-Pb Geochronology and Geodynamic Implications of the Kribi Metavolcanic Rocks, Nyong Group, Congo Craton. *Acta Geochimica*, **41**, 470-495. https://doi.org/10.1007/s11631-022-00533-2

[170] Owona, S., Schulz, B., Minyem, D., Ratschbacher, L., Tchamabe, B.C., Olinga, J.B., *et al.* (2022) Eburnean/Trans-Amazonian Orogeny in the Nyong Complex of Southwestern Cameroon: Meta-Basite Geochemistry and Metamorphic Petrology. *Journal of African Earth Sciences*, **190**, Article 104515. https://doi.org/10.1016/j.jafrearsci.2022.104515

[171] Cabanis, B. (1989) Le diagramme La/10-Y/15-Nb/8: Un outil pour la discrimination des séries volcaniques et la mise en évidence des processus de mélange et/ou de contamination crustale. *Comptes Rendus de l'Académie des Sciences. Série II*, **309**, 2023-2029. https://cir.nii.ac.jp/crid/1570854176404988416

[172] Nga Essomba Tsoungui, P., Ganno, S., Tanko Njiosseu, E.L., Ndema Mbongue, J.L., Kamguia Woguia, B., Soh Tamehe, L., *et al.* (2020) Geochemical Constraints on the Origin and Tectonic Setting of the Serpentinized Peridotites from the Paleoprotero-

zoic Nyong Series, Eseka Area, SW Cameroon. *Acta Geochimica*, **39**, 404-422. https://doi.org/10.1007/s11631-019-00368-4

[173] Soh Tamehe, L., Wei, C., Ganno, S., Rosière, C.A., Li, H., Soares, M.B., *et al.* (2022) Provenance of Metasiliciclastic Rocks at the Northwestern Margin of the East Gabonian Block: Implications for Deposition of BIFs and Crustal Evolution in Southwestern Cameroon. *Precambrian Research*, **376**, Article 106677. https://doi.org/10.1016/j.precamres.2022.106677

[174] Fuanya, C., Bolarinwa, A.T., Kankeu, B., Yongue, R.F., Tangko, E.T. and Nkepguep, F.Y. (2019) Geochemical Characteristics and Petrogenesis of Basic Rocks in the Ako'ozam-Njabilobe Area, Southwestern Cameroon: Implications for Au Genesis. *SN Applied Sciences*, **1**, Article No. 904. https://doi.org/10.1007/s42452-019-0959-5

[175] Woguia, B.K., Nono, G.D.K., Tsoungui, P.E.N.E., Njiosseu, E.L.T., Kenne, P.A. and Nzenti, J.P. (2022) Geochemistry and U-Pb Zircon Age of the Paleoproterozoic Metasedimentary Rocks from the Bidou I, Nyong Series, Cameroon: Implications for Provenance and Tectonic Setting. *Arabian Journal of Geosciences*, **15**, Article No. 154. https://doi.org/10.1007/s12517-022-09476-7

[176] Santos, F.G., Cavalcanti Neto, M.T.O., Ferreira, V.P. and Bertotti, A.L. (2020) Eo to Paleoarchean Metamafic-Ultramafic Rocks from the Central Portion of the Rio Grande Do Norte Domain, Borborema Province, Northeast Brazil: The Oldest South American Platform Rocks. *Journal of South American Earth Sciences*, **97**, Article 102410. https://doi.org/10.1016/j.jsames.2019.102410

[177] Polat, A. and Kerrich, R. (2000) Archean Greenstone Belt Magmatism and the Continental Growth-Mantle Evolution Connection: Constraints from Th-U-Nb-LREE Systematics of the 2.7 Ga Wawa Subprovince, Superior Province, Canada. *Earth and Planetary Science Letters*, **175**, 41-54. https://doi.org/10.1016/s0012-821x(99)00283-6